WIRELESS SENSORS FOR ENHANCING FOOD SUPPLY CHAIN VISIBILITY

By

Saranraj Karuppuswami

A DISSERTATION

Submitted to
Michigan State University
in partial fulfillment of the requirements
for the degree of

Electrical Engineering — Doctor of Philosophy

2019

ABSTRACT

WIRELESS SENSORS FOR ENHANCING FOOD SUPPLY CHAIN VISIBILITY

By

Saranraj Karuppuswami

The demand for providing safe and quality food from the farm to the plate had led to the development of sensor technologies for quality control and real-time end-to-end monitoring of food along the supply chain. These advanced sensors serve as the first line of defense against food-borne outbreaks, economically motivated adulteration, and food contamination preventing illness, deaths, huge economic losses and promotes global health and well-being. The key goal is to ensure that the food reaching the fork meets the highest safety standards by promoting tamper-free sustainable practices along the food supply chain. Real-time food monitoring also prevents unnecessary wastage due to spoilage or good food being thrown out due to misconception of the labeled expiration date.

In this dissertation, a number of RF passive wireless sensing approaches are presented that allows simultaneous tracking and quality monitoring of packaged food products as it moves along the supply chain. The end goal is to develop a low cost, long range, battery-free, and real time sensor tag which can detect multiple parameters of the packaged food simultaneously and at the same time provide the identification information. In order to realize a multi-functional sensor tag, a number of sensing approaches are developed targeting four different types of food related quality control challenges; Adulteration, Contamination, Wastage, and Spoilage. To identify and eliminate food adulteration, magnetoelastic based dielectric and viscosity sensors are developed. These hybrid sensors are shorter range sensors and a number of liquid food items such as milk and oil are characterized. A sensing approach

that utilizes 3D printed RF sensors coupled to a microfludic channel for liquid profling by monitoring the dielectric constant is developed for food quality detection. Next, to prevent contamination, capacitance based short range inductor-capacitor (LC) tanks are developed. An interdisciplinary approach which is a confluence of carbohydrate coated nano particles capturing bacteria in liquid food with RF detection is developed. A common method to prevent wastage or spoilage is to detect and profile aroma emitted from food. Adsorption, absorption, and capillary condensation based short range as well as long range sensors that monitor the dielectric constant or the conductivity of the target food are developed. First, a short range capillary condensation based sensor is demonstrated for volatile profiling using a porous substrate and an LC tank. This is followed by demonstrating sensitivity and specificity of different thin-film coated short range sensors that detect vapors that are directly related to the spoilage index of the food. Finally, a long range passive sensor integrated with ID is demonstrated for detecting Ammonia in packaged food. The developed sensor is compatible with existing RFID infrastructure and is capable of digitizing the sensor information along with the identification information for transmission. Overall, the work demonstrates that a passive multi-modal sensor provides additional information about products moving across the supply chain transforming the tracebility-centric supply chain into a value-centric one with increased visibility and empowers the different stake holders with the quality information as the product moves along the supply chain.

This dissertation is dedicated to my beloved family...

ACKNOWLEDGMENTS

From a small town in Southern Indian State of Tamilnadu, Coimbatore to Michigan, East Lansing, my life's journey was filled with adventure and unforgettable memories. I am grateful to a number of people who has contributed in some way or the other to help me complete my PhD study at Michigan State University. First and foremost, I would like to express my deepest gratitude to my advisor Dr. Premjeet Chahal who in many ways had molded my professional and personal life. He has given his time and energy to make me what I am today and for which I am forever indebted. Next, I am thankful to the rest of my committee members Dr. Edward J. Rothwell, Dr. Wen Li, Dr. Evangelyn C. Alocilja for their valuable suggestions and feedback through my PhD work. I am especially thankful to Dr. Rothwell for guiding me during my turbulent times and encouraging me both professionally as well as personally. I have taken most of my EM courses at MSU with him and I have learned a lot from him. I would also like to thank Dr. Shanker Balasubramaniam for giving me his time and encouraging words.

I would like to thank the AXIA Institute (previously known as Midland Research Institute for Value Chain Creation (MRIVCC) for sponsoring my research and making all this work possible, especially Katherine A. Franz and Donald L. Buchalski. I would like to thank a number of people in the Department of Electrical and Computer Engineering for all their support starting with the ECE shop, Mr. Brain Wright and Mr. Gregg Mulder without whom most of the work presented in this thesis is not possible. Mr. Karl Dersch from ECE cleanroom for being on call whenever needed. Mrs. Carol Flegler from the Center for Advanced Microscopy for helping me with the SEM imaging. A special thanks to Dr. Katy Luchini Colbry, Assistant Dean for graduate studies for helping me with funding during my

most difficult times. I would like to thank Dr. Tim Hogan who taught me clean room and because of whom most of the fabrication work in this thesis was made possible.

I would like to thank my fellow colleagues and alumni from the Electromagnetics Research Group (EMRG). I had learned a lot from my colleagues how to go about with the lab and they were my sole support thorughout my graduate school making it a fun filled ride. I am thankful to our previous members Dr. Kyoung Youl Park, Dr. Nophadon Wiwatcharagoses, and Dr. Joshua Myers for all their wisdom. Further, special thanks to special friends Dr. Amanpreet Kaur and Dr. Mohd Ifwat Mohd Ghazali for contributing to my PhD work and being there for me. My Pokemon buddy and a good friend Dr. Jennifer Byford for all the time we spent in working (playing) together. My two best friends and soon to be doctors Mr. Saikat Mondal and Mr. Deepak Kumar for all the time (fun) we had together on and off campus and for all the valuable contributions towards my PhD work. My other colleagues and friends Pratik Chatterjee, Yuxiao He, Chris Oakley, Michael Craton, Vinny Gjokaj, Stavros Vakalis, Serge Mghabghab, Anton Schlegel, Omkar Ramachandran, Abdel Alsnayyan, Zane Crawford, Scott OConnor, Sean Ellison, Elliot Lu and everyone else who has been a part of my day to day life. Thank you all!

Finally, I would like to thank my family, my wife Sri Subhaasini C.N and my daughter Saishastika Saran for all the endless love and support, my parents (late) Mr. R. Karuppuswami and Dr. K.R. Thenmozhi for all their sacrifice and love, my grandparents (late) Mr. K.V Ramasamy and Mrs. R. Lakshmi for making me dream and encouraging me with love, and my brother Naveenraj Karuppuswami.

TABLE OF CONTENTS

LIST OF TABLES

LIST OF FIGURES

Chapter 1

Introduction

Quality control of food products is necessary to prevent loss of nutrients, food-borne outbreaks and food-related illness. The United States Center for Diseases Control (CDC) estimates that 48 million people get sick from food-borne illness, 128,000 are hospitalized, and 3,000 die each year [1]. Three major categories that are a potential threat to public health and safety are contamination, adulteration, and spoilage of food items. Food products undergo multiple stages of processing before it reaches the plate and CDC estimates that the food is prone to contamination at any stage of the food supply chain; from the farm to the consumer. Food recalls due to contamination of pathogens or allergens cost the food industry a huge economic and reputation loss. In February 2018, FDA recalled Greek and Low Fat Yogurts from Michigan's supermarket giant Meijer due to risk of small glass particles contamination [2] [3].

Food fraud and economically motivated adulteration have become a rampant problem in the United States leading to several hundred deaths and disease outbreaks [4]. Intentional adulteration of food causes wide scale harm to public health leading to illness, death, and economic disruption of food supply [5]. The most common practices in food adulteration are mislabeling and substituting an expensive item with a similar cheap item having the same color and texture, and adding chemicals to meet the required regulated quality standards. The adulterated product usually goes undetected due to the inability of consumer or retailer to identify the authenticity of food product [4] [6].

Apart from adulteration and contamination, a serious impact on food safety is spoilage. Consuming spoilt food lead to loss of nutrients and opens the door for a variety of illness due to microbial organisms such as bacteria. Food spoilage after reaching the consumer or retailer is the primary cause of food wastage in the United States. According to USDA, the estimated food waste in the United States is between 30-40% of the total food supply. In 2010, the economic research service of USDA reported approximately $161 billion worth of food was lost at the retailer and consumer levels [7]. American families throw out approximately 25% of the food they buy, cost ranging from $1,365 to $2,275 annually. This amount of waste has broad impacts on food security, resource conservation, and climate change. Food waste is the single largest component dumped into landfills resulting in landfills being the third largest source of methane in the US [7].

The impact of real-time monitoring of food and food products to prevent contamination or spoilage and promote tamper-free supply chain is huge ranging from saving lives to preventing economic and reputation losses for the trillion dollar food industry. Enabling affordable low cost technology to perform quality checks allows better control of food products at the producer level preventing contaminated or spoilt food from reaching higher levels of the supply chain. Empowering the retailer or consumer with the food product quality and traceability information will force the processor and distributor to adhere and enforce strict quality control standards since the brand and reputation are at stake. The real-time monitoring also allows the Federal agencies such as Food and Drug Administration(FDA), Department of agriculture (USDA), and Environmental Protection Agency (EPA) to regulate, enforce and monitor safety standards in the food industry. There is a growing need to develop technologies that promote an end to end monitoring of food products along the supply chain. The end goal is to ensure that the food reaching the fork meets the highest

safety standards.

Currently, there are a number of real-time tracking infrastructures such as Radio frequency identification (RFID), Electronic article surveillance (EAS), and bar codes providing supply chain traceability in the food industry [8] [9]. A typical RFID system consists of a tag or a transponder, a reader for interrogation and a database for storing data [10]. RFID tags are like labels that are attached to the food container or package allowing tracking of location across the supply chain. The identification data is uploaded real-time to the cloud for product tracking by interested parties such as retailers, producers and in some cases, the consumers. There are three types of RFID tags based on their interrogation technology, passive, semi-passive and active tags. The passive tags are battery less and uses the interrogation power for transmitting the information (ID) back to the reader. The passive tags are further classified into two broad categories; chipless and chip-enabled tags. The chipless tags are predominantly Inductor-Capacitor (LC) based short range resonators and the chip-enabled tags consists of a modulation circuitry to send the identification information with internal memory for storage [10] . A semi-passive tag utilizes the functionality of the passive tag and in addition to it, the tags leverages on battery assisted power to operate. An active tag relies completely on on-board power supply for transmitting the data. The power supply can be a battery or solar cell and allows long read range. Figure 1.1 shows the broad categorization of RFID sensors based on the interrogation technique and operating principle. The sensor element is incorporated as part of the passive or active RFID tag to detect the quality of food products as it moves along the supply chain.

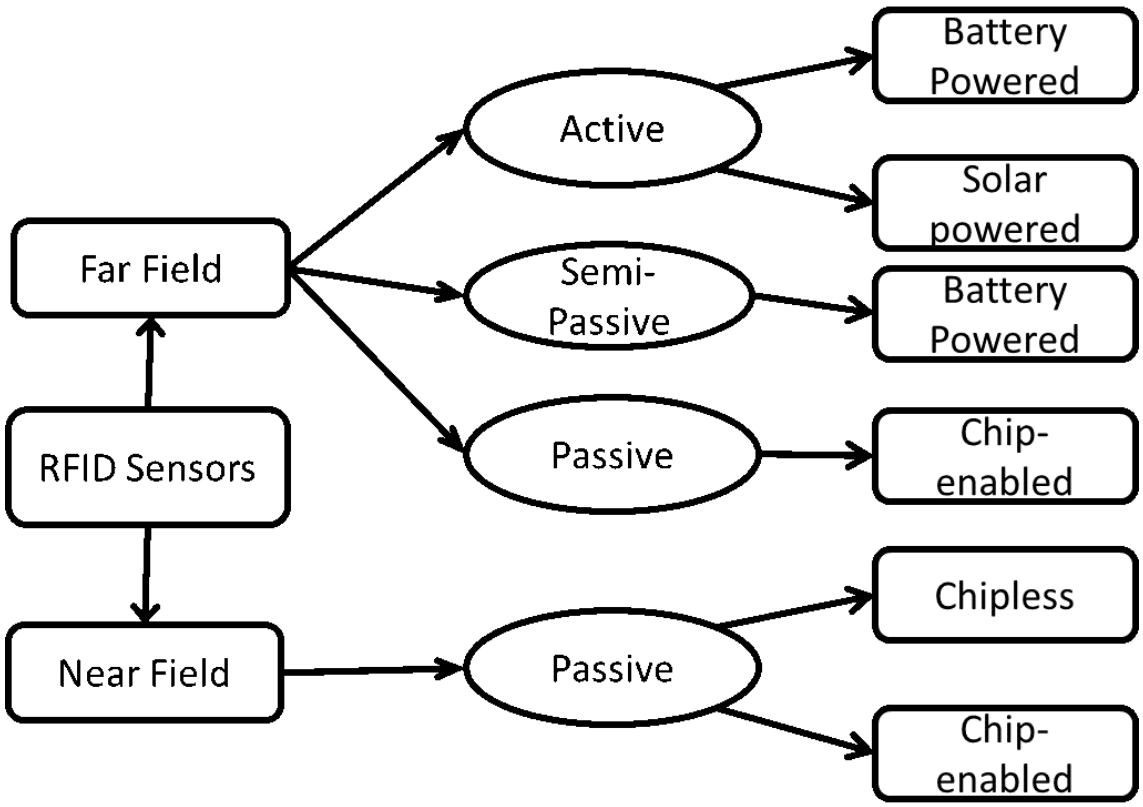

Figure 1.1: Types of RFID sensors based on the operating principle.

1.1 Wireless Food Sensors

The two major wireless tag categories are chip-enabled and chip-less sensor tags. In this section, a broad overview of different sensing functionalities of these two categories are presented.

1.1.1 Chipless sensor tags

The fundamental principle of operation of sensing for the chip fewer tags are based on inductive, capacitive or conductive coupling with the target under test. The sensitivity of these sensors depends on the coupling factor and are characterized by monitoring the change in frequency, phase or quality (Q)-factor of the sensor. The different techniques with

examples are listed in Table 1.1. Typically, chipless wireless sensor tags are near-field tags and have a shorter interrogation range.

Table 1.1: Sensing techniques for chipless tags

Parameter	**Coupling**	**Examples**
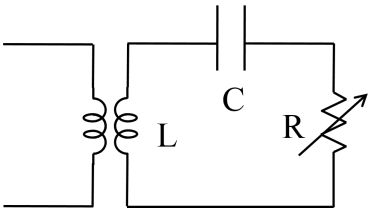	Conductive	Coating of a conductive layer on the sensor. Increasing conductive path of the antennas or growing antennas.
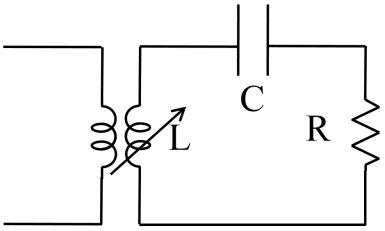	Inductive	Direct coating of a sensitive layer over the inductors.
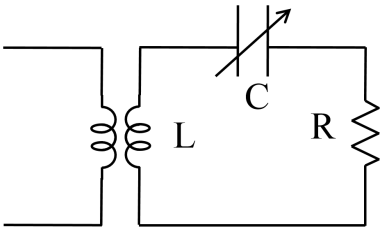	Capacitive	Dielectric loading. Change in effective capacitance due to change in bias voltage electrode potentials

1.1.2 Chip-enabled sensor tags

The chip-enabled tags have identification data associated with them. The sensor incorporated tags transmit the sensor data and identification data to the readout circuitry. The operation relies on the interrogation power of the reader or battery assisted power from the tag. The sensitivity of the passive tags depends on the change in operating frequency, read

range or power based on direct loading of the target. For the battery assisted tags, in general, an analog to digital converter or a microprocessor provides a digital readout of different sensing parameters. The following Table 1.2 lists different chip-enabled sensing mechanisms. Typically, chip-enabled tags are generally far-field with a longer interrogation range.

Table 1.2: Sensing Techniques for chip-enabled tags

Passive	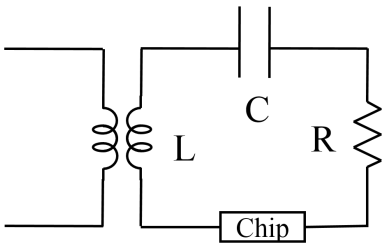	Coating of a sensitive patch on the tag. Dielectric or substrate loading of the tag
Semi-Passive	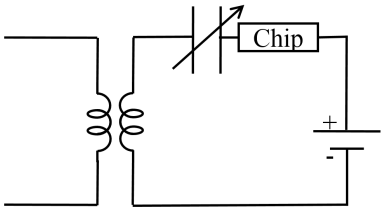	Battery assisted commercial sensors like temperature, humidity or electrodes such as pH coupled to passive tags
Active	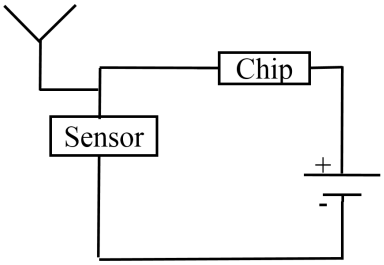	Electrodes and commercial sensors coupled to microprocessors and ADCs Digital readout like a bracon or transponder

1.2 Classification of Food Sensor Tags

The sensing element of the chip-enabled or chip-less RF tags monitor different parameters as markers for sensing. In case of food, the RF sensors are broadly classified based on

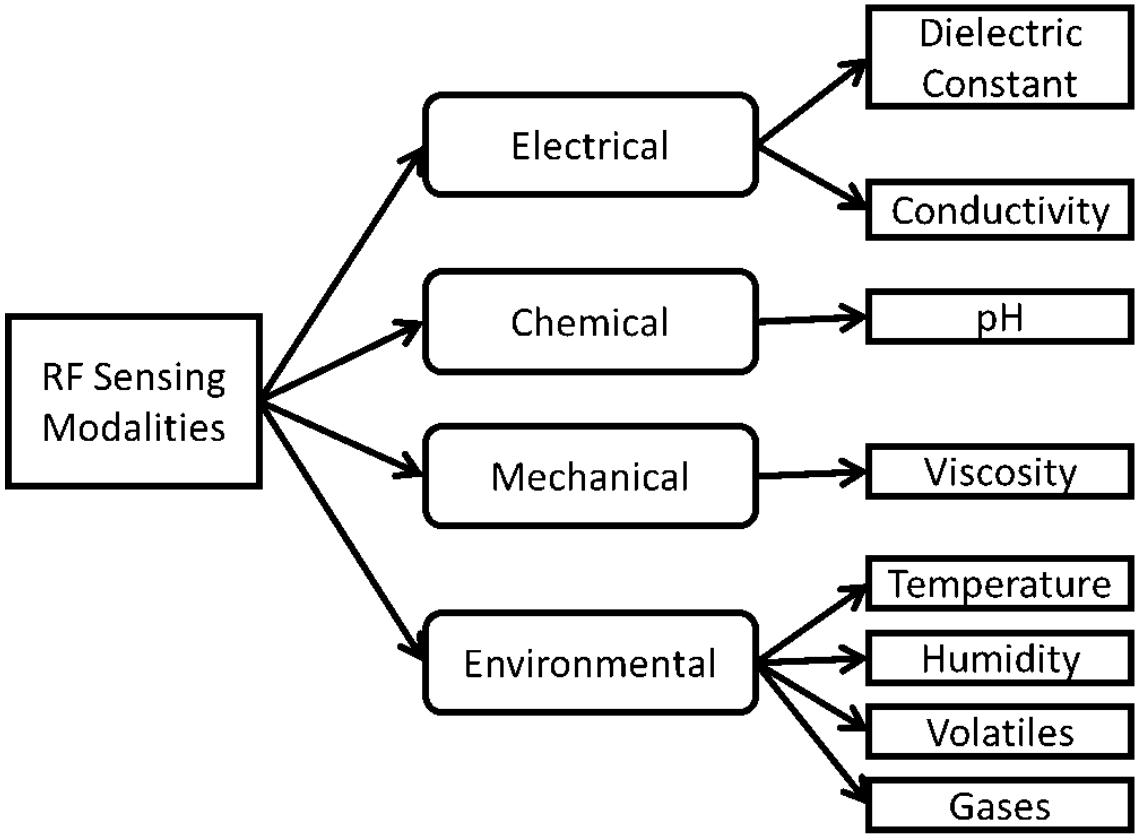

Figure 1.2: Classification of different sensing modalities that can be incorporated in RFIDs.

the monitoring parameter (sensing modality) into four major categories, Electrical, Chemical, Mechanical, and Environmental RF tags. These tags maybe invasive or non-invasive in nature. The monitoring parameter (For example: pH, dielectric constant, etc) should be in direct contact with the sensing element for detecting the quality of the food. Such type of sensors which require a direct contact with food are called as invasive sensors. For non-invasive sensors, the monitoring parameter (For example: temperature, humidity, etc) indirectly activates the sensing element for quality detection. The sensing element is not in direct contact with the food and monitors the target parameters without direct line of sight such as food volatiles or aroma. Figure 1.2 presents the broad categorization of different sensing modalities that can be incorporated in the RFIDs.

1.2.1 Electrical RF Tags

The electrical tags monitor the different electrical properties of food such as dielectric constant, loss tangent, conductivity, and resistivity. Typically, the detection technique employed is based on the conductive, inductive or capacitive coupling of the sensing element with the food. The change in an electrical property of food changes the coupling factor and leads to change in impedance, frequency, Q-factor, or read range of the RFID tag.

1.2.1.1 Dielectric Constant and Loss Tangent

The dielectric constant and loss tangent of food products are monitored for understanding the spoilage rate and freshness. As the food spoils, the dielectric constant and loss tangent increases or decreases based on the changes to the physical and chemical composition of the product. For invasive sensing, the RF sensor is placed on the surface of the food or immersed in the liquid food for monitoring. For example, [11] presented a chipless RF tag on a flexible pure-protein silk film substrate that can be easily adhered to the surface of food products such as apples, egg, tomatoes, cheese and bananas. The degradation of food leads to shape-deformation that shifts the resonance frequency due to effective dielectric change. For non-invasive sensing, the RF sensor is placed on the outer surface of the food container and capcitively coupled to the food for monitoring. This helps in prediction of shelf life and spoilage rate. In [12], a commercial RFID tag is placed on the surface of food for detecting spoilage rate in beef, pork and cheese by monitoring the change in the read range over time. The permittivity change is correlated to spoilage and in turn correlated to the read range. For example, [13, 14] presented a RF chipless sensor tag on the surface of a milk carton for determining the change in dielectric constant as milk spoils over time. The dielectric constant increases with microbial spoilage of milk and this capacitively loads the

sensor shifting the resonance frequency.

1.2.1.2 Conductivity or Resistivity

Typically, there are two techniques for detecting the change in conductivity, direct and indirect. In direct technique, the sensing element is immersed into the food and the change in conductivity is monitored over time. In indirect technique, the change in conductivity of food loads the impedance of the sensing element through capcitive coupling. In this case, the sensor is placed on the surface of the food. For example, in [15], an interdigitated RF sensor coupled with a screen printing compatible sensing film is used in which the resistivity of the film changes with an increase in amine concentration. The sensor is placed in contact with codfish in an enclosed chamber, and the resistivity is measured over time. As the fish ages, it releases trimethylamine which de-dopes the semiconductor film and increases the resistivity.

1.2.2 Chemical RF Tags

The chemical tags monitor the electrochemical changes due to change in chemical properties of food products such as pH over time for spoilage and freshness.

1.2.2.1 pH

The chemical tags monitor the pH of the food under test [16, 17]. Food pH level provides intuition on the shelf life of the food product since pH and spoilage rates are directly correlated. Typically, these tags consist of a pH sensitive electrode coupled to a passive or semi-passive RF tag. The pH-sensitive voltage change is used to change the bias voltage or capacitance of the RF tag leading to change in frequency and read-range. For example,

in [18], a RFID sensor embedded with pH sensitive electrodes for monitoring spoilage rate in fish and meat is presented. The iridium oxide electrodes fabricated on polyamide substrate and coupled to the RFID transponder are wrapped directly onto the fish meat and the pH is measured. As the pH changes (2-12), the electro chemical potentials generated by the electrodes changes and are converted to frequency varying signals; this is correlated to the spoilage rate. Another example is [19], a similar iridium oxide electrode with a varactor diode coupled to an inductor coil is presented for monitoring the pH of milk. The electrode is dipped in the milk, and as the milk spoils the pH decreases and changes the biasing voltage of the varactor diode which is monitored over time.

1.2.3 Mechanical RF Tags

The mechanical tags monitor the change in mechanical properties of the food product and correlate the change to spoilage or adulteration. Typically, the tags have an inherent natural resonance that changes with a change in density or viscosity of the food. Example of a mechanical tag is a magnetoelastic sensor (Metglas).

1.2.3.1 Viscosity or Density

Liquid food freshness and quality is analyzed by monitoring the viscosity of the food over time. For example, in [20], a magneto elastic RF sensor is presented for adulteration detection of extra virgin olive oil. The sensor has an inherent natural resonance that changes with change in viscosity of the liquid food. The RF sensor is dipped into liquid food and the change in viscosity is monitored over time.

1.2.4 Environmental RF Tags

The environmental tags are those that monitor in real-time the packaging environment parameters such as temperature, humidity, volatiles, food aromas, and gases. The RF tags are made inherent part of the package but are not in direct contact with the product under test. The sensors help in predicting the shelf-life, discoloration, freshness, and spoilage rate of food. The sensors have a parameter sensitive film, electrode or layer coupled to the RF tag that changes as the monitoring parameter changes. This loads the impedance of the tag and thereby changes the resonance frequency or read range.

1.2.4.1 Temperature

The packaged foods are subjected to different temperature cycles across the supply chain from packer to the consumer. It is important to monitor the temperature variations to predict the shelf life and freshness of perishable food products such as fruits, vegetables, milk, and meat. For example, [21] proposed a passive chipless RF temperature sensor with a dual band resonator and a varactor diode biased by negative temperature coefficient resistor. As the temperature changes, the biasing voltage changes and shifts the resonance frequency of the dual resonator. Furthermore, there are a number of studies that employ active or semi-passive temperature sensors that are used for monitoring temperature across the perishable food supply chain. These sensors help in alerting the transporter if the temperature falls below the minimum standards. For example, [22] studied the performance of three semi-passive and one active RFID sensor for temperature mapping along the pineapple supply chain (ThermAssure RF, ALB-2484, ThermaProbe RF, and ILR i-Q 32T). The tags were placed on different parts of the pineapple palette to understand the temperature dynamics.

1.2.4.2 Humidity

The presence of moisture inside the packaged dried foods is not desirable and leads to spoilage. Monitoring the presence of moisture is vital for increasing the shelf life of dried foods such as cereals, chips, crackers, and snacks. For example, in [23], a passive chipless sensor is proposed for humidity detection. The sensor design consists of an interdigitated capacitor on a cellulose-based substrate that is capable of changing the resonance frequency when exposed to moisture. In [24], an interdigitated RFID sensor coupled to a microcontroller is presented for detection of humidity in mushroom packages.

1.2.4.3 Food Volatiles and Gases

Fresh produce such as fruits, vegetables, and dairy products release volatiles as it ages. The volatile profiling of the packaged environment gives an insight to the freshness and state of the monitored food. Food aroma is an important marker for non-invasive quality monitoring. A large number of sensitive coatings are available that have higher affinity towards certain specific volatiles which determine the food quality. A few examples are, in [25], a lutetium bisphthalocyanine coated indium tin oxide electrodes are proposed for detection of aroma volatiles of oil and wine. A platinum interdigitated electrode coated with zinc oxide is proposed in [26] for identification of ethanol concentration in different brands of tequila. An Al or Au interdigitated capacitor coated with molecular imprint polymer is presented in [27] for sensing limonene volatiles emitted during ripening process of mangoes. In the above examples, the sensor film when in contact with the target volatile loads the interdigitated capacitor and shifts the resonance frequency.

1.3 Modified Supply Chain Sensors

The different types of sensing modalities discussed in the previous section offer a myriad of solutions for monitoring the quality of food along the supply chain independent from the current tracking infrastructure. Integrating these sensors along with the current infrastructure is necessary to promote a "value-centric" approach of supply chain management. The current RFID tracking infrastructure provides just the traceability information for the products and there exist a need for improving the infrastructure to provide both the traceability as well as the sensing information simultaneously for enhanced and real-time quality control. Figure 1.3 presents a modified supply chain with sensor integrated RFIDs for improving visibility.

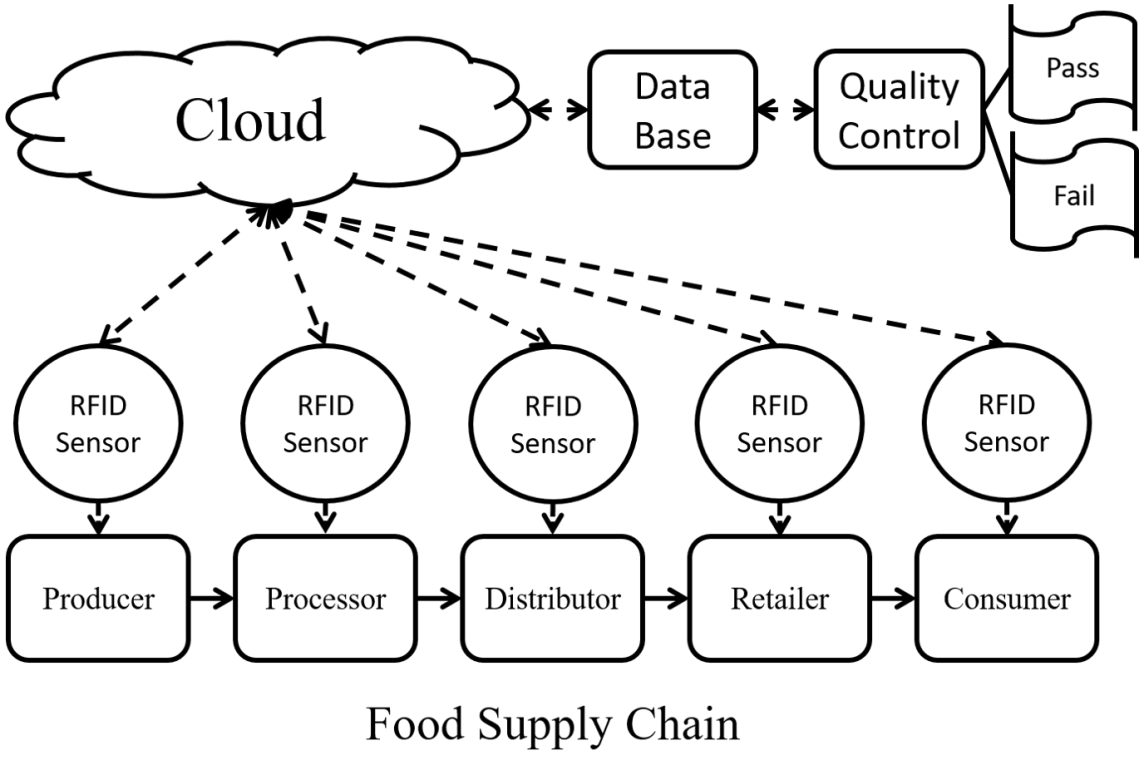

Figure 1.3: Modified Food Supply Chain Tracking Infrastructure.

1.3.1 Modified RF Sensor Tag

The proposed idea is economically viable only if the existing reader infrastructure is used without significant modification. In this case, the sensor tag should be modified such that it is able to transmit both identification data as well as the sensor data. Furthermore, the current RFID tags are ultra-low cost, battery free and passive in nature. To maintain such specifications in the modified version, the tag should satisfy the following constraints:

- Battery-free and passive.
- Ability to harvest energy from the reader signal to activate the associated electronics.
- Low power consumption for the digital modulation as well as for retrieving the anolog sensor data.
- Multiple sensor integration that monitors different target markers simultaneously.
- Identification as well as sensor data digitization.
- Miniaturized and fabricated on a food packaging compatible flexible substrate.
- Longer read range and ultra low cost with ability to mass commercialize using conventional manufacturing techniques such as roll-to-roll.

The goal is to satisfy the above mentioned specifications and to design a sensor integrated RFID tag. The modified tag consists of an antenna for communication, an integrated chip with the associated digital electronics, and a sensing unit with single or multiple sensing elements. An envisoned modified supply chain based on passive sensor integrated RFID tags with multiple sensing elements on a single low cost flexible tag is shown in Figure 1.4.

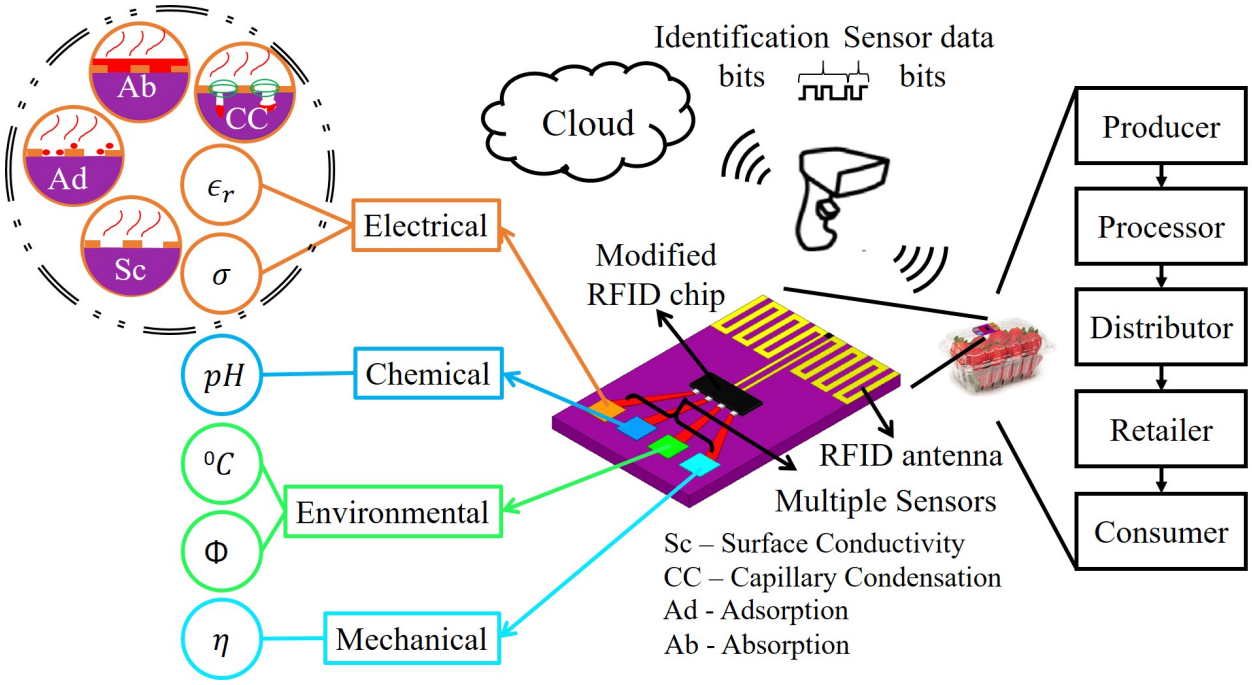

Figure 1.4: Envisoned modified supply chain with sensor integrated RFIDs.

1.4 Summary of Dissertation Contributions

This section will summarize chapter by chapter contribution for the development of wireless sensing techniques for enhancing visibility across the supply chain. The main contributions are

- *In Chapter 2, a hybrid sensing approach for detecting change in dielectric constant and viscosity of target liquid is developed allowing two-factor authentication.* The wireless passive sensor consists of two magnetoelastic strips in parallel coupled to an inductor coil to form a wireless LC tank. The natural resonance of the strips is affected by the viscosity of the liquid food and the resonance due to the formation of the LC tank is affected by the dielectric constant of the liquid food. Both the resonances are read out using a single reader coil forming a wirless short range system. The proposed sensors are evaluated for determining the adulteration levels in extra virgin olive oil.

- *In Chapter 3, a sensing approach that utilizes 3D printed RF sensors coupled to a microfludic channel for liquid profiling is developed for food quality control.* Two different resonators are presented, a 3D printed cavity and a 3D printed split ring resonator. Both the resonators use a microfludic channel through which the target liquid is introduced for identification. These sensors can be easily made as a part of a "'smart"' vial to monitor dielectric constant of liquid food as it passes through different layers of the supply chain. A passive UHF RFID tag is also 3D printed and demonstrated to showcase the applicability of a low cost alternate fabrication technique in manufacturing supply chain sensors.

- *In Chapter 4, an interdisciplinary approach for detecting bacterial count in liquid food matrices using RF sensors is developed for contamination detection.* The technique

uses carbohydrate coated conductive nano particles to capture the bacteria in liquid food and impedance load the RF sensor for indirect estimation of bacterial count. Two RF sensing approaches using different sensing elements are developed, a metamaterial inspired split ring sensing element for the wired approach and an interdigitated capacitor coupled to an inductor for the wireless approach. A "smart" vial is developed using the confluence of nanoparticles and RF sensing elemenets and are evaluated for determining bacterial levels in milk.

- *In Chapter 5, a new sensing approach that uses capillary condensation phenomenon on a porous substrate for detection of food volatiles is developed for spoilage detection.* The technique uses an interdigitated sensing element fabricated on a porous substrate into which the volatile molecules condenses changing the effective dielectric constant of the substrate and inturn the effective capacitance of the interdigitated element. A inductor is coupled to the sensing element for enabling short range wireless communicaiton. The resonance frequency of the LC tank is read out using an external pick up coil and it changes with change in the volume and type of condensate in the pores. The technique is evaluated for volatile profiling of food aroma.

- *In Chapter 6, a sensing approach that uses absorption of food volatile molecules and gases onto different thin film coatings with improved specificity is develeoped for spoilage detection.* The technique uses interdigitated capacitor with a thin-film coating as a sensing element. Two approaches are presented; volatile sensor, and gas sensor. For the first approach, thin film of two different photoresists are coated onto the sensing element; SU8 and S1813 and evaluated for enhancing or selectively blocking certain food volatiles. For the second approach, a thin film of conductive polymer which has a

very high affinity towards Ammonia is coated onto the sensing element and evaluated for sensitivity and specificity. The sensor is capable of detecting 3 ppm of Ammonia under room temperature and atmospheric pressure.

- *In Chapter 7, a sensor integrated RFID tag is developed that is compatible with existing RFID infrastructure for detecting Ammonia gas concentration in packaged food.* The modified sensor tag consists of a digital modulation circuit from [28] that converts the analog sensor data into digital bits and transmits them along with the identification information back to the reader. The sensor tag along with the digital circuitry is evaluated for detection of Ammonia gas which is a spoilage marker for protein rich food products. This sensor tag is capable of converting the analog data of the different sensing elements developed in the previous chapters to digital bits showing a path forward to integrate multiple sensors using a single passive tag to enhance visibility of the supply chain.

Chapter 2

Dielectric Based Sensors For Adulteration Detection

2.1 Introduction

The first topic investigated is to develop a RFID compatible low cost wireless passive sensor for detection of food adulteration. Food fraud and economically motivated adulteration of liquid food has become a rampant problem in the United States and around the globe [4, 6, 29, 30]. This kind of fraudulent and intentional tampering of food has led to several hundred deaths and disease outbreaks [4]. The adulterated product usually goes undetected due to the inability of a consumer to identify the authenticity by visual inspection or smell. Liquid foods such as milk, oil, fruit juice, honey, yogurt and alcohol are most vulnerable to adulteration. The most common practice in liquid food adulteration is, mislabeling and substituting an expensive liquid item with a cheaper but similar item having the same color and texture. For example, mixing very expensive extra virgin olive oil with other edible oils or non-food grade oils. Another common practice is to add chemicals to the liquid food to meet certain commercial standards. For example, addition of melamine to enhance protein content in milk [31] or the addition of malic acid to enhance acid content in fruit juices [32]. There is a pressing need for the development of new technologies to detect adulteration, in particular, adulteration of extra virgin olive oil. Olive oil is one of the leading food categories with

the highest reported case of food fraud in the United States [4]. Common liquid detectors are based on properties of liquids such as conductivity [33], viscosity [34] and dielectric constant [35]. Most of the sensors reported in the literature often measure a single liquid property of the target. However, it is desirable to have simultaneous measurement multiple properties in order to get two factor authentication and quality control. This enhances the sensitivity, specificity, and reliability of the sensor, and is often difficult to defeat. Hybrid sensors and sensor arrays have often been used in chemical sensing, food sensing, and quality control of food and agricultural products [36]. In addition to hybrid sensing, wireless sensing is required for characterizing parameters without direct line of sight or physical contact with the sample. The growth of hand-held wireless devices makes a wireless sensing approach more attractive for building a low cost sensing system [37]. A good candidate for hybrid sensing is magnetoelastic strips. Magnetoelastic strips have been previously used for sensing parameters such as temperature, humidity, stress, density, pH, displacement, viscosity, and magnetic fields [38].

Magnetoelastic strips are amorphous ferromagnetic material with high magnetostriction and magnetoelastic coupling coefficients [39]. When subjected to a time varying external magnetic field, the magnetoelastic strips deform along their length and convert magnetic energy to elastic energy. Due to high magnetostriction, they exhibit a magnetoelastic resonance which is inversely proportional to the length of the strip. This resonance can also be detected wirelessly using a pick up coil [39]. The hybrid sensor proposed in this chapter utilizes simultaneous measurement of electrical (dielectric constant) and mechanical (viscosity) properties for quality control of liquid food. It is beneficial to use two factor sensing as it allows an additional reference for cross checking. Hybrid sensors are necessary for sensing liquid mixtures, for example, different types of milk may have similar viscosity but differ-

ent dielectric properties, or different types of oil may have different dielectric and different viscosity properties.

Two different sensor designs approaches are porposed and evaluated in this chapter, Sensor-1 and Sensor-2. Sensor-1 uses a parallel plate capacitor integrated with an independent amorphous ferromagnetic magnetoelastic strip (Metglas), and an inductor coil. The coil is coupled to the capacitor to form a resonant LC tank. Additionally, the coil allows wireless interrogation of the sensor by the external pickup coil. In Sensor-2, the capacitor is designed using two parallel mounted magnetoelastic strips separated by a spacer. An inductor coil is attached to the capacitor to form an LC resonator. This coil also allows for wireless interrogation of this LC tank. The electrical and mechanical resonances are detected using the same pickup coil and the unit is integrated into the cap of a vial making it the smart vial. Since both properties are detected simultaneously, one can be used as an inbuilt reference for enhanced specificity.

2.2 Design and Fabrication

Two different design approaches are investigated for the hybrid sensor, termed here as Sensor-1 and Sensor-2.

2.2.1 Sensor-1 Design

Sensor-1 consists of an LC tank for dielectric sensing and a magnetoelastic strip (Metglas 2826MB) for viscosity sensing that are independently mounted, see Figure 2.1. The LC tank consists of an inductor coil (diameter = 30 mm) and a capacitor comprised of two identical copper plates separated by dielectric spacers placed on both ends forming an electrical res-

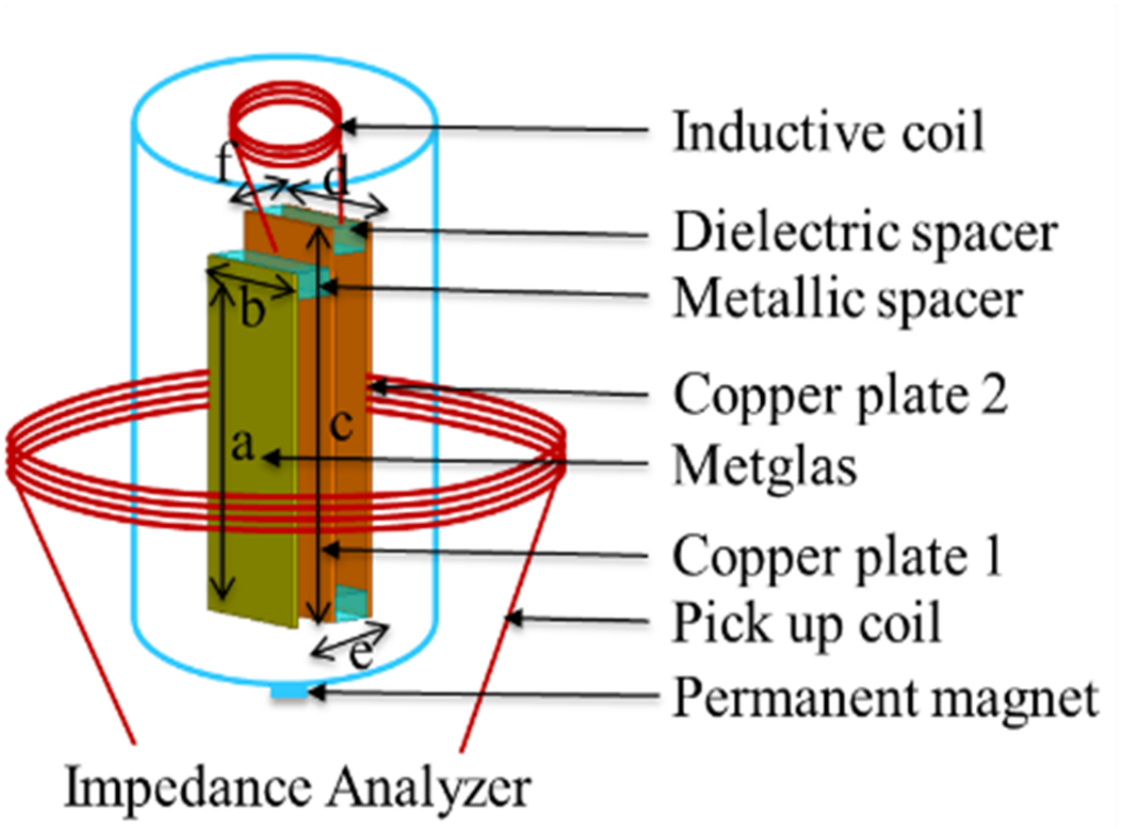

Parameter	a	b	c	d	e	f
Dimensions (mm)	21	9.5	40	10.7	2.52	2

Figure 2.1: Schematic of hybrid Sensor-1 using a parallel plate capacitor in parallel to a magnetoelastic strip along with the dimensions.

onator. The inductor coil serves the additional purpose of coupling to an external pick up coil for wireless interrogation of the electrical resonance. The magnetoelastic strip attached in parallel to the capacitor separated by a copper spacer forms the mechanical resonator. The magnetoelastic strip has its own independent mechanical resonance that can also be detected wirelessly by the external pick up coil. A permanent magnet is placed at a fixed position below the vial to provide DC field for the magnetoelastic strips.

2.2.2 Sensor-2 Design

The Sensor-2 consists of an LC tank made up of an inductor coil (diameter = 30 mm) and parallel plate capacitor comprised of two magnetoelastic strips (Metglas 2826MB) separated by a dielectric spacer on one end. The magnetoelastic ribbons are conductive in nature and thus can be used to form a parallel plate capacitor. The capacitor is used for dielectric sensing by tracking the LC resonance (electrical) due to change in capacitance between the strips. The two strips are designed to have the same widths but a small difference in lengths to provide different mechanical resonances adjacent to each other in frequency. The second resonance can be used as a built in reference if the resonance peak is traced relative to each other or to gain additional data for higher accuracy in measurements. Figure 2.2 shows the schematic of Sensor-2 along with the dimensions. Sensor-2 has a much simpler design in comparison to Sensor-1 as the LC tank independently becomes a hybrid resonator having both electrical and mechanical resonances and can be used for tracking a simultaneous change in the dielectric constant and viscosity of the liquid under test. In the future it can also be used to study electrical-mechanical non-linear properties of samples.

2.3 Theory

The natural frequency of the magnetoelastic strip can be approximately calculated by solving the equation for beam deflection from the classical Euler-Bernoulli beam theory [40]. This estimated natural resonance for Metglas can be tailored to the frequency of interest to make it compatible with existing RFID frequency standards.

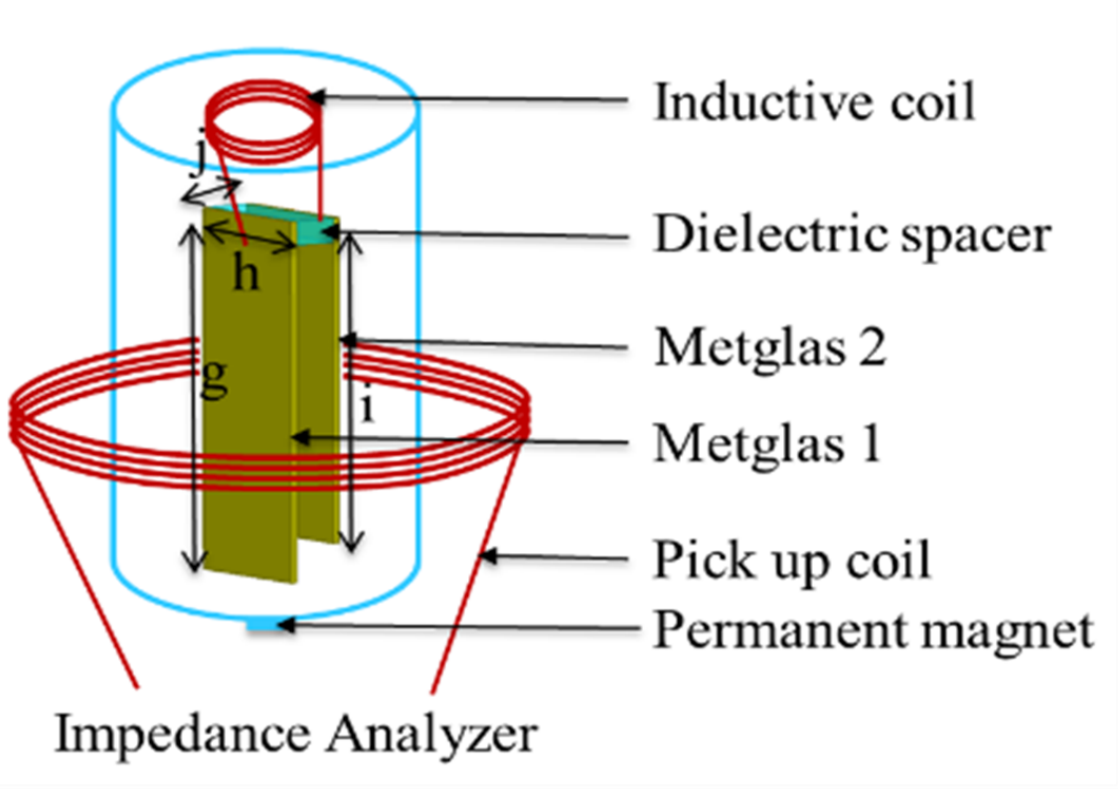

Parameter	g	h	i	j
Dimensions (mm)	30	9.5	25	0.54

Figure 2.2: Schematic of hybrid Sensor-2 using a parallel plate capacitor in parallel to a magnetoelastic strip along with the dimensions.

2.3.1 Modified Beam Equation

The beam equation is solved by applying the boundary conditions of a cantilever beam. The boundary conditions are:

1. displacement and slope at the clamped end are equal to zero, and

2. momentum and shear at the free end are equal to zero.

The natural frequency of a cantilever under vibration is given by the following formula 2.1 and the values are listed in Table 2.1.

$$\omega_n = \alpha_n^2 \sqrt{\frac{EI}{\rho A l^4}},\ where\ \alpha_n = \beta_n^2 L^2,\ and\ \beta_n L = \frac{(2n-1)\pi}{2} \tag{2.1}$$

Table 2.1: Parameters for calculating the natural resonance

Parameter	**Values**
Length of the cantilever beam (L)	0.021 m
Elastic modulus of the Magnetoelastic strip 2826MB (E)	100 GPa
Density of the strip (ρ)	7900 kgm^{-3}
Area of the strip (A)	0.19*10^{-6} m^2
Moment of Inertia (I)	6.33*10^{-18} m^4

2.3.2 Natural Resonance Estimation

The calculated fundamental resonance for the magnetoelastic strip using the values listed Table 1.2 is 26 kHz. The magentoelastic strips and the inductor coil are made as an integral part of the cap of a smart vial. The resonance frequency of the magnetoelastic ribbons excited by an external magnetic field is detected by measuring the impedance of the coil as a function of frequency. Alternatively, it can also be measured by picking up the time varying magnetic flux created due to an inverse magnetoelastic effect. This effect leads to deformation or vibration of the strip which is detected using a pick up coil placed near the strip [34]. Change in the resonance frequency due to mechanical loading is used to measure viscoelastic properties of different liquid samples.

2.3.3 Equivalent Model

Figure 2.3 shows the equivalent model of the sensor setup for both designs. The resonance frequency (electrical and mechanical) of both sensors is measured wirelessly using a single

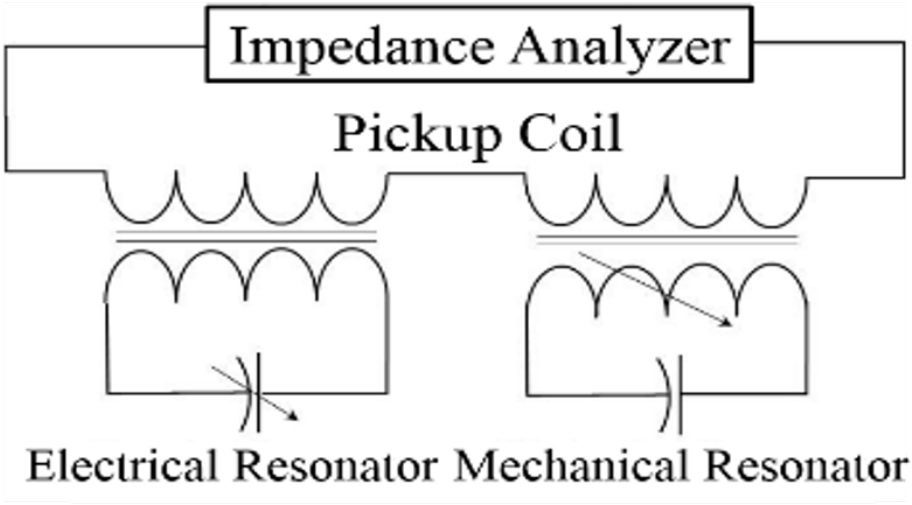

Figure 2.3: Equivalent model of the sensor.

pick up coil connected to an impedance analyzer (HP4194A).

2.3.4 Sensor-1 Unloaded Resonances

Figure 2.4 and Figure 2.5 shows the measured impedance and phase as a function of frequency for both electrical and mechanical resonances for Sensor-1. The electrical resonance is at 12.63 MHz and the fundamental mechanical resonance peak is at 45.04 kHz. However, for the mechanical resonance, the stronger and sharper resonance with higher signal to noise ratio occurs at higher order harmonics (243.65 kHz), and hence this is selected for all the measurements.

The measured natural resonance (mechanical) of Sensor-1 is at 45.05 kHz. The mismatch between the measured and calculated natural resonance is due to constraints such as (i) the beam equation does not take into account the magnetoelastic effects, (ii) the equation calculates the resonances in a vacuum environment and, (iii) the equation is for unrestricted free cantilever beams, but in reality the magnetoelastic strip is restricted by the positon and

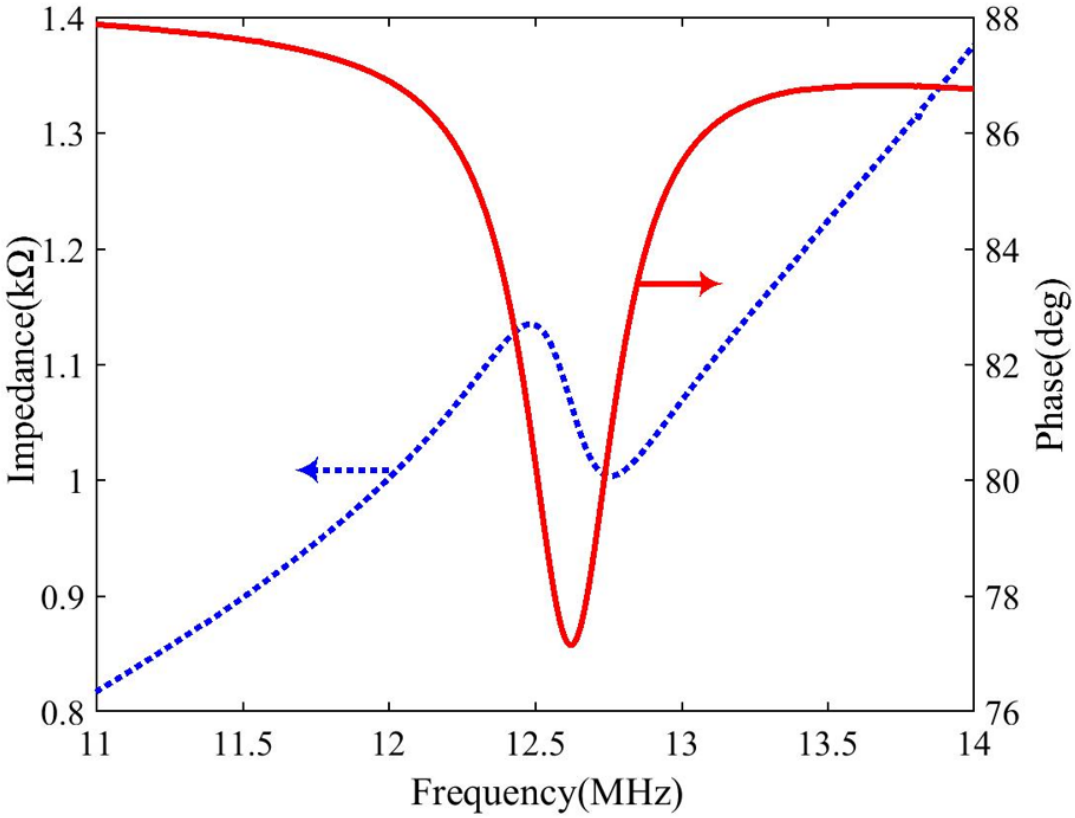

Figure 2.4: Measured electrical resonance for Sensor-1.

placement of a permanent magnet in its vicinity that provides the DC magnetic field.

2.3.5 Sensor-2 Unloaded Resonances

Figure 2.6 and Figure 2.7 show the measured impedance and phase as a function of frequency for electrical and mechanical resonances, respectively, for Sensor-2.

The electrical resonance is at 10.665 MHz and the two higher order mechanical resonances, due to two magnetoelastic strips, are at 241.85 and 246.5 kHz. Similar to Sensor-1, the resonance at higher order harmonics are sharper having higher signal to noise ratio and hence this is selected for all further measurements and is shown in Figure 2.7.

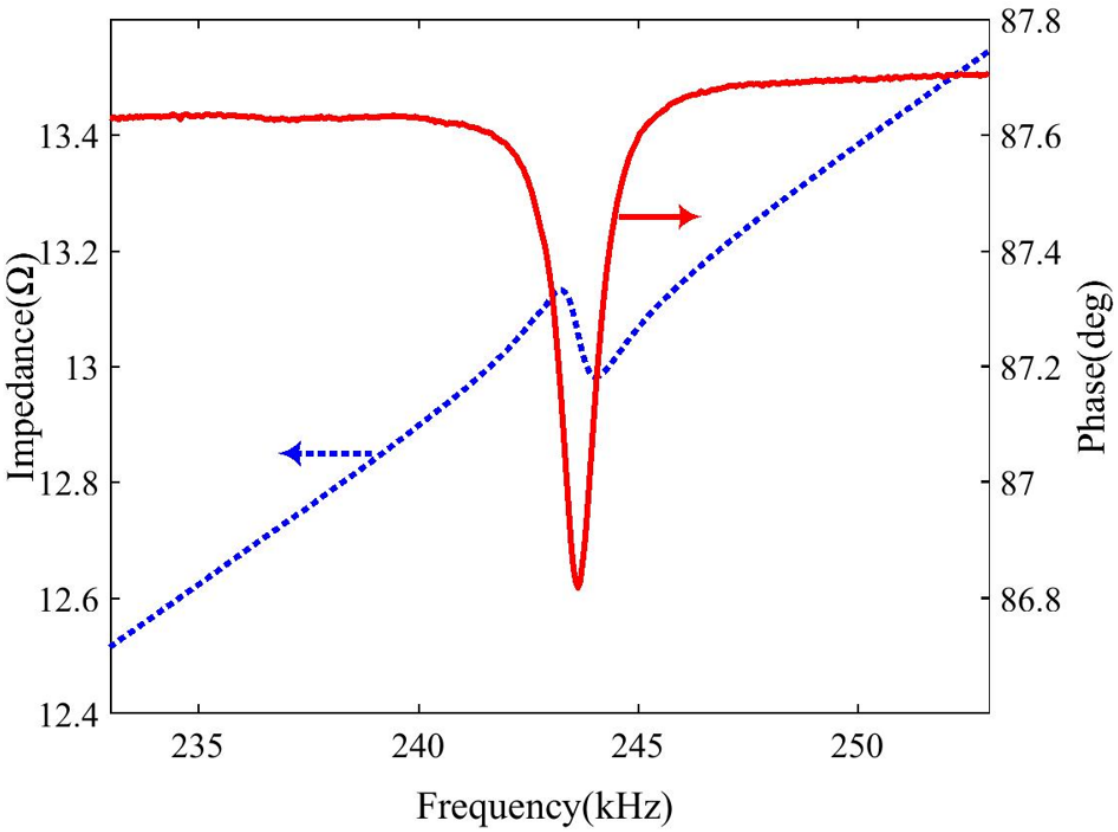

Figure 2.5: Measured mechanical resonance for Sensor-1.

2.4 Measurement and Characterizationn

2.4.1 Dielectric Reference Measurements

Oil and glycerine samples will be used to demonstrate the hybrid sensing capability of the proposed sensors. The samples are characterized first to extract the real part of the dielectric constant. This provides a reference for evaluation of the smart vial as a dielectric sensor. The measurement of frequency dependent dielectric constant for different liquid samples is performed using a simple parallel plate capacitor design. The dielectric properties are extracted by filling the liquid in between the parallel plates of a capacitor [41]. The accuracy of the measuring technique is verified by comparing the measured dielectric constants of

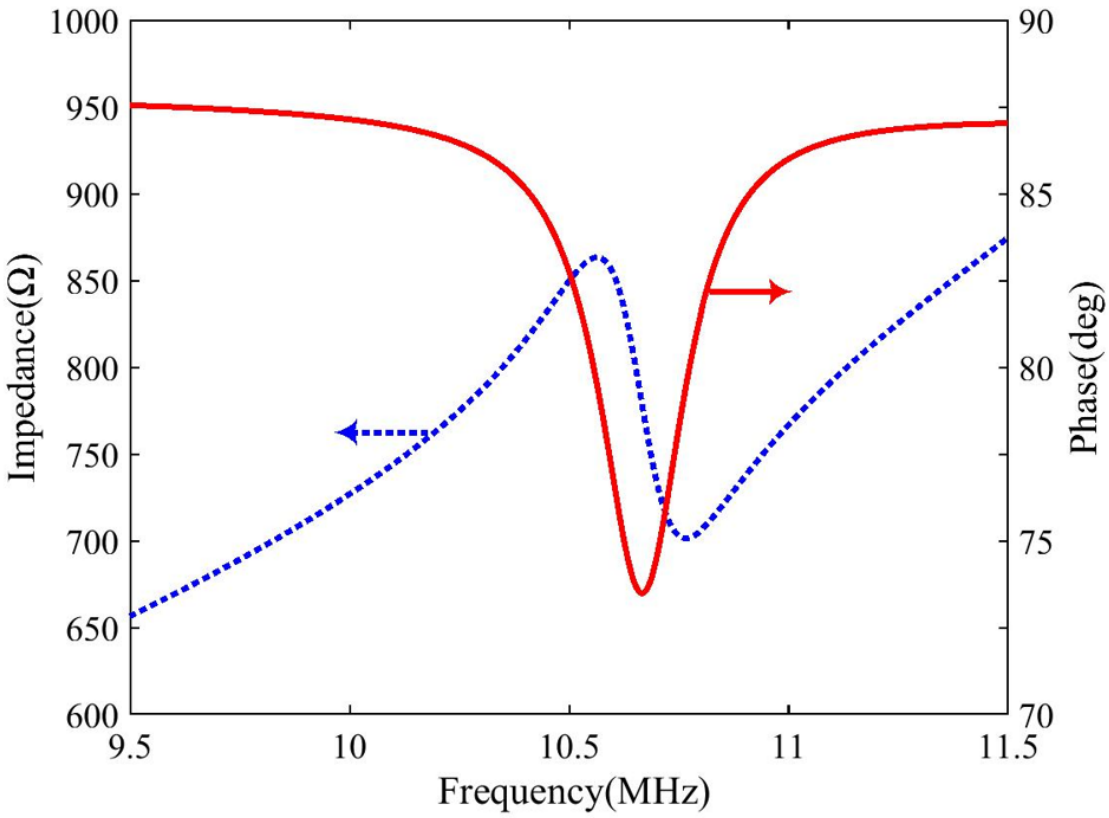

Figure 2.6: Measured electrical resonance for Sensor-2.

known samples measured with the data available in the literature.

2.4.1.1 Extraction of Dielectric Constant

The procedure for extracting the real part of the dielectric constant is outlined as follows. The capacitance (C) of a parallel plate capacitor is given in 2.2

$$C = \frac{\epsilon_r \epsilon_0 A}{d} \tag{2.2}$$

where, ϵ_r is the dielectric constant of the material, ϵ_0 is the permittivity of free space, A is the area of the plate, and d is the separation between the two plates. The dimensions

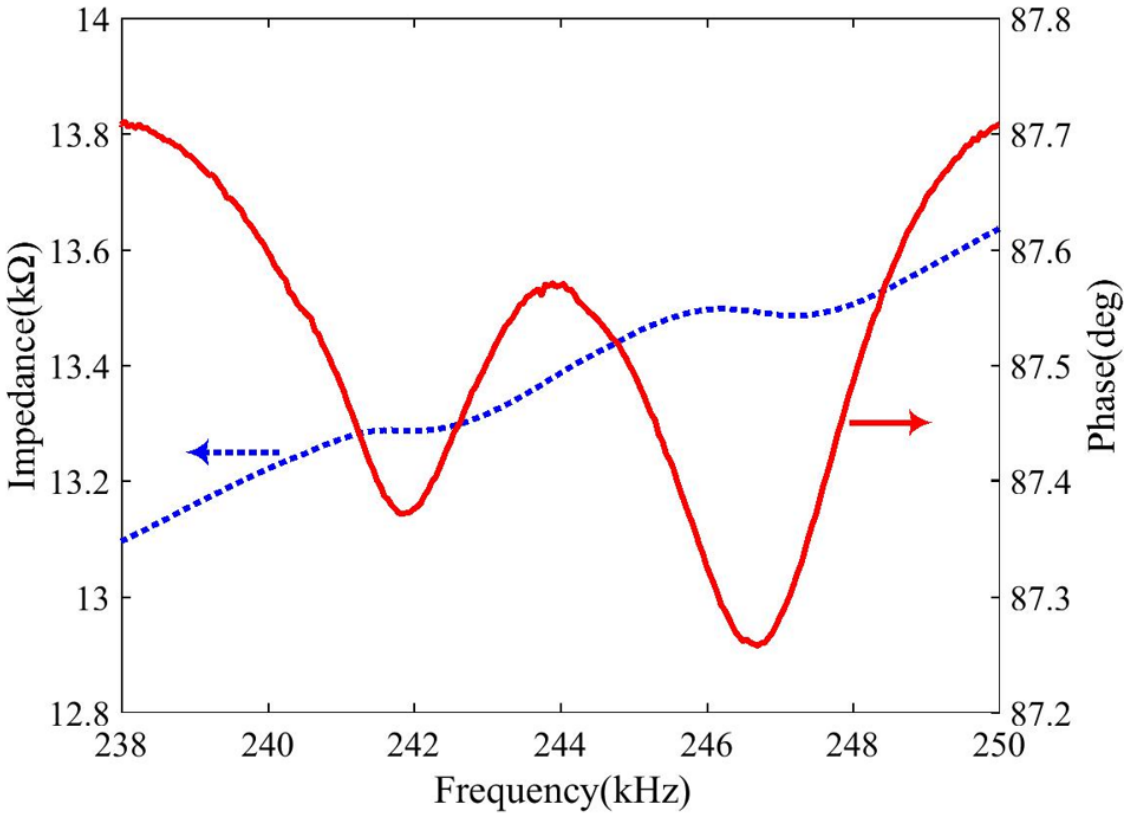

Figure 2.7: Measured mechanical resonance for Sensor-2.

of the copper plates are listed in Figure 2.1. The plates are separated by a narrow width dielectric spacer of 3 mm length, 10.7 mm width and 0.5 mm thickness on both ends as shown in Figure 2.8.

The parallel plate capacitor is characterized first to estimate the error capacitance due to various sources such as the wires connecting the impedance analyzer, solder joints, fringing capacitance and other parasitic capacitances. A set of materials with known dielectric constants such as air, iso-propanol and methanol are used for this estimation. The capacitor is immersed in containers with known liquids such that the liquid fills the gap between the parallel plates. The capacitance is recorded on the impedance analyzer by sweeping the frequency over 3-24 MHz range. The error capacitance due to fringing fields and other par-

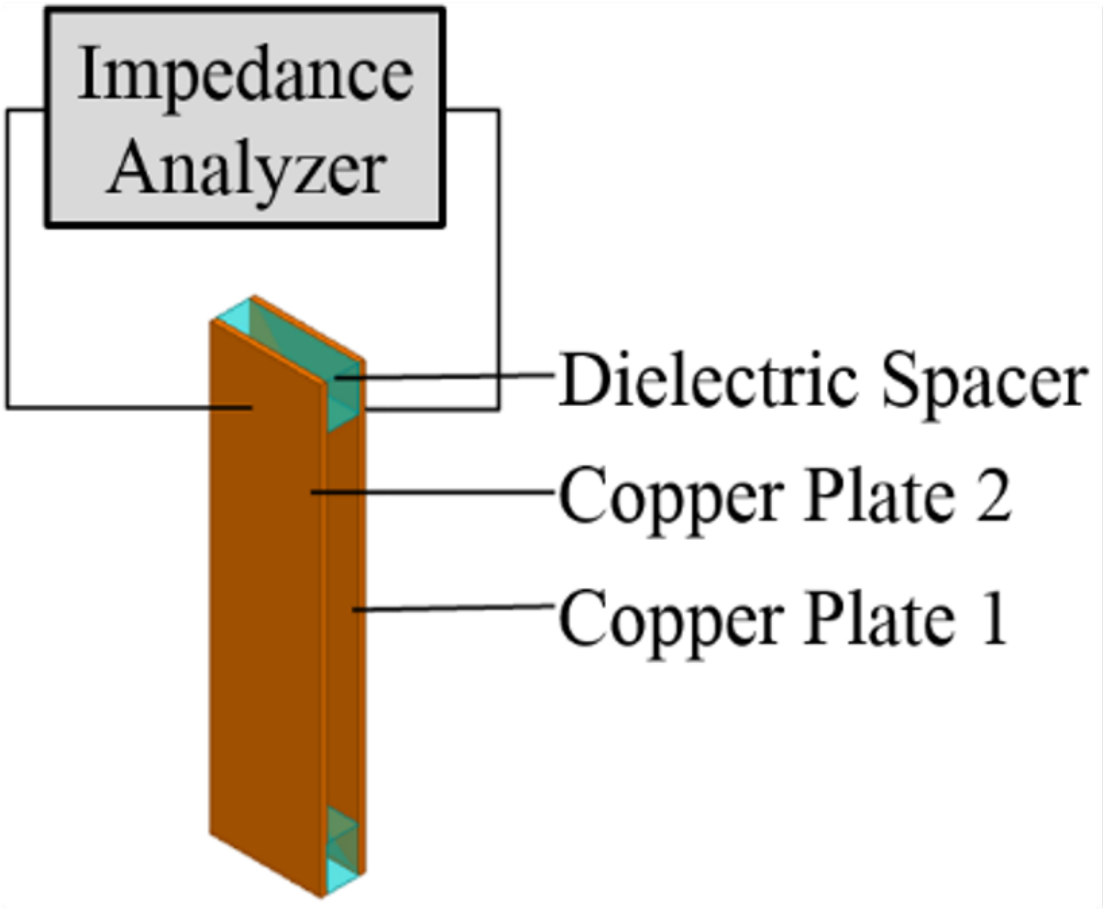

Figure 2.8: Schematic of the experimental setup for dielectric constant extraction.

asitics at each frequency is theoretically calculated. The real part of the dielectric constant is extracted by using the following formula in 2.3.

$$\epsilon_r = \frac{C_{measured} - C_{error}}{C_{air} - C_{error}}, \ where\ C_{error} = C_{fringe} + C_{Parasitic}. \tag{2.3}$$

The dielectric constant (ϵ_r) of the unknown liquid is independent of the area and spacing between the parallel plates. Using 2.3, the real part of the dielectric constant of any unknown liquid can be extracted over the measured frequency range.

2.4.1.2 Glycerine-DI water

The first set of experiments is carried out to validate the accuracy of the method proposed. Three different concentrations of glycerine DI-water samples are measured and compared to values reported in literature. The liquids were mixed at room temperature using percent by volume ratio. Table 2.2 lists the measured dielectric constant and available literature data for the three samples. The measured values are very close to reported data in the literature.

Table 2.2: Dielectric Constants and Viscosity of different Glycerine- DI water mixtures

Glycerine Concentration %	**Viscosity (cP)** [42]	ϵ_r [43]	ϵ_r **measured at 14.5 MHz**
65	15.2	-	59.98
70	22.5	57.06	57.05
80	60.1	52.27	51.89

2.4.1.3 Oils

The second set of experiments is done to extract the dielectric constant of different types of oils. The oils were purchased from a local grocery store and the experiments were carried out at room temperature (22 ^{o}C). Figure 2.9 and Figure 2.10 show the plots for dielectric constant of different oils over a measured frequency range of 3-24 MHz.

2.4.1.4 Oil Mixtures

The third set of experiments is carried out to demonstrate the dielectric constant change due to mixing of different oils (extra virgin olive oil and corn oil). Figure 2.11 shows a plot for real part of the dielectric constant of the mixture, by volume ratio, over a frequency

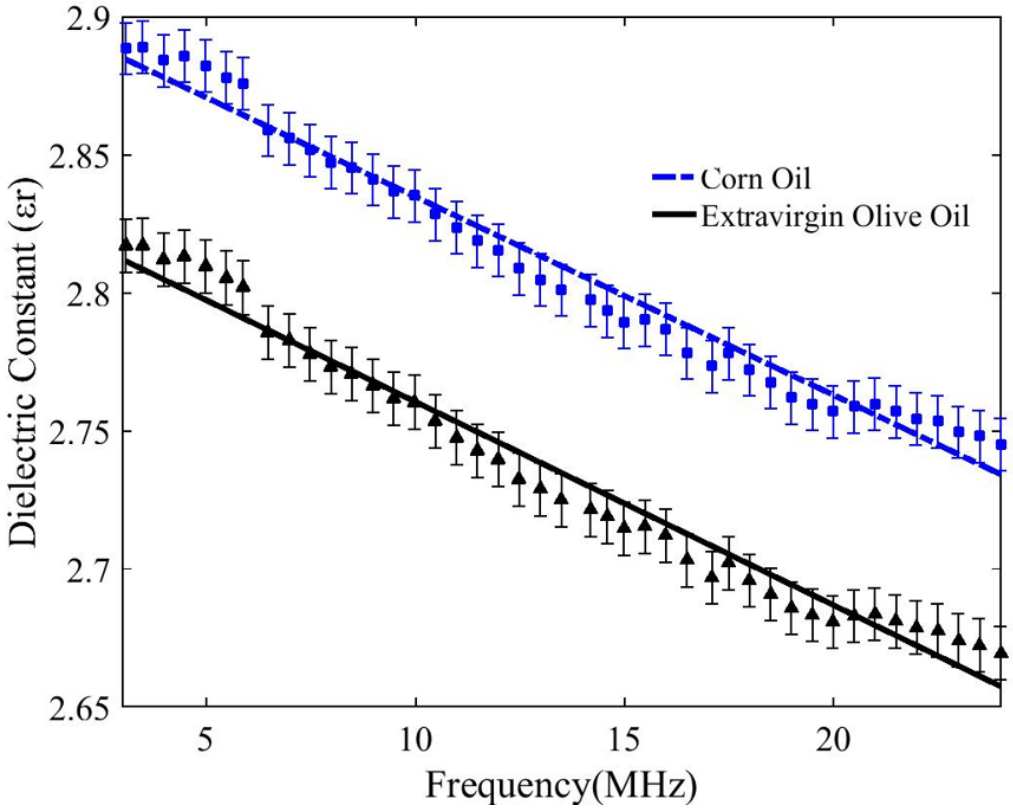

Figure 2.9: Measured dielectric constants for corn and extra virgin olive oil.

range of 3-24 MHz. The change in dielectric constant with mixing ratios verifies that the hybrid sensor can be successfully adapted as a dielectric sensor by monitoring the shift in the electrical resonance.

2.4.2 Reference Testing

The hybrid sensing capability of the smart vial is demonstrated by simultaneous sensing of viscosity and dielectric constant of different glycerine and DI-water mixtures using both sensors. Glycerine DI- water mixtures were selected as a reference to test the performance of the sensors since it offers a wide range of dielectric constant ($\epsilon_r = 53 - 79$) and viscosity (1-60 cP) to test [41,43]. Mixing is done at room temperature using percent by volume ratio

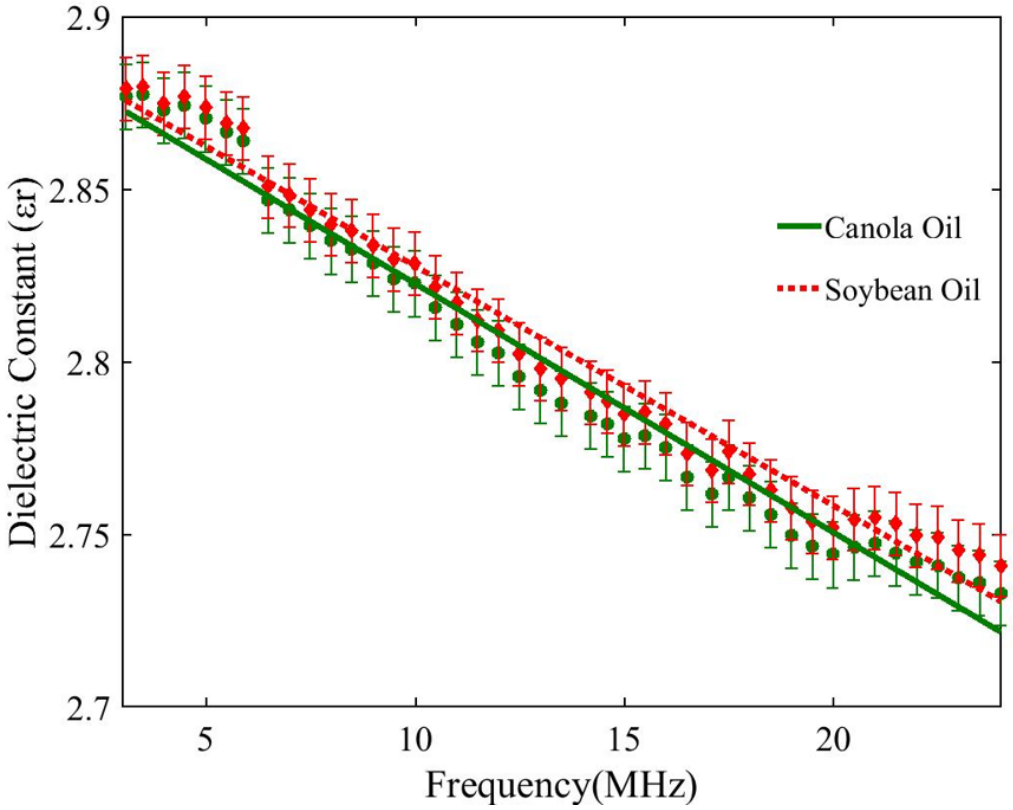

Figure 2.10: Measured dielectric constants for canola and soybean oil.

of 10%, 30%, 40%, 50%, 60%, 65% and 80% glycerine. The liquid sample under test is filled up to the top of the dielectric spacer filling the gap in both the designs. Depending on the change in properties of the liquid, both the electrical and mechanical resonances shift and this is monitored wirelessly using an impedance analyzer. Figure 2.12 shows the change in electrical resonance for different concentrations of glycerine-DI water solutions for Sensor-1 and Figure 2.13 for Sensor-2.

The experiments were performed for each liquid sample with a fixed volume of 11 ml for each trial. The values at each frequency point were averaged 32 times by the impedance analyzer during each trial before being recorded. The electrical resonance frequency is inversely proportional to the dielectric constant, or the capacitance, of the sensor. As the dielectric

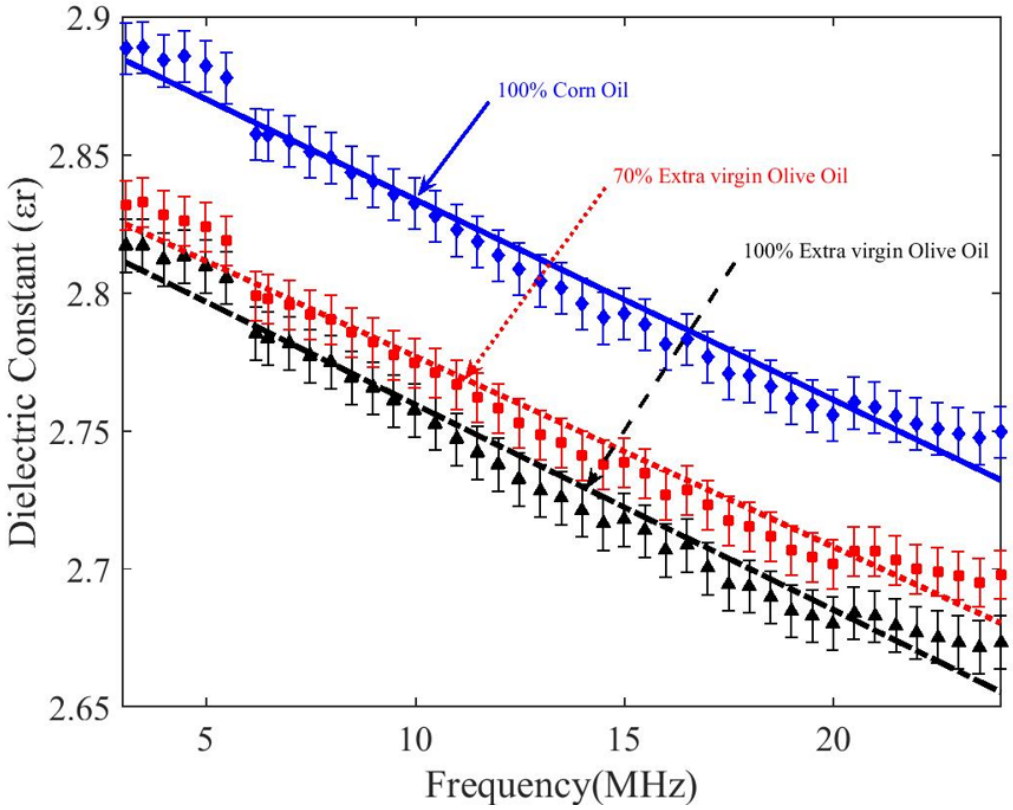

Figure 2.11: Measured dielectric constants for different mixtures.

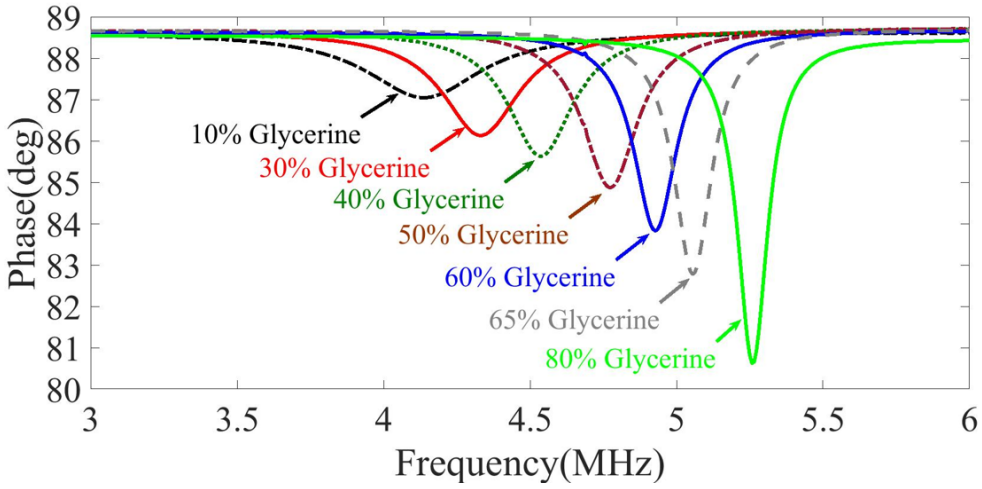

Figure 2.12: Electrical resonance for different concentrations of glycerine-DI water solutions measured using Sensor-1.

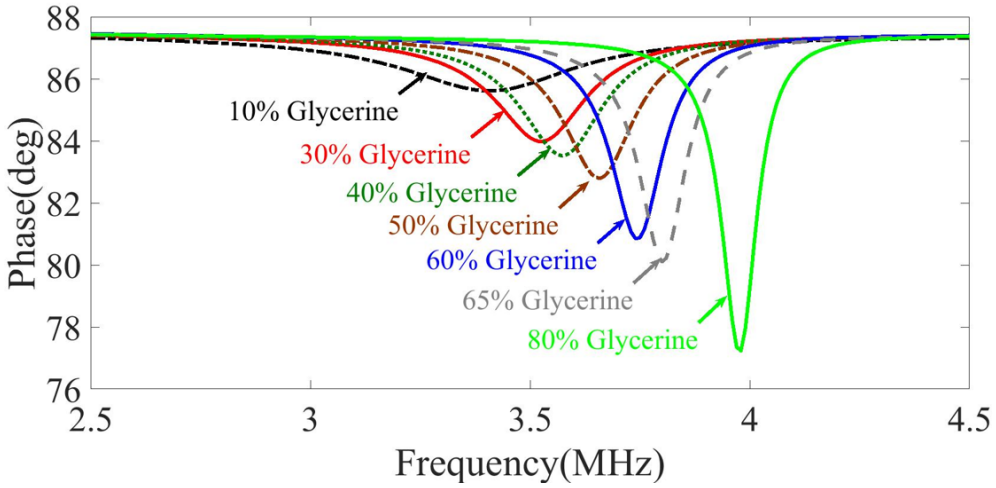

Figure 2.13: Electrical resonance for different concentrations of glycerine-DI water solutions measured using Sensor-2.

constant increases, the resonance frequency decreases and the frequency peak shifts to the left. This demonstrates the dielectric sensing capability of the developed smart vial hybrid sensor. The sensors are evaluated for their performance twice and the results are averaged to compare their performance. Figure 2.14 shows the graph for delta change in frequency versus dielectric constant ($\epsilon_r = 53 - 79$) with respect to 10% glycerine-DI water for both Sensor-1 and Sensor-2.

The resonance peak of the magnetoelastic sensor is traced for different viscosity loading for the same samples simultaneously and the impedance analyzer performs similar averaging before being recorded. The viscosity value for different mixture of water and glycerine can be found in [41]. The viscosity increases with increase in concentration of glycerine as viscosity of 100% glycerine is 1499 cP [41]. Figure 2.15 shows the change in mechanical resonance frequency while using the resonance peak at 10% glycerine- DI water as reference for both Sensor-1 and -2 (viscosity 1-60 cP). The mechanical resonance is directly proportional to the square root of the liquid viscosity and hence an increase in viscosity increases the resonance

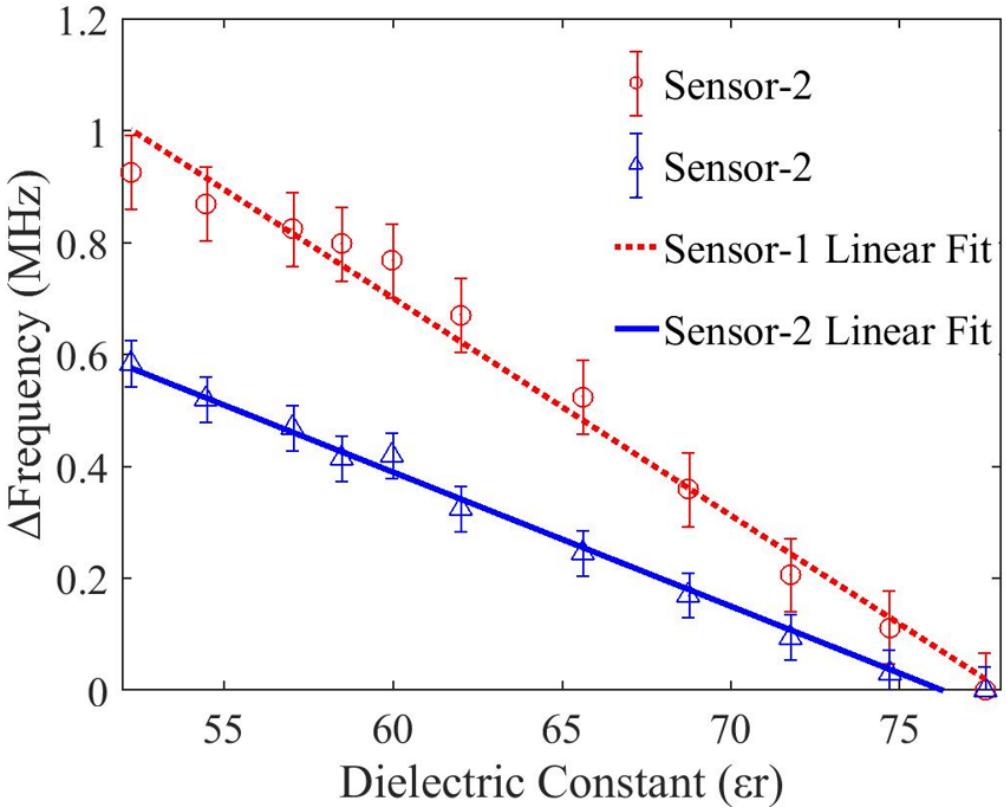

Figure 2.14: Measured change in resonance frequency (electrical) as a function of dielectric constant for Sensor-1 and Sensor-2.

frequency [44]. This demonstrates the simultaneous viscosity (mechanical) sensing capability of the developed smart vial hybrid sensor. The measured results followed a square law dependence of mechanical resonance on viscosity as expected.

2.4.3 Olive Oil Adulteration Detection

Quality control and supply chain management is very important to maintain high standards of food safety and consumer health. The magnetoelastic sensor has been used for quality control of liquid food such as glucose, oil, and milk [45]. In this paper, an application of the hybrid sensor is demonstrated for olive oil (extra virgin) adulteration detection. The corn

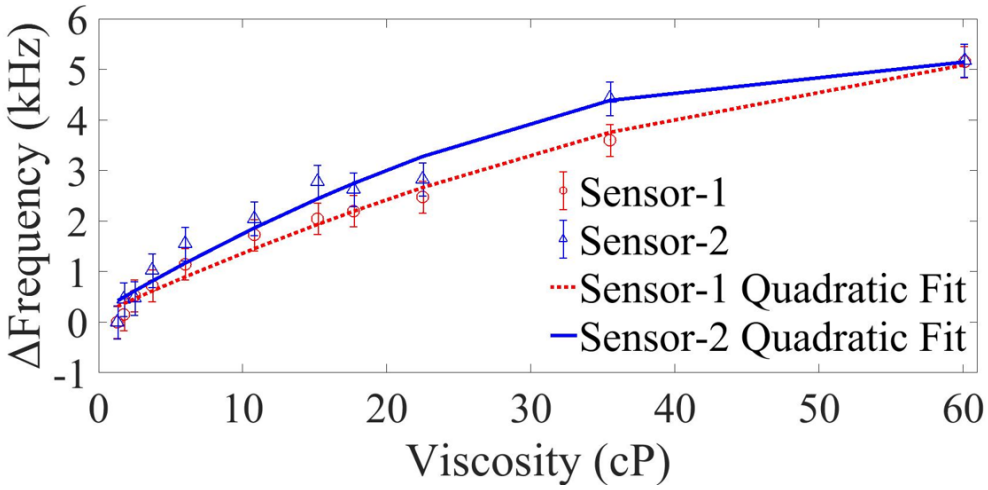

Figure 2.15: Measured change in resonant frequency (mechanical) as a function of viscosity (cP) for Sensor-1 and Sensor-2.

oil and olive oil were mixed in different ratios for testing the sensitivity of the sensor. It is almost impossible to detect the mixing by just a visual inspection.Figure 2.16 and Figure 2.17 show the change in electrical resonance for adulteration levels of olive oil for Sensor-1 and Sensor-2.

In all the measurements, the volume of the samples used for testing was fixed to be 11 ml. The olive oil and the corn oil has a measured dielectric constant of approximately 2.74 and 2.82, respectively, at 11.5 MHz. From the results shown in Figure 2.11, it is evident that the dielectric constant varies depending on the level of adulteration. The trend shows a downward shift in resonant frequency for an increase in dielectric constant as expected. Figure 2.18 shows the change in frequency (electrical) for different adulteration levels with 100% olive oil as reference. The slope of the graph indicates that Sensor-1 has a similar sensitivity as Sensor-2 for detecting small changes in dielectric constant.

Figure 2.19 shows the change in frequency (mechanical) for the adulteration level with 100% olive oil as the reference. The adulteration changes the viscosity of the oil. Olive oil

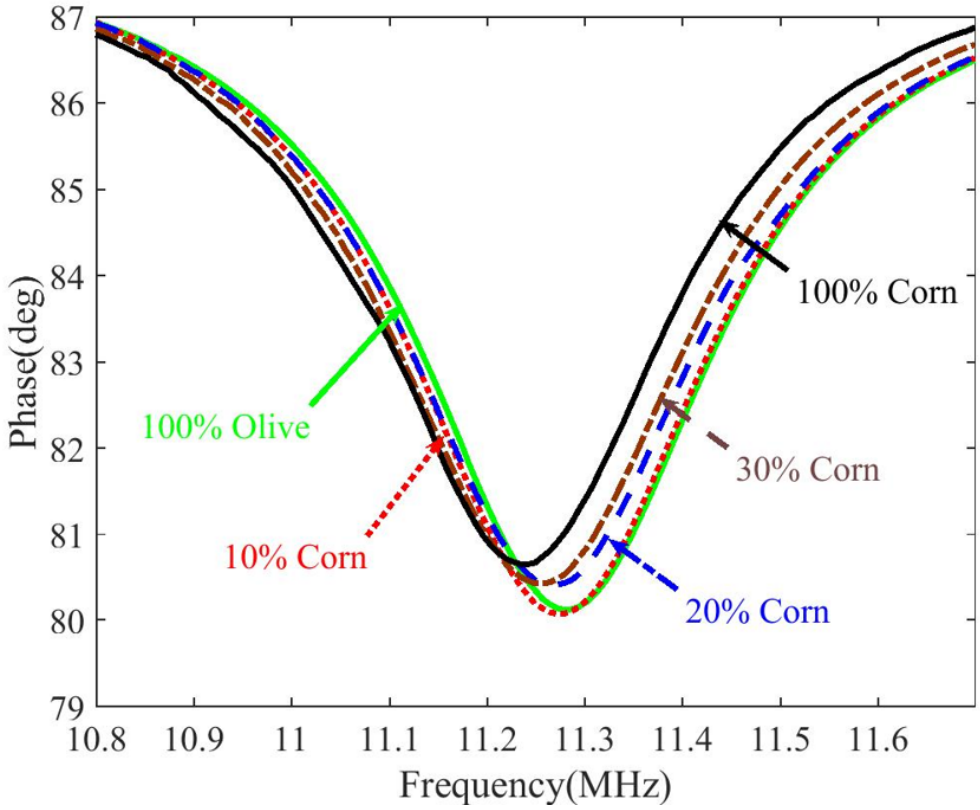

Figure 2.16: Electrical resonance for different concentrations of olive oil and corn oil mixtures for Sensor-1.

has viscosity of 92 cP [46] and corn oil 52.3 cP [47]. It can be inferred from the graph that two magnetoelastic strips in parallel (Sensor-2) has higher sensitivity to change in viscosity than one magnetoelastic strip (Sensor-1) as expected.

Overall, Sensor-2 which has two magnetoelastic strips (Sensor-2) in parallel offers a much simpler design with similar sensitivity for a dielectric constant change and a higher sensitivity for a viscosity change than Sensor-1 for adulteration detection of extra virgin olive oil. The natural resonance of the sensor can be tailored to RFID frequency by appropriately choosing the geometry of the metglas. Likewise, the electrical resonance can also be tuned to be compatible with RFID frequency making it easily adaptable to the existing RFID

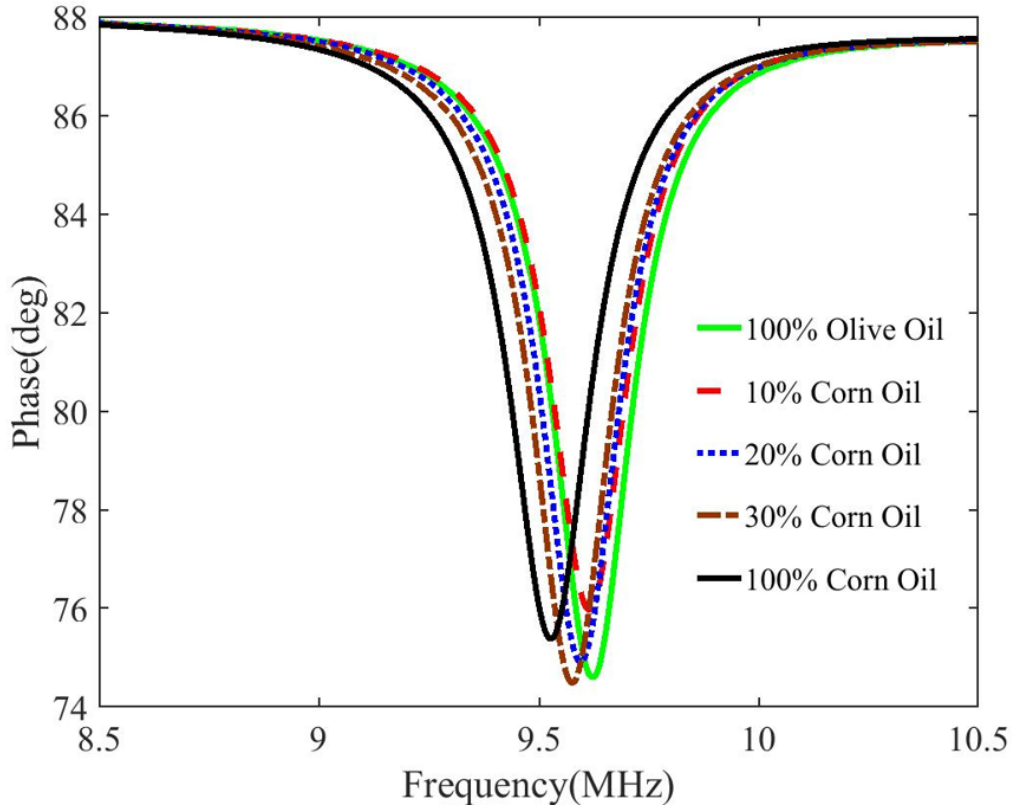

Figure 2.17: Electrical resonance for different concentrations of olive oil and corn oil mixtures for Sensor-2.

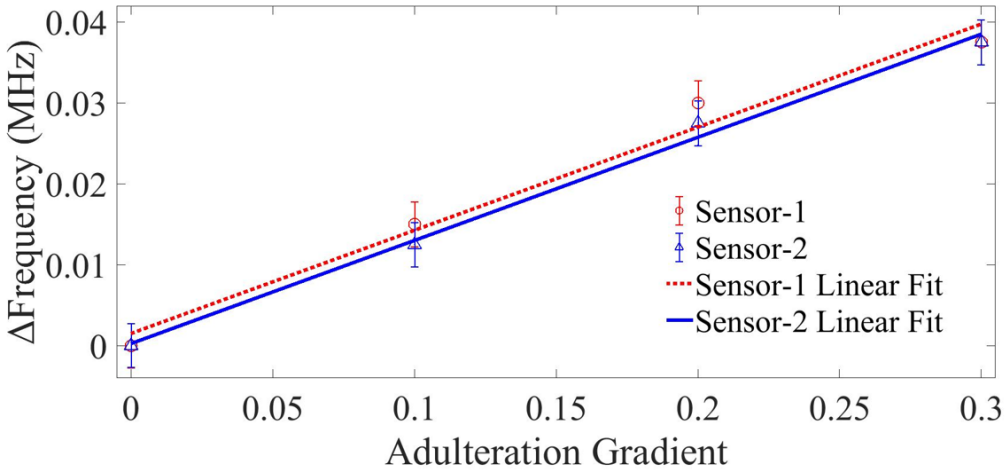

Figure 2.18: Change in frequency (electrical) as a function of adulteration concentration for Sensor-1 and Sensor-2.

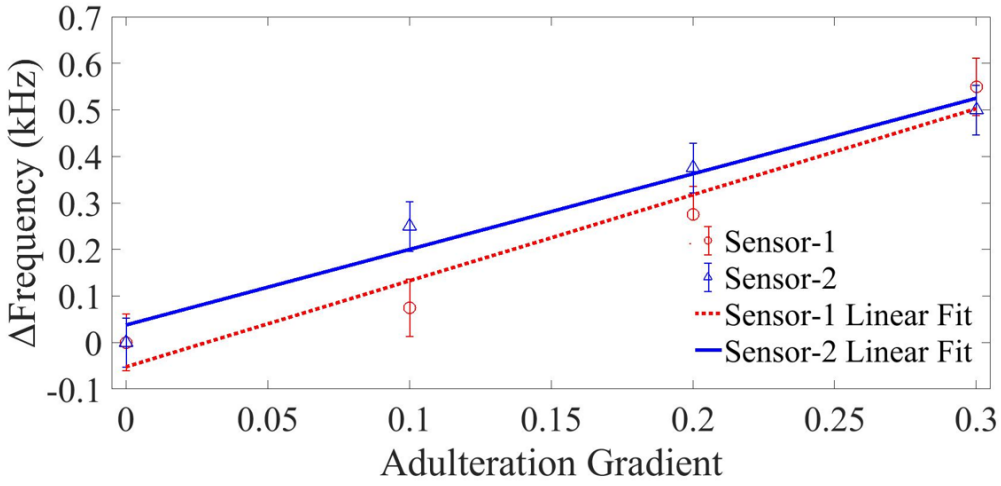

Figure 2.19: Change in frequency (mechanical) as a function of adulteration concentration for Sensor-1 and Sensor-2.

infrastructure.

2.5 Summary

This chapter demonstrates a simple, inexpensive, and reusable hybrid sensor for real time liquid sample measurements. It has many applications and in this chpater, it has been demonstrated for the adulteration detection of extra virgin olive oil. The hybrid sensor can play a key role in food safety and quality management. The hybrid nature of the sensor allows simultaneous measurement of two properties, dielectric constant and viscosity, by tracking the electrical and mechanical resonant frequencies. The resonance frequencies are measured wirelessly enabling remote detection. The natural resonance of the sensor can be tailored to be compatible with RFID readers making it easily adaptable to the existing RFID infrastructure. The hybrid sensor has several advantages over single parameter sensors such as being real time, simple to use, and wireless. One limitation is that the sensor is invasive in nature and hence requires the samples to be in direct contact with the sensing element. The

detection of 10% adulteration by the smart vial is low enough for most practical applications and this sensor can be readily used for quantification of commercial extra virgin olive oil along the supply chain.

Chapter 3

Dielectric Based Microfluidic Sensors For Quality Control

3.1 Introduction

The second topic investigated is to develop low cost microfluidic based sensors for dielectric profiling. Typically, RF sensors are placed on the outer wall of the food packaging for detecting the food quality. Resonators are commonly used RF sensors for determining the dielectric constant of food similar to the one demonstrated in the previous chapter. The microfludic channel can be easily made as part of the substrate on which the resonator is fabricated. The target liquid entering the channel perturb the fields of the resonator and this in turn shifts the resonance frequency. The resonance frequency is correlated to the dielectric constant of the target liquid and is monitored for identification. Typically, liquid food packages are fabricated using plastics and this is a boon for alternative low cost manufacturing techniques such as 3D printing. By employing 3D printing, the food package can be printed along with the sensor and the microfluidic channel as envisioned in Figure 3.1.

In this chapter, 3D printing has been employed as an alternative low cost fabrication technique than traditional manufacturing to fabricate the sensors. First, a 3D printed perturbed cavity resonator followed by a metamaterial-inspired split ring resonator is presented for dielectric profiling of liquids. Second, a wireless passive 3D printed RFID tag is pre-

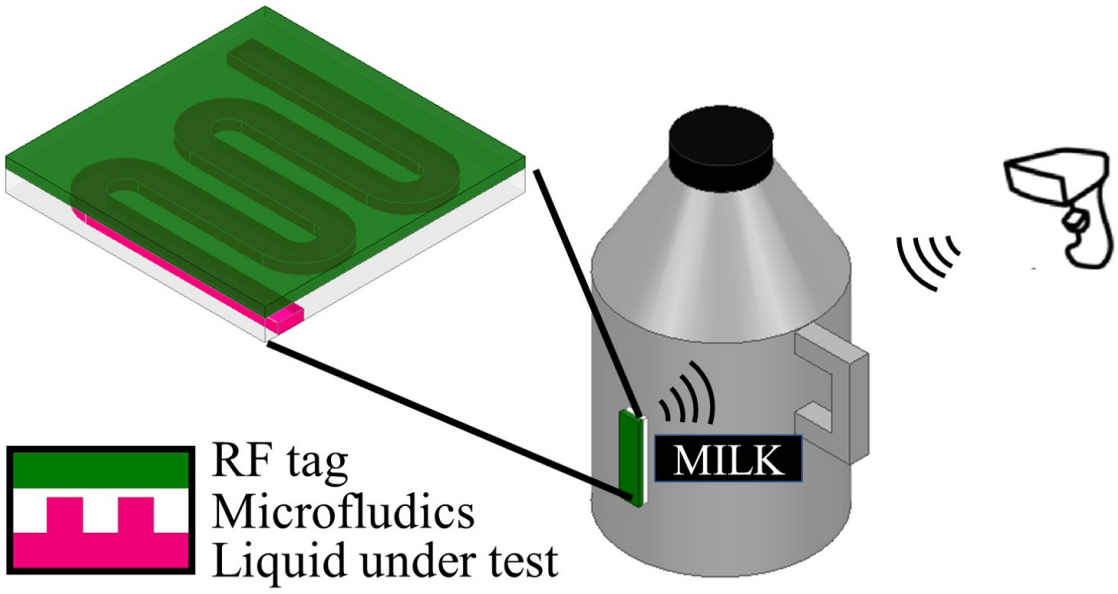

Figure 3.1: Envisioned "smart" packages with 3D printed microfluidics and food packages for quality monitoring.

sented and performance compared to a traditional RFID tag showing a technique to utilize 3D printing for fabricating customized and low cost sensors for monitoring products along the supply chain.

Recently, 3D printing has garnered significant attention in fabrication of RF and microwave devices due to their significant advantages than traditional manufacturing techniques such as lower fabrication cost, rapid customization, flexibility in the third dimension (z-axis), and can fabricate complex geometries with ease. Some examples of 3D printed microwave devices presented in literature are antennas, resonators, and microstrip-based circuits [48–50].

3.2 3D Printed Cavity

Cavity perturbation is one the most widely used technique for characterizing materials due to its relative simplicity in obtaining the intrinsic properties of material under test. From the time Bethe and Schwinger proposed the cavity perturbation technique, multiple studies have been published modifying the classical perturbation theory for different practical applications [51]. These techniques have been typically demonstrated by inserting a small sample into the cavity or by creating a small deformation along the cavity walls to insert the sample. An extensive review on the origin of cavity perturbations and the development of different methods of perturbations is presented in [52, 53].

Furthermore, modifications of cavity resonators coupled with different guided wave structures and resonators have been reported in literature for determining the dielectric properties of liquids such as cavity coupled substrate integrated waveguides (CSIW) [54], fringing field based perturbed cavity resonator [55], coaxial coupled cylindrical open-ended cavity resonator [56], whispering-gallery based semi-open metal shield cavity resonator [57], and split ball resonator coupled perturbed cavity resonator [58]. Table 3.1 lists the different perturbation techniques along with the sensing principle that has been reported in literature in the last five years for liquid characterization. The modified cavities have enhanced sensitivity but has complex geometry that is difficult to fabricate using traditional manufacturing techniques.

Typically, cavity resonators are fabricated using traditional techniques such as micromachining, metal plate soldering, dip brazing, and electric discharge machining. These techniques are complex and labor intensive, and consumes more material and generates large wastes. Moreover, metal machining increases the weight of the cavity and, in the case

Table 3.1: Different cavity perturbation techniques for liquid sensing

Circuit	**Perturbation**	**Sample**	**Reference**
Cavity Coupled substrate integrated waveguide	Cylindrical Rectangular Slotted	Solvents, Glycerine Water, Solvents	[54], [59] [60]
Rectangular Cavity	Cylindrical Fringing Fields	Solvents, Water Oil	[61] [55]
Rectangular Coupled Cavity	Cylindrical	Solvents	[58]

of multiple layers, can lead to misalignment errors between parts. An alternate fabrication technique that is simple low-cost and can readily prototype complex geometries from a range of materials overcoming the limitations of conventional fabrication is 3D printing. A number of microwave circuits such as antennas, resonators, and waveguides, have been fabricated and demonstrated using 3D printing [62, 63]. 3D printing is ideal for fabricating low-loss air substrates (ϵ_r =1) due to the flexibility in the third dimension and has been demonstrated for fabricating different microwave devices, e.g., multi-layered cavity resonator [64–66]. Leveraging on the advances in AM, a low-cost reusable resonator sensor for characterizing small sample of liquids is presented.

A rectangular cavity resonator is 3D printed using VeroWhitePlus polymer material and is metal coated using metal sputtering followed by electroplating. A small cylindrical perturbation (sample holder) is created in the top layer of the cavity in which the liquid samples are loaded. Based on the sample loading, the resonance frequency of the cavity changes and it is monitored in real-time for sample characterization. A variety of standard dielectric liquid samples were measured and characterized demonstrating the sensitivity of the fabricated resonator and its potential use in monitoring liquids along the supply chain.

3.2.1 Theory

Material perturbation of resonance cavity is a well established theory [67]. When a cavity is perturbed with a material of different relative permittivity ϵ_r and permeability μ_r, the resonance frequency of the cavity shifts by $\Delta\omega$ as given in 3.1, where ω_0 represents the resonance frequency of the air filled cavity. In 3.1, $\vec{E_0}$ and $\vec{H_0}$ represent the original electric and magnetic fields and V_0represents the perturbed volume.

$$\frac{\Delta\omega}{\omega_0} \simeq -\frac{\int_V \left((\epsilon_r - 1)\epsilon_0|\vec{E_0}|^2 + (\mu_r - 1)\mu_0|\vec{H_0}|^2\right)dv}{\int_V \left(\epsilon_0|\vec{E_0}|^2 + \mu_0|\vec{H_0}|^2\right)dv} \tag{3.1}$$

For a pure nonmagnetic dielectric material, 3.1 is reduced to simplified 3.2.

$$\frac{\Delta\omega}{\omega_0} \simeq -\frac{\int_V \left((\epsilon_r - 1)\epsilon_0|\vec{E_0}|^2\right)dv}{\int_V \left(\epsilon_0|\vec{E_0}|^2\right)dv} \tag{3.2}$$

Equation 3.2 denotes that the fractional change in stored electric field due to a dielectric material perturbation can be related to fractional change in the resonance frequency. The rectangular cavity was designed with a=50 mm, d=50 mm and b=14 mm, which would excite the TE_{101} mode at ω_0=4.24 GHz for unperturbed air medium. The resonance frequency ω_0 can be calculated as in 3.3.

$$f_{mnl} = \frac{c}{2\pi\epsilon_r\mu_r}\sqrt{\left(\frac{m\pi}{a}\right)^2 + \left(\frac{n\pi}{b}\right)^2 + \left(\frac{l\pi}{d}\right)^2} \tag{3.3}$$

$$E_y = Asin\left(\frac{\pi x}{a}\right)sin\left(\frac{\pi z}{d}\right) \tag{3.4}$$

For unperturbed TE_{101} mode, electric field E_y can be shown as given in 3.4. Now, when the electric field is perturbed due to a specific material, the fractional change in resonance

frequency is quantified by computing the numerator integral as in 3.2. When different materials would be introduced in the cavity, the total energy of the unperturbed cavity, which is the denominator of 3.2 would remain constant for all of them except the numerator would be changing for different cases. The integral in 3.2 can be computed by substituting E_y from 3.4.

Considering a dielectric material perturbation of dimensions a_0, b_0, c_0 of rectangular shape positioned with center at x_0, y_0, z_0), the integral in 3.2 is computed as shown in 3.5

$$\int_V \big((\epsilon_r - 1)\epsilon_0 |\vec{E_0}|^2\big) dv = A^2(\epsilon_r - 1)\epsilon_0 b_0 \int_{x_0 - \frac{a_0}{2}}^{x_0 + \frac{a_0}{2}} sin^2\big(\frac{\pi x}{a}\big) dx \int_{z_0 - \frac{c_0}{2}}^{z_0 + \frac{c_0}{2}} sin^2\big(\frac{\pi z}{d}\big) dy \tag{3.5}$$

$$\int_V \big((\epsilon_r - 1)\epsilon_0 |\vec{E_0}|^2\big) dv = A^2(\epsilon_r - 1)\epsilon_0 b_0 \Big(\frac{a_0}{2} - \frac{a}{\pi} cos\Big(\frac{2\pi x_0}{a}\Big) sin\Big(\frac{\pi a_0}{a}\Big)\Big) \Big(\frac{c_0}{2} - \frac{d}{\pi} cos\Big(\frac{2\pi z_0}{d}\Big) sin\Big(\frac{\pi c_0}{d}\Big)\Big) \tag{3.6}$$

$$\frac{\Delta\omega}{\omega_0} = \frac{2k_0 k_a k_d b_0 (\epsilon_r - 1)}{bd}$$

where

$$k_a = \Big(\frac{a_0}{2} - \frac{a}{\pi} cos\Big(\frac{2\pi x_0}{a}\Big) sin\Big(\frac{\pi a_0}{a}\Big)\Big)$$
$$k_d = \Big(\frac{c_0}{2} - \frac{d}{\pi} cos\Big(\frac{2\pi z_0}{d}\Big) sin\Big(\frac{\pi c_0}{d}\Big)\Big) \tag{3.7}$$

The fractional change in resonance frequency is quantified as shown in 3.7. Here, constant k_0 is experimentally obtained, which denotes the coupling of the dielectric material through some the 3D printed material. Finally, the relative dielectric constant of the material under test is obtained from the fractional resonance frequency change as shown in 3.8.

$$\epsilon_r = 1 + \frac{\Delta\omega}{\omega_0}\frac{bd}{2k_0k_ak_db_0} \tag{3.8}$$

Here, constant k_o is experimentally obtained, which denotes the coupling of the dielectric material through the 3D printed material.

3.2.2 Simulation and Fabrication

The dimensions of the cavity were chosen to be 50*50*14 mm such that the resonance frequency of the air-loaded cavity is at 4.17 GHz. The most important step to realize good sensitivity is to optimize the shape and location of the perturbation in the top wall of the cavity. Initial simulations were performed to analyze the sensitivity of various perturbation positions and an optimal position was chosen for the design. For all the simulations, the size and shape of the perturbation is fixed. The cylindrical perturbation chosen has a radius of 5 mm and a depth of 4.5 mm leading to a total volume of 0.35 cm^3. Two different samples were loaded into the perturbation, air and liquid (ϵ_r=25) and the simulations were performed at various perturbation positions. The sensitivity is obtained by calculating the difference in the resonance frequency between air and liquid loading and is expressed as Δf . The center of the top layer of the cavity is at (25, 25, 14) and the center of the cylindrical perturbation is at (x, y, 14). A predefined combination of (x, y) coordinates for the center of the cylindrical perturbation is chosen. Figure 3.2 shows the sensitivity for different sample holder positions along the top wall of the cavity.

It can be inferred from Figure 3.2 that sensitivity of the sensor is high at the center of the cavity, as expected. In order to cater to a wide variety of liquids with higher loss tangent, the center is not an ideal choice since strong coupling of a lossy liquid impacts the

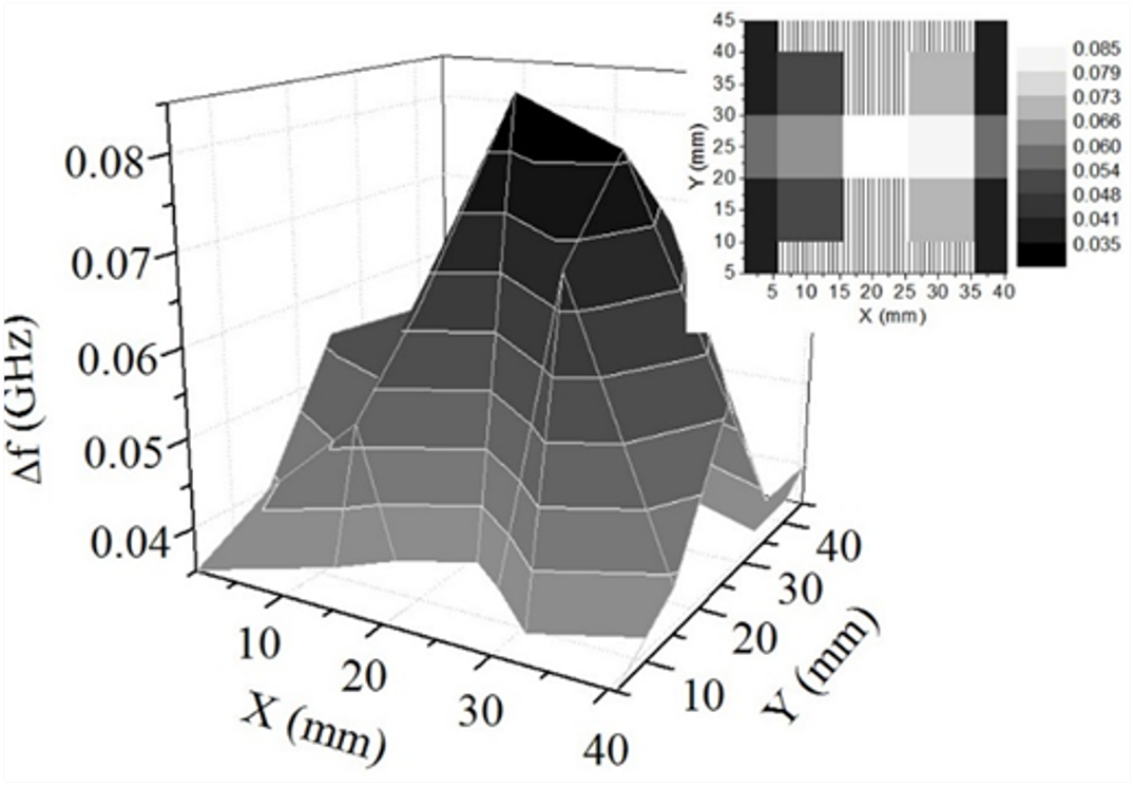

Figure 3.2: Sensitivity of the sensor for different perturbation positions.

Q-factor of the sensor. Hence, (10, 25, 14) was chosen as an optimal position for the center of the cylindrical perturbation. The schematic of the designed 3D printed rectangular cavity resonator, the fabricated image along with its dimensions are shown in Figure 3.3.

A rectangular cavity was 3D printed using Stratasys Object Connex350 printer in two separate pieces as shown in Figure 3.3. After metallization, these are snapped together using LEGO-like support pillars and corresponding holes as discussed in [64]. The metallization of the printed parts is a two-step process; first, 60 nm titanium is sputter deposited for adhesion of copper onto the plastic followed by 500 nm of copper. In the second step, the thickness of the metal layer is increased to 5-6 μm by electroplating copper. The patterning of the metal layers on the 3D printed plastic is done using a damascene-like mechanical polishing process presented in [68].The cavity is excited by 50 Ω microstrip lines extended on either side on

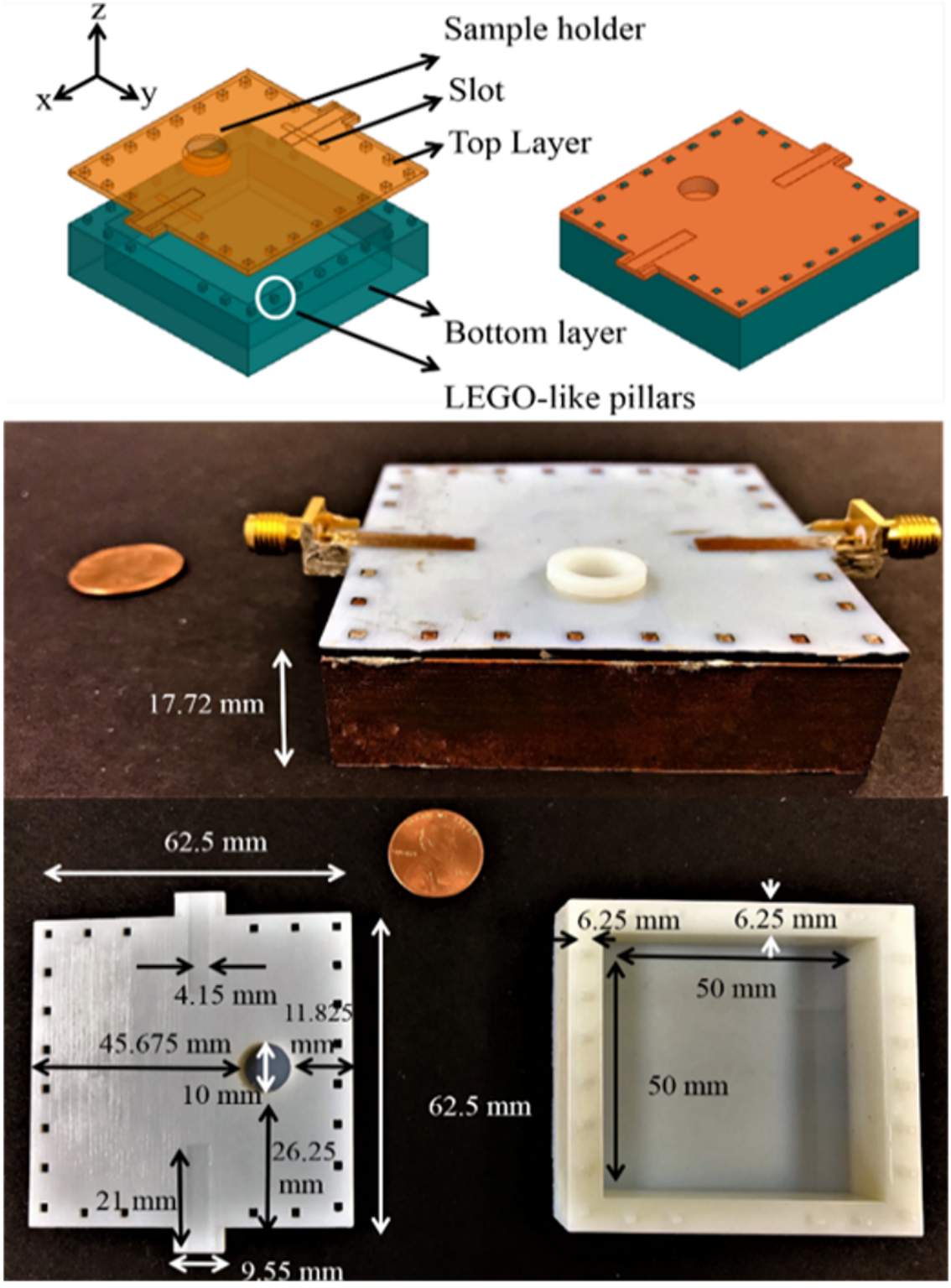

Figure 3.3: Schematic and image of the 3D printed rectangular cavity with dimensions.

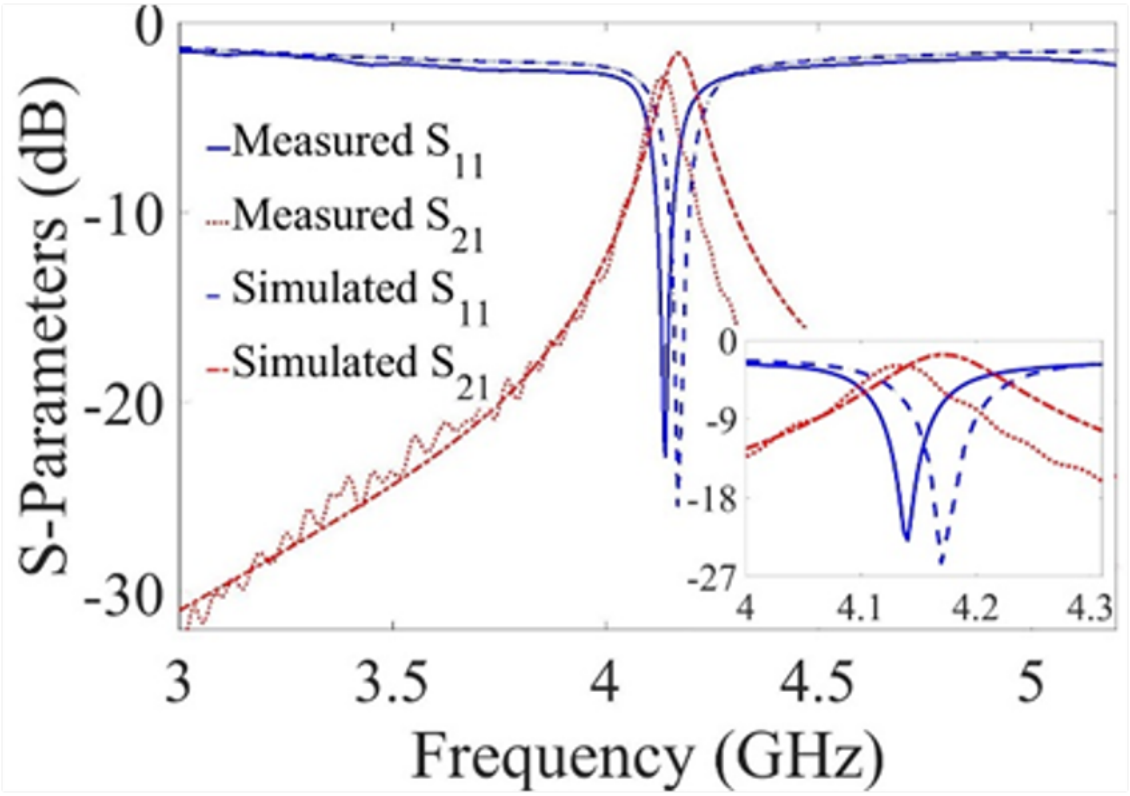

Figure 3.4: Simulated and measured s-parameters of the 3D printed perturbed cavity resonator.

the top layer and SMA connectors are attached, using conductive silver paste (resistivity 0.017 Ω.cm), for probing. Two rectangular slots (2 mm * 15 mm) are cut in the seed metal layer below the microstrip lines for coupling into the cavity. Figure 3.4 shows the simulated and measured results for the designed resonator. The measured and simulated resonance frequencies are at 4.14 GHz and 4.17 GHz, respectively. The downward shift in frequency is due to the lossy conductive silver paste on the connectors that affect the coupling into the cavity as well as reduced air gaps between the top and bottom layer due to warping effects of the VeroWhitePlus material during the sputtering process making the cavity a little larger than the designed dimensions.

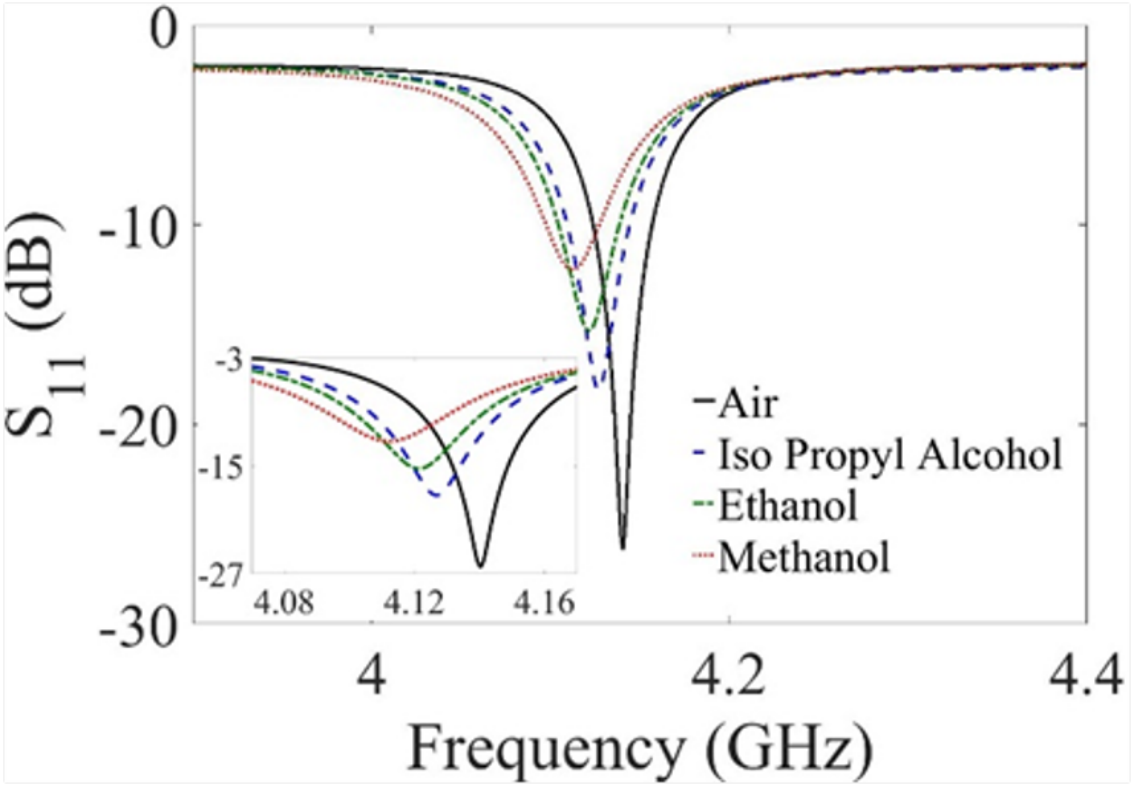

Figure 3.5: Measured frequency shift for different solvent loading.

3.2.3 Results and Discussion

A set of experiments were performed by using the cylindrical perturbation of dimensions 5 mm (radius) * 4.5 mm (depth) positioned with center at $x_0 = 10.575$ mm, and $z_0 = 25$ mm. The equivalent rectangular perturbation dimensions are $a_0 = c_0 = 8.86$ mm, $b_0 = 4.5$ mm. The perturbation was completely filled with the solvent under test (350 μl), and each solvent was measured three times and the results were averaged out. Figure 3.5 shows the measured resonance frequency shift under different solvent loadings.

It can be inferred from Figure 3.5 that as the dielectric constant increases, the resonance frequency decreases, as expected. Using the experimental shift, the value of constant k_0 was estimated as 40.2.Table 3.2 shows the experimentally obtained dielectric constant and the

dielectric constant reported in literature for the different solvents used in the experiment along with the corresponding resonance frequencies.

Table 3.2: Estimated and standard dielectric constants for samples under test and measured resonance frequency.

Solvent	**Estimated** ϵ_r	**Literature** ϵ_r [68]	f_0 **GHz**
Iso Propyl Alcohol	18.88	18.62	4.127
Ethanol	23.99	25.10	4.122
Methanol	36.77	32.35	4.112

The 3D printed multi-use cavity resonator is a low-cost easily customizable choice for monitoring liquid quality in real-time using a small sample volume. This technique is attractive since it can be easily tailored to suit a variety of liquids with varying dielectric properties by optimizing different perturbation parameters such as the size, shape, position, and coupling with the cavity. The sensitivity can be further improved by selecting the choice of the perturbation parameters based on the minimum detectable dielectric change which is required to evaluate the quality of the liquid under test. For example, the sensor can be easily adapted to monitor adulteration of milk with water or between different oil mixtures. Furthermore, 3D printing allows customizable perturbation geometries, allowing to tailor the sensitivity for even a small dielectric property change in liquid sample under test. The 3D printing of microwave devices offers several advantages, such as rapid customization and simple tool setup. But, it also has few associated challenges such as the mounting of SMA connectors to the cavity with the lossy silver epoxy leading to poor quality factor. This can be improved by printing the cavity using a high-temperature resin instead of VeroWhitePlus and soldering the connectors directly onto the metalized plastic. Using a high temperature

material will also prevent warping of the 3D printed substrates during and after the sputtering process. Advances in low loss 3D printed material and printing parts with smoother surface will lead to further improvement in the quality factor of the resonant cavity. The real-time nature of the sensor makes it compatible to monitor liquids along the supply chain. More specifically, in the food supply chain, this technique can be adapted as a quality control measure in estimating the dielectric properties of liquid food and thereby predicting the quality, freshness and spoilage rate over time. The technique is rapid and requires only a small sample volume (350 μl) making it a cost effective solution. The size of the sensor and volume of the sample under test can further be reduced by designing the sensor to operate at a much higher frequency.

3.3 3D Printed Split Ring Resonator

Resonant structures are best suited for liquid characterization due several advantages such as high-quality factor, smaller in size, simple to design, small sample requirement, field-operable, and easier handling. Some examples of resonant structures are perturbation-based cavity resonators, microstrip based resonators, and metamaterial-based or inspired resonators [68, 69]. The fundamental operating principle of these sensors is shift in the resonance frequency based on sample loading and this shift is used to identify and characterize the liquid properties such as dielectric constant of the sample under test. Metamaterials are periodic structures with filtering behavior which are controlled based on the geometry, shape, size, orientation, and the fringing fields. Split ring resonators is the most common topology exploited for realizing metamaterial-based filters or resonators. The rings can be square, circular or triangular with single or multiple gaps based on the application of interest [70].

For liquid sensing, a microfluidic channel is integrated as part of the substrate on which the periodic structure is fabricated. The position, geometry, and shape of the microfluidic channel depends on the fringing fields of the metamaterial-based resonators. A comprehensive review of metamaterial based microfluidic sensors is presented in [71]. Table 3.3 lists the different metamaterial based microfluidic liquid sensors presented in the last five years.

Table 3.3: Different SRR based microfluidic solvent sensors

SRR	**Sample Volume (μL)**	**Reference**
Rectangular Split Ring Resonators	900	[72]
	58.5	[73]
	8.6	**This Work**
	3	[74]
	1.65	[75]

The design chosen for this sensor is a combination of a band-pass and band-stop split ring resonator with integrated microfluidic channel on the substrate. The channel is optimized based on the influence of the sample on the fringing fields of the split ring resonators. Several standard solvents were measured and the frequency shift monitored demonstrating the sensitivity of the fabricated sensor. The fabricated real-time sensor finds its intended use for monitoring the quality of liquids along the supply chain.

3.3.1 Design and Simulation

The dual split ring resonator design consists of a band stop square ring resonator and a band-pass square ring resonator coupled to a 50 Ω microstrip line. The substrate used is a high temperature resin compatible with FormLabs Form2 printer with a dielectric constant (ϵ_r) of 2.8 and a loss tangent (tanδ) of 0.02 [62]. The dimensions are optimized such that the pass band is around 7.5 GHz. The microfluidic channel is positioned such that the liquid

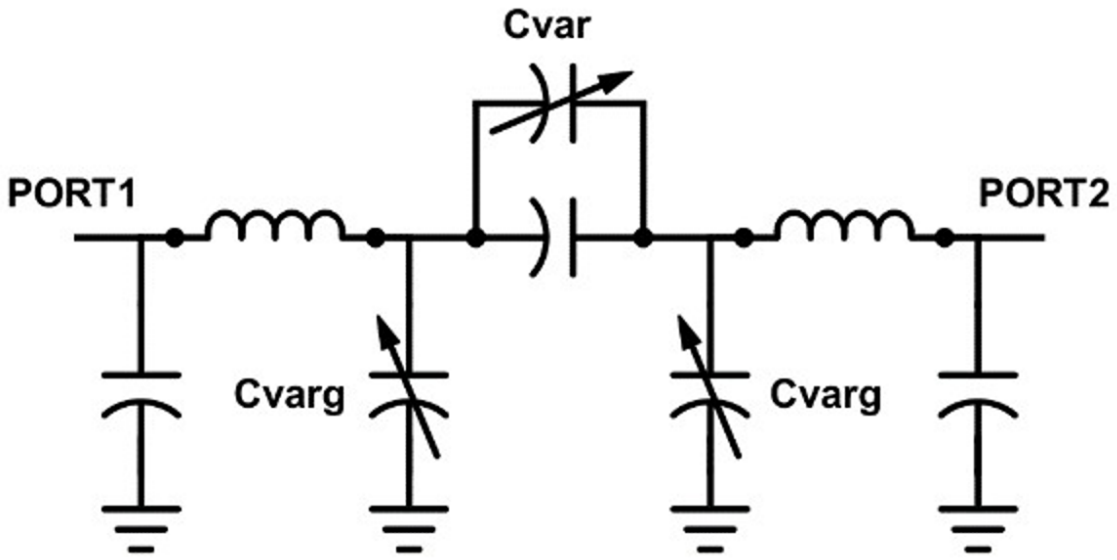

Figure 3.6: Equivalent circuit model at the microfluidic junction.

under test strongly couples to the fringing fields of the resonator. In the proposed design, the gap between the pass band rings is the most sensitive part and hence chosen for the integration of the microfluidic channel (0.5 mm in radius). The equivalent circuit diagram of the band pass rings at the microfluidic junction is shown in Figure 3.6.

The capacitance C_{var} represents the variable capacitance in between the transmission line (gap capacitance), which changes depending on the dielectric constant of the liquid in the microfluidic channel. Furthermore, the transmission line sections also couple to the ground plane through the microfluidic channel. This gives rise to additional capacitance C_{varg}. If the circuit model in between Port 1 and Port 2 is simplified, then C_{eq} represents the equivalent capacitance in between the two ports and L_{eq} represents the equivalent inductance. The resonance frequency (f_{res}) of the resonator is governed by the following 3.9:

$$f_res = \frac{1}{2\pi\sqrt{(L_eqC_eq)}} \tag{3.9}$$

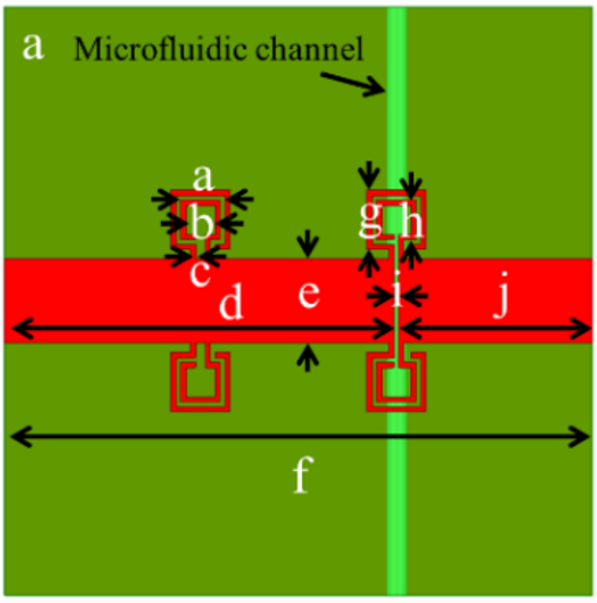

Parameter	Dimension (mm)
a	2.5
b	1.5
c	0.25
d	19.9
e	4.27
f	30
g	3
h	2
i	0.25
j	9.9

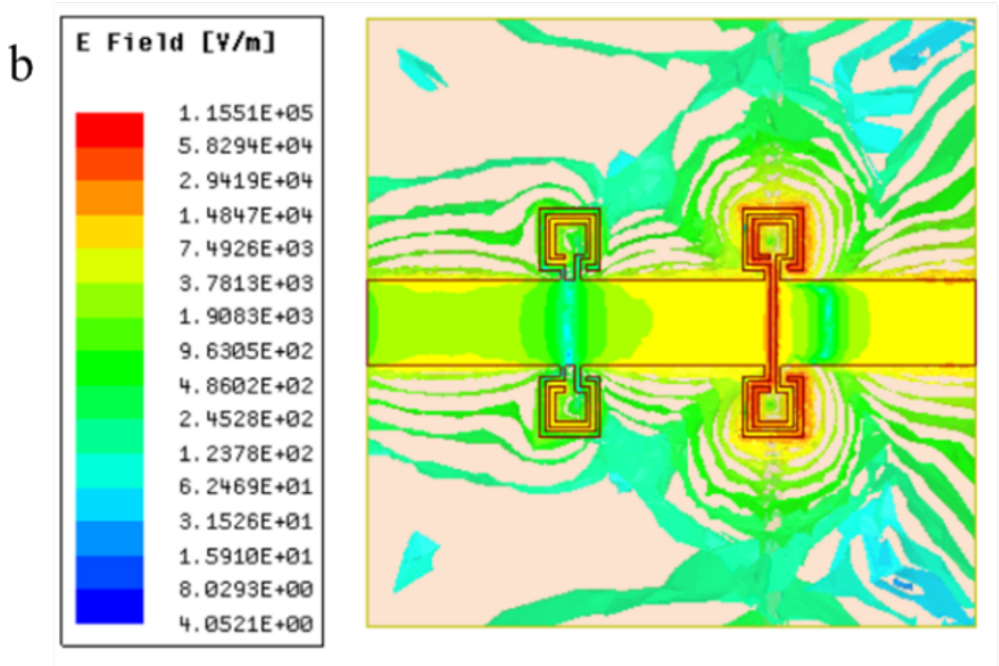

Figure 3.7: Dual SRR a) Schematic with the dimensions, b) unloaded electric field distribution at resonance frequency.

The schematic of the dual SRR integrated with the channel along with the dimensions is shown in Figure 3.7a. Figure 3.7b. shows the unloaded field distribution of the designed sensor at the resonance frequency (7.635 GHz).

3.3.2 Fabrication

The sensor is fabricated using a commercially available Form lab Form 2 printer. A simple metal patterning process is utilized to pattern the conductive traces on the 3D printed substrate [48]. Figure 3.8 shows the four steps involved in patterning conductive traces on the 3D printed substrate. First, the substrate is printed with parts that require metal to be present 200 μm lower than the rest of the parts (called trenches) as shown in Figure 3.8a. Second, a 60 nm Titanium (Ti) is sputter deposited to promote adhesion between the Copper (Cu) and the 3D printed substrate as shown in Figure 3.8b. Third, a 500 nm Cu is sputter deposited on top of the Ti and is followed by electroplating that increases the Cu thickness to $\sim$ 5-6 μm as shown in Figure 3.8c. Finally, the fourth step involves removing the Cu and Ti present in the unwanted areas (non-trenched areas) by a simple damascene-like mechanical polishing step to realize the patterned structure as shown in Figure 3.8d.

Figure 3.9 shows the final fabricated structure along with the simulated and measured results. The resonance frequency of the sensor is at 7.451 GHz which is slightly lower than the simulated response.

The discrepancy in the measured and simulated results is due to the surface roughness of the printed substrate ($\sim$ 1 μm). Furthermore, the non-uniformity in the deposited metal layer inside the trenches and the difficulty to completely polish off metal from unwanted areas around the ring. Due to the smaller gap between lines potentially add extra capacitance to the circuit lowering the resonance frequency.

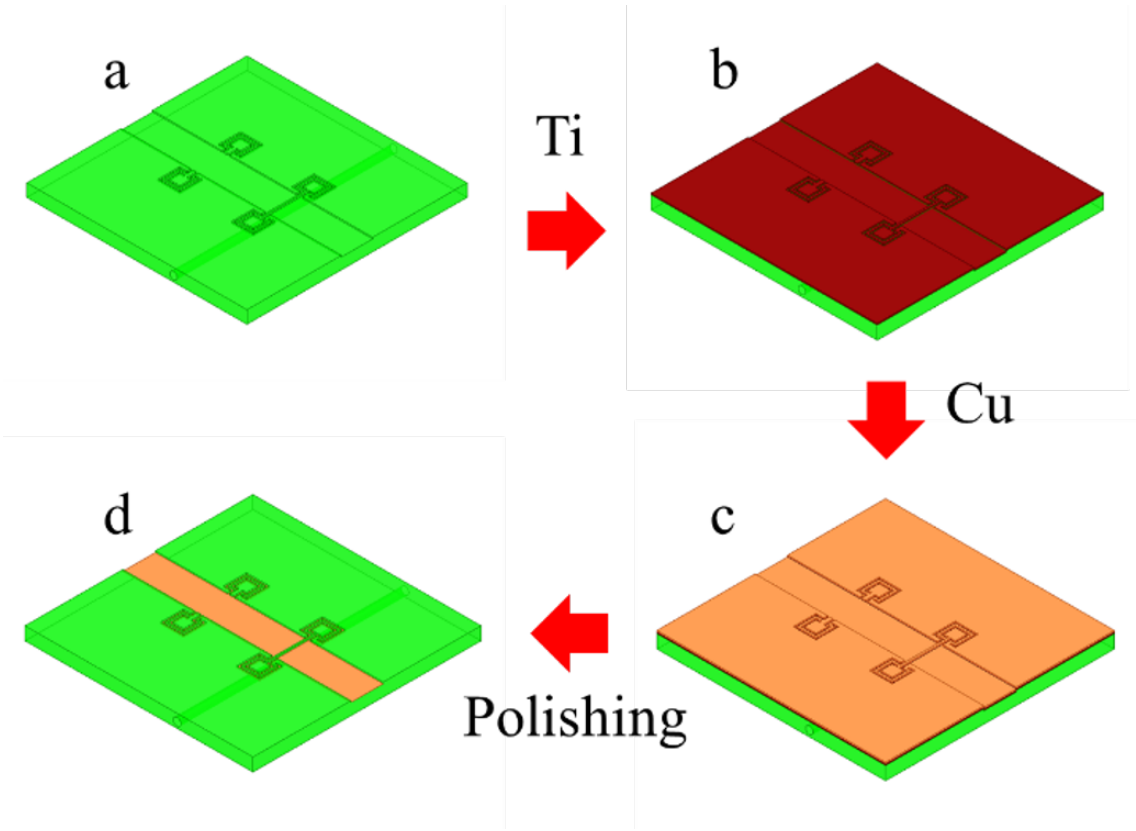

Figure 3.8: Damascene-like metal patterning process a) substrate with different heights (trenches), b) Ti deposition by sputtering, c) Cu deposition by sputtering and electroplating, and d) final polished design.

3.3.3 Results and Discussion

The inlet and outlet of the microfluidic channel is fitted with two needles to facilitate easier introduction of different liquid samples. The sensor is measured using a two port Vector Network Analyzer (Agilent PNA N5227A). A set of experiments are performed to validate the sensitivity of the fabricated sensor. In this experiment, different liquids such as isopropanol, ethanol, methanol, and DI water are injected into the microfluidic channel and the frequency shift is monitored. The experiment is repeated thrice and the values are averaged out. Figure 3.10 shows the change in reflection coefficient for different dielectric loading.

It can be inferred from Figure 3.10 that the resonance frequency of the sensor decreases

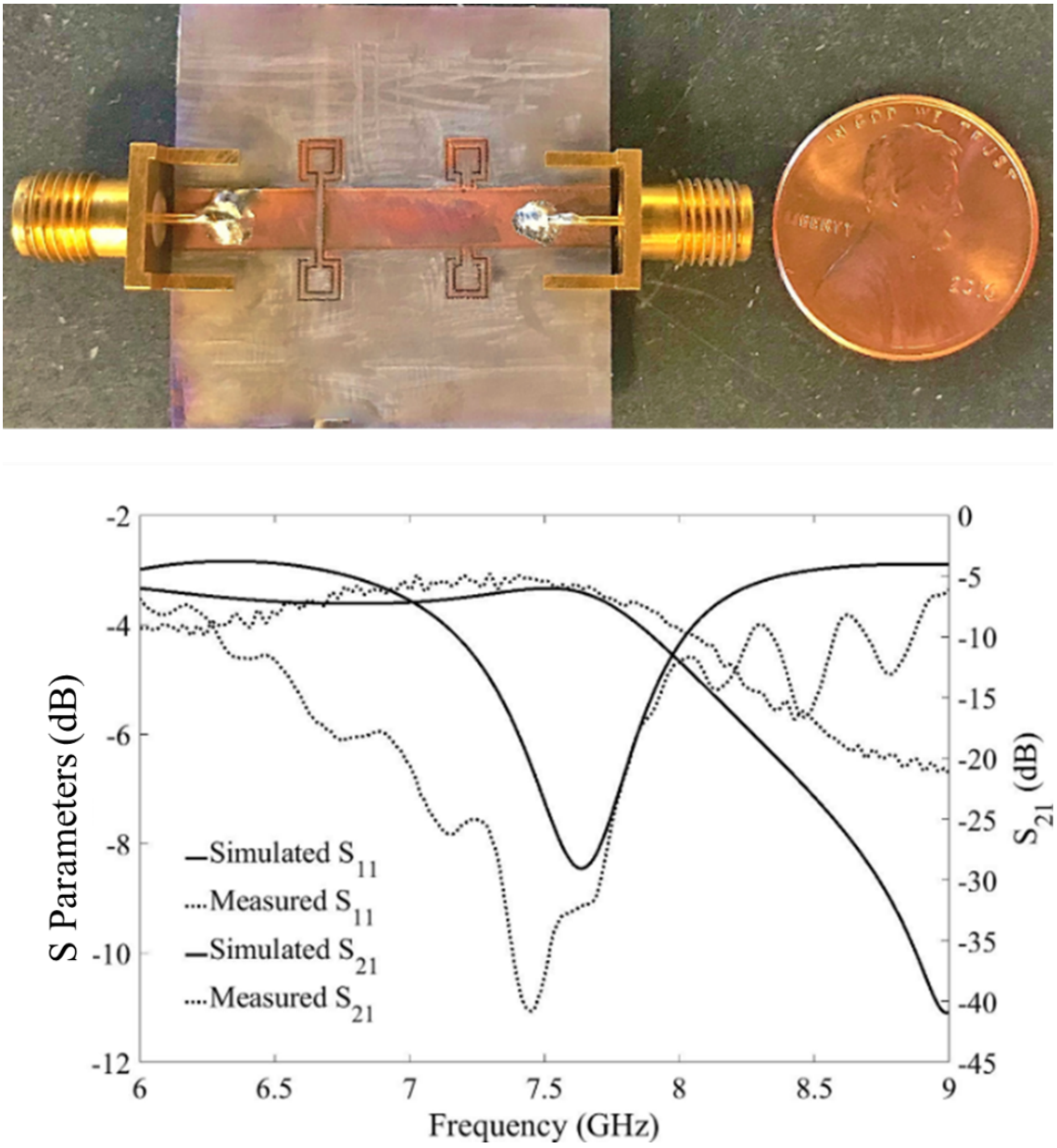

Figure 3.9: Image of the fabricated sensor tag (top), simulated and measured results for the unloaded tag (bottom).

with increase in dielectric constant as expected. The sensitivity depends on the coupling of the samples under test with that of the sensor. In this case, the design was chosen to be strongly coupled and hence more suited for liquids with lower dielectric constants. Nevertheless, the sensor can detect distinctly between isopropanol and ethanol which has

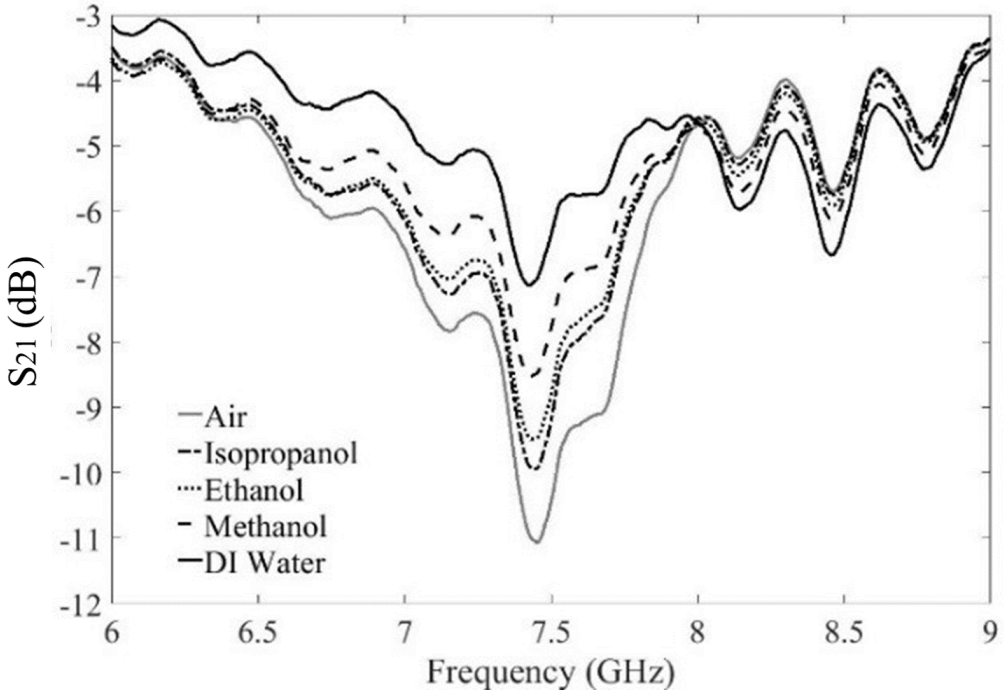

Figure 3.10: Change in transmission coefficient for liquids with different dielectric constants.

a dielectric constant of 18 and 25, respectively [68]. The sensitivity of the sensor can be improved by weakly coupling the microfluidic to the fringing fields for detecting higher dielectric constant mixtures such as isopropanol and water.

The 3D printed metamaterial-based sensor is a low-cost sensor for monitoring liquids in real-time along the supply chain. It can be easily customized and modified to suit the type of liquids being monitored based on optimizing the coupling between the sample and the fringing fields of the sensor. The reusable nature of the sensor allows monitoring multiple liquids in a short period of time. For example, the sensor can be used for detecting adulteration of milk with water along the diary supply chain. The technique is real-time and requires ¡ 10 μl of sample volume making it a cost-effective solution. Furthermore, the sensor can be coupled to an antenna and the data can be transmitted wirelessly making it compatible to any hand-held sensing infrastructure such as RFIDs.

3.4 3D Printed Passive RFID tag

A typical RFID system consists of an RFID interrogator and a RFID tag. The interrogator sends the query signal and the tags within the range of the interrogator receives the query signal and responds back backscattering the identification information. Traditionally, RFID tags are printed using a roll-to-roll technique such as screen printing or inkjet printing in a large scale. The conventional tags are generally attached external to the object to be tracked which are not immune to physical tampering and may in turn encourage counterfeiting. To overcome this limitation, the RFID tags can be made as an integral part of the plastic packaging making it tamper proof discouraging counterfeiting. One technique is to 3D print the RFID tag directly on the food package allowing seamless integration and promotes better authentication controls [76].

3.4.1 Design

3.4.1.1 RFID Tag Design

The FCC approved UHF RFID frequency band is 902-928 MHz and for most practical cases 915 MHz is chosen as an operating frequency for the tag. A meandered dipole antenna design is chosen to reduce the overall form factor of the tag. The antenna is designed to operate at 915 MHz and is impedance matched to a commercial RFID chip (Higgs 3 from Alien Technology) using ANSYS HFSS. The schematic of the designed RFID with the dimensions and the fabricated image is shown in Figure 3.11.

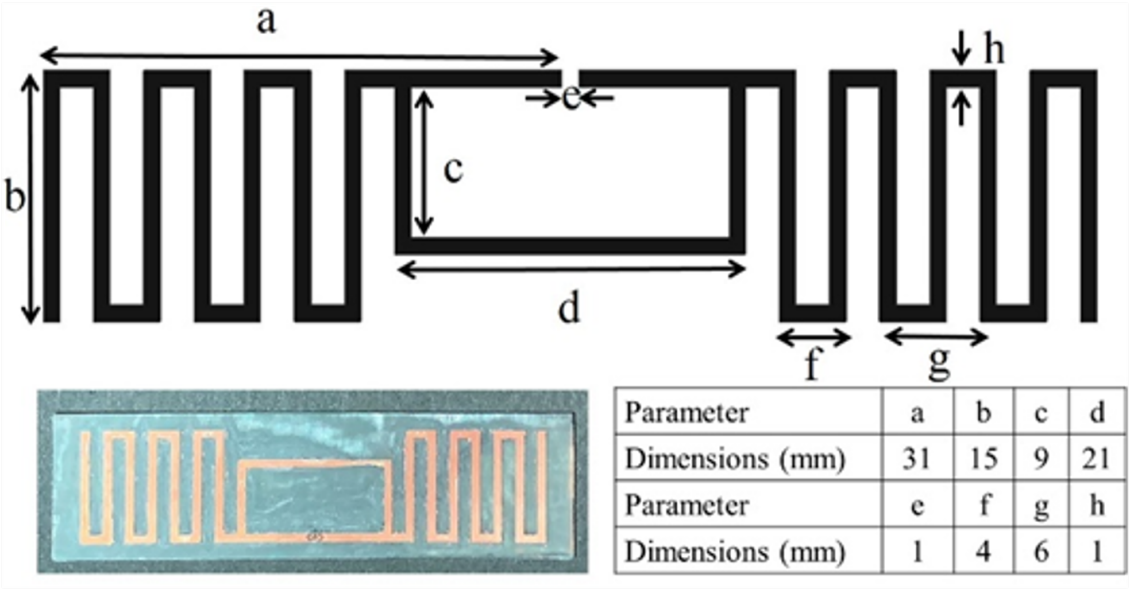

Parameter	a	b	c	d
Dimensions (mm)	31	15	9	21
Parameter	e	f	g	h
Dimensions (mm)	1	4	6	1

Figure 3.11: Schematic and Image of the 3D printed embedded RFID tag along with the dimensions.

3.4.1.2 Fabrication

A Form labs Form 2 3D printer is used for printing the tag layer by layer using stereolithographic process. The substrate for the antenna is printed first with a cavity for embedding the RFID chip. The printing is stopped at a predefined step and the chip is placed manually inside the cavity with its legs facing upwards and printing is continued to complete the structure. Vias are created over the legs of the RFID chip for electrical connectivity as explained in [62, 77] and as shown in Figure 3.12 . The parts in which metal is to be retained is printed 200 μm lower than the rest of the structure. The 3D printed structure is cured under Ultra-Violet light for 10 mins. This is followed by metallizing the structure in a two-step process, first, a 60 nm of Titanium is sputter deposited for aiding in adhesion between the plastic and Copper followed by 500 nm of Copper using a Denton Vacuum Desktop Pro system. The second step is to increase the thickness of sputtered copper to 5-6 μm using an electroplating process. After metallization, the copper is mechanically polished off and

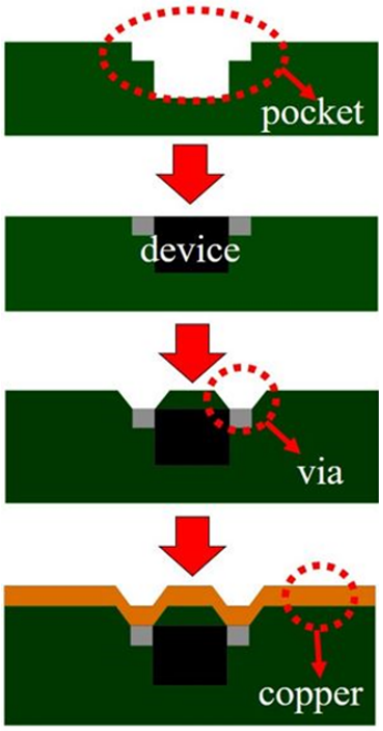

Figure 3.12: Schematic of the embedding process.

removed from the unwanted regions as explained in [48] to realize the final structure.

3.4.2 Measured Setup

In order to validate the performance of the tag, a set of experiments are performed to determine the read range. The measurement set up consists of a commercially available UHF RFID reader (Impinj Speedway R420) for radiating the query signal towards the tag. The reader consist of a circularly polarized patch antenna with a 6 dBi gain and radiates the query signal at a fixed signal strength of 30 dBm. The 3D printed RFID tag is placed in the field of view of the reader at a fixed distance as shown in Figure 3.13. The tag receives the query signal and backscatters the identification information to the interrogator.

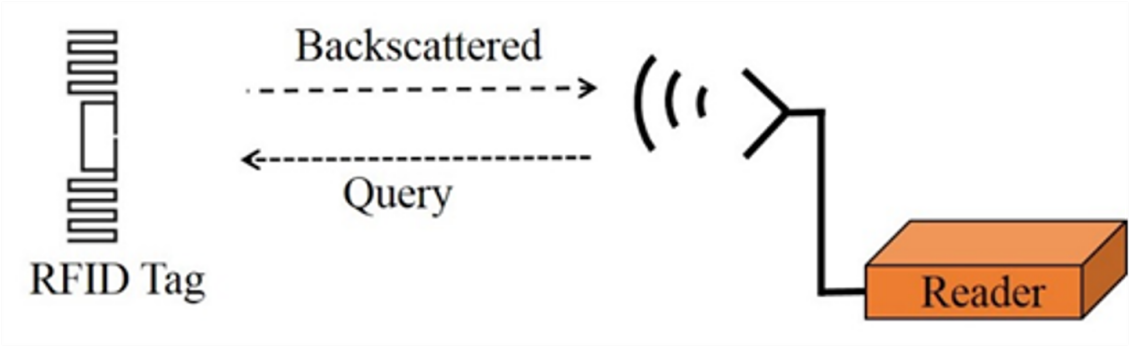

Figure 3.13: Measurement Setup for evaluating the 3D printed RFID.

3.4.3 Results

The received signal power is measured as a function of read range. The experiments are repeated thrice and the values are averaged out. The measured received power as a function of read range is shown in Figure 3.14.

It can be inferred from the graph that the printed tag is capable of achieving a read range of 20 feet ($\sim$ 6 m) with a received power of -56 dBm. The relationship between read range and received power depends on a number of factors such as multi-path interference, presence of reflecting objects in the field of view, reader power, reader antenna gain, efficiency of the tag, gain of the tag antenna, and other losses. The oscillatory behavior of the received power at increased read range is predominantly due to the effects of multi-path interference and reflections from the surrounding objects. The 3D printed tag substrate can incorporate a microfluidic channel for liquid sensing. The read range of the tag will be affected based on the dielectric loading and can be correlated to different liquids.

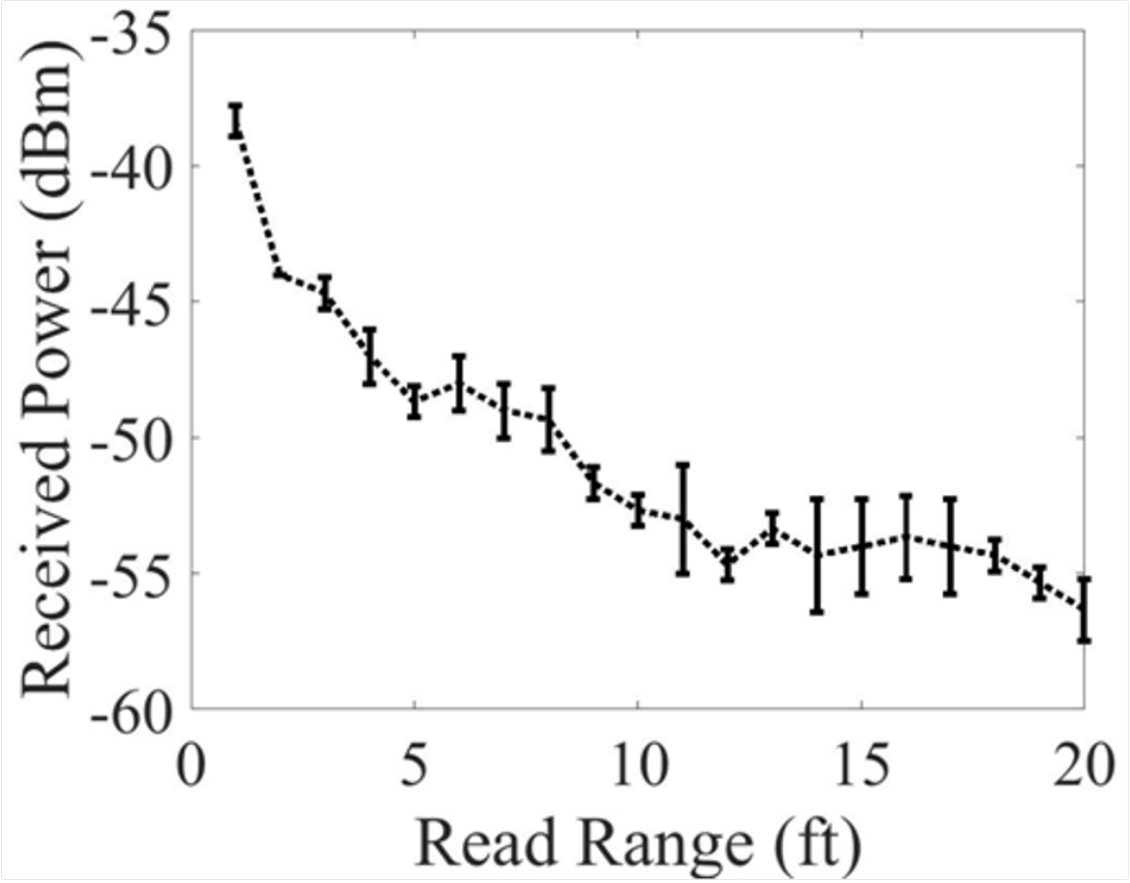

Figure 3.14: Measured received power as a function of distance between the interrogator and the 3D printed RFID tag.

3.5 Summary

In this chapter, 3D printing is exploited to fabricate sensors coupled with microfluidic channel for liquid profiling. Using this approach allows easier fabrication of the geometry without much complexity and can be completed in a short time. The multi-use nature of the sensors developed allows adapting the same measurement technique for different samples. For the cavity, different geometry optimization techniques depending on the coupling between the samples and the cavity can be investigated and different perturbation configurations with complex geometries can be studied to detect liquids having a wide range of dielectric con-

stants. The cavity resonator requires only a small sample volume of 350 μl for profiling. For the split ring resonator, the sensor requires a very small volume of sample (¡ 10 μl) for operation and the current sensitivity ($\Delta\epsilon_r \approx 6$) can be further improved by optimizing the coupling between the sample and the resonator by further optimizing the size and shape of the microfluidic channel. Nevertheless, the developed sensor can be easily adapted to monitoring liquids in real-time along the supply chain. The next step is to customize the sensor and integrate an antenna similar to the one shown in the last section for transmitting the data to a hand-held reader. Overall, this chapter demonstrates the applicability of low cost 3D pritning method as an alternative technology to traditional manufacturing of supply chain sensors for food quality control.

Chapter 4

Capacitance Based Sensor For Contamination Detection

4.1 Introduction

The third topic investigated is to develop a RFID compatible low cost wireless passive sensor for detection of food contamination. First, a wired technique using an RF tag is proposed to validate the concept followed by a field-operable RF wireless sensor for detecting bacterial load in liquid food such as milk. Milk is the primary source of nutrients and one of the highest consumed liquid foods in the United States [78, 79]. Quality control of milk and milk products ensures prevention of foodborne outbreaks that allows overall improvement in global health and well-being. Rapid detection of pathogenic bacteria in milk offers significant economic benefits for the billion-dollar dairy industry across the globe. Recent development in sensing technology assists in sustainable practices across different levels of the supply chain, guaranteeing product compliance with established safety and quality standards [80,81]. There are numerous types of bacteria which may contaminate the pasteurized milk during post-processing, transportation and storage such as E-Coli, Salmonella, Bacillus, Listeria, etc. [5-6].

Microbial analysis of milk includes conventional methods such as flow cytometry, colorimetric assays, culture methods, and dye reduction tests [82]. BactoScan FC (FossElectric,

Hillerod, Denmark) is an FDA approved commercial system for detection of bacterial count in milk [83]. It uses flow cytometry, photo electronic sensing of fluorescently-labeled bacterial cells, and RFID technology for sample identification. A simple, low cost, real-time, field-operable wireless sensor is needed with minimum liquid handling, fewer calibration steps and that is simple to use.

Two different sensing elements are investigated for detecting the bacterial load. First is a metamaterial inspired split ring resonator (SRR) and second is an interdigitated capacitor. In literature, SRR-based biosensors are developed for detection of biomolecules such as prostate cancer markers, prostate specific antigen and cortisol stress hormone [84,85]. SRRs were also used for sensing the binding of biotin and streptavidin on the sensor surface [86]. A plasmonic SRR has been demonstrated for DNA sensing in the optical regime [87]. SRR has unique properties such as high quality (Q) factor making it an ideal choice for sensing smaller changes in material properties [84]. Furthermore, these SRR can be coupled to radiating elements making it compatible with existing RFID infrastructure. In this work, the SRR is used as a direct wired sensor to detect bacterial load and for verifying the proof of concept RF biosensor.

The second approach is an RFID compatible sensor with an interdigitated capacitor as a sensing element. Such sensors with added functionality, in particular, bio-sensing of pathogens are of significant interest due to their non-contact and non-invasive nature. Recently, RFID infrastructure had been adapted for sensing different biomarkers such as antibodies and nanoparticles [88]. RFID compatible sensors have been adapted for different quality control applications such as prediction of shelf-life, freshness, and spoilage of food such as milk and fish [13].

Short interrogation range passive wireless LC tanks with high Q-factor are ideal for

detecting small changes in the target analyte. The number of pathogens can be correlated to the resonance frequency shift due to impedance loading of the LC tank, and such an approach is presented in this chapter. An RFID compatible wireless sensor tag system using an interdigitated capacitor is presented for threshold detection of milk contaminated with E. coli C3000 bacteria. The surface charge chemistry allows the bacteria in the contaminated milk to attach to the wall of the smart vial. The bacteria are labeled with dextrin-capped gold nanoparticle (d-AuNP) markers for detection. The attachment of the bacteria to the vial and d-AuNP to the bacteria is verified using microscopy images (SEM and TEM). The smart vial is placed on the interdigitated capacitor coupled to an inductor coil. The interdigitated capacitor has strong electric fields in between the fingers, enabling change in capacitance due to d-AuNP loading of the sensor. This capacitive loading shifts the resonance frequency and this shift is correlated to the threshold level of bacteria in the contaminated milk. For verification, the measured resonance shift is correlated with well-known spectrophotometry measurements. The developed biosensor is compatible with different types of pathogenic bacteria and the resonance frequency of the sensor tag can be tailored to RFID frequency to adapt to existing infrastructure. The schematic of the proof-of-concept biosensor is presented in Figure 4.1.

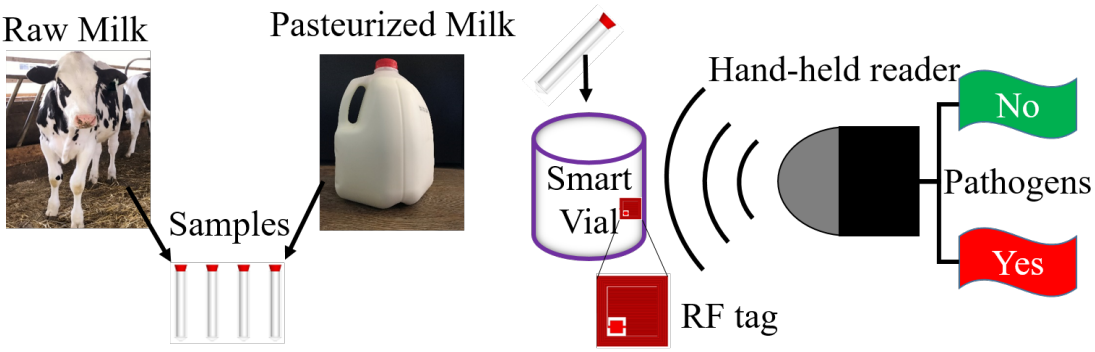

Figure 4.1: Schematic of the proof of concept biosensor.

4.2 Design and Fabrication

4.2.1 Sensor Tag

4.2.1.1 Metamaterial inspired split ring resonator Sensing Element

The split ring resonator (SRR) sensing element consists of two square split rings capacitively coupled to a transmission line, one used for measurement and the other for reference. The SRR is designed using ANSYS HFSS; and fabricated by conventional photo lithography and etching, using Rogers 3003 laminates (thickness ∼1.52 mm). The SRR is measured using a Vector network analyzer (VNA) and the resonance frequency of the first ring was at 3.4 GHz and second at 4.8 GHz. Since the first ring has higher Q-factor than the second one, it was chosen as the measurement ring for all experiments. The schematic of the developed SRR sensor along with the dimensions, measured scattering (S) parameters and electric field (E-field) distribution at the resonance frequency (3.4 GHz), are shown in Figure 4.2. The crucial element for detecting a small change in the number of d-AuNP present is to create strong electric fields in the gap region of the SRR sensor. The d-AuNP perturb the E-field in the gap region and thereby shift the resonance frequency of the SRR.

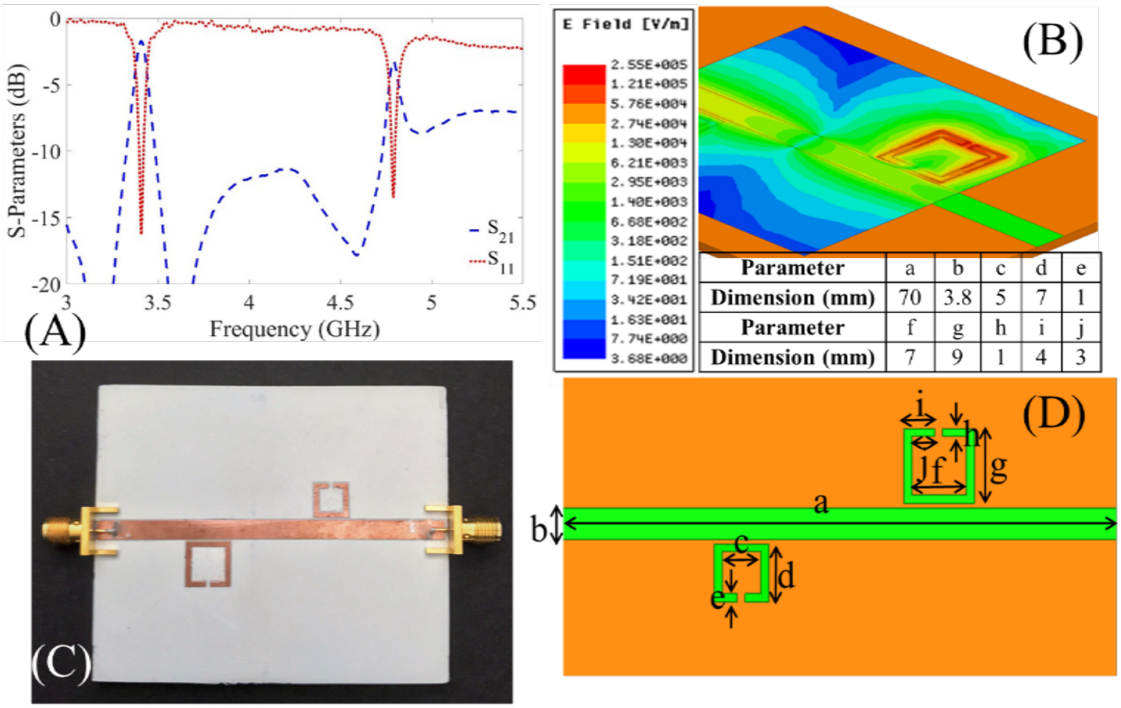

Parameter	a	b	c	d	e
Dimension (mm)	70	3.8	5	7	1
Parameter	f	g	h	i	j
Dimension (mm)	7	9	1	4	3

Figure 4.2: Measured S-Parameters (A), E-Field distribution at the resonance frequency (B), image of the SRR (C), schematic of the designed SRR (D) and a table listing its dimensions.

4.2.1.2 Interdigitated Sensing Element

The RFID compatible sensor tag consists of two key components, an interdigitated capacitor (C) coupled to an inductor (L) and an external pick-up coil. The interdigitated capacitor is designed using ANYSYS HFSS and fabricated using conventional photolithography and chemical etching. The goal of the interdigitated capacitor is to confine strong electric fields in between the fingers making it extremely sensitive to capacitive loading. The substrate chosen for this sensor design was Rogers 3003 high frequency laminate with dielectric constant (ϵ_r) of 3, loss tangent ($\tan\delta$) of 0.0013 and thickness of 1.52 mm. The schematic and dimensions of the interdigitated capacitor are shown in Figure 4.3.

The interdigitated capacitor consists of 78 fingers with a spacing of 40 m between the fingers. A commercially available inductor coil of 100 μH is soldered onto the pads of the

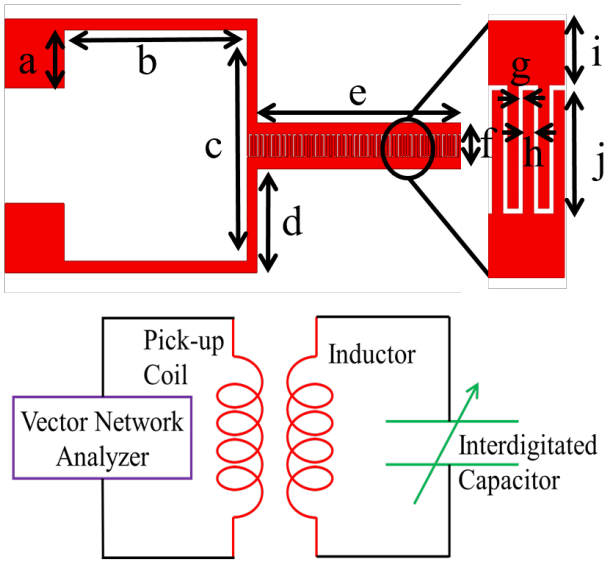

Parameter	Dimensions (mm)
a	2.5
b	9.3
c	10
d	4.5
e	10.38
f	2
g	0.04
h	0.1
i	0.5
j	0.96

Figure 4.3: Schematic and dimensions of the LC tank.

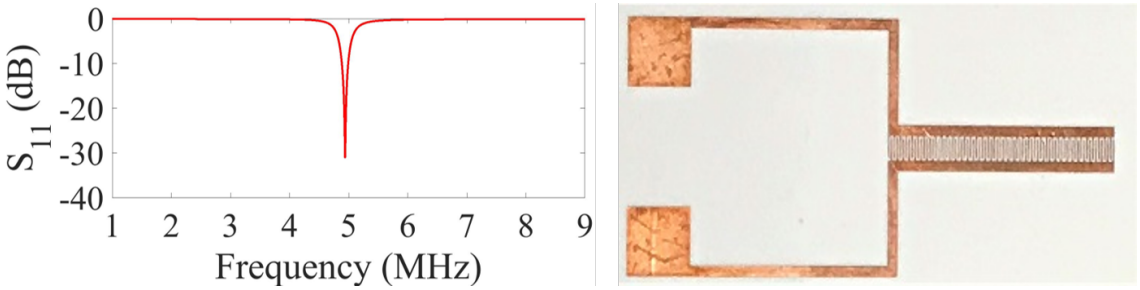

Figure 4.4: Measured S-parameters and optical image of the RF tag. An inductor coil was attached before the measurements.

interdigitated capacitor to form an LC resonant tank. Also, the inductor coil used a wireless interface to the external pick-up coil. The major advantage of choosing a commercially wound coil is that it requires less real-estate on the substrate and also it has a low resistive loss. The measured frequency of operation of the LC tank is at 4.94 MHz. The developed sensor has a high Q-factor (15.93) which allows for ease of detection of any change in resonant frequency. Figure 4.4. shows the optical image of the RF tag along with the measured resonance frequency after mounting of an inductive coil between the pads.

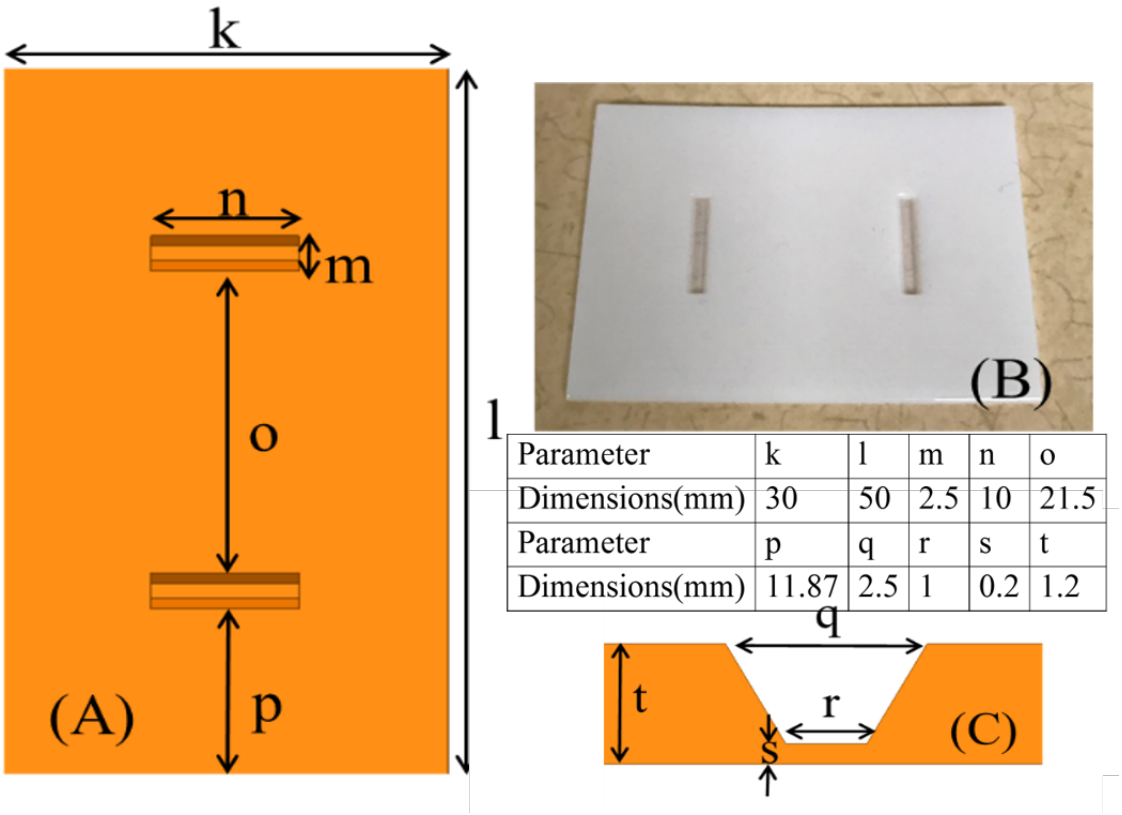

Parameter	k	l	m	n	o
Dimensions(mm)	30	50	2.5	10	21.5
Parameter	p	q	r	s	t
Dimensions(mm)	11.87	2.5	1	0.2	1.2

Figure 4.5: Schematic and dimensions of the smart vial forms.

4.2.2 Smart Vial

For proof of concept, the smart vial is represented by flat forms that were fabricated using a low-cost 3D printing approach. 3D printing has huge potential for large commercial scale up. Each form is designed to have two wells, a sample well and a reference well, each with a 20 L volume. The forms were printed (Stratasys Object Connex 350 printer) using VeroWhitePlus, with a dielectric constant of ∼2.8. The schematic and dimensions of the forms are shown in Figure 4.5.

4.3 Principle of Operation

Electrostatic forces dominate the binding dynamics of targeted pathogenic E. coli C3000 cells to the smart vial, and d-AuNP to the cells and the smart vial.

4.3.1 E. coli attachment to the smart vial

Pathogenic microbes have a tendency to attach to surfaces to improve their access to nutrients and form biofilms for protection, among other survival needs. Xu et. al. found that E. coli would bind strongly to hydrophobic fluorosilane surfaces within 10 sec [89]. The smart vial forms were printed with a thermoplastic VeroWhitePlus polymer. It has negatively charged carbonyl (C=O) groups on the surface, making the thermoplastic hydrophobic. The binding seen in SEM images in Figure 4.6A of the sample well is potentially hydrophobic binding of E. coli cells to the surface.

4.3.2 d-AuNP attachment to E. Coli

AuNP are capped with dextrin carbohydrates that have negatively charged hydroxyl (-OH) groups on the surface. The AuNP have a positive charged surface leading to an electrostatic bond between the dextrin and AuNP, forming dextrin-coated AuNP (d-AuNP). Bacteria have a negatively charged cell surface with numerous molecular structures projecting out such as flagella, fimbriae, and curli, which assist in surface adhesion and attachment to other cells and surfaces [90,91]. The negatively charged hydroxyl groups of the dextrin potentially bind to positively charged amino acid pockets within the cellular surface molecules, leading to seemingly selective attachment of d-AuNP on the E. coli surface, as seen in Figure 4.6B.

4.3.3 d-AuNP attachment to smart vial

The acrylic surface of the smart vial forms contain an abundance of electron-rich oxygen atoms with carbonyl (C=O) groups. Binding of d-AuNP to the smart vial surface as shown in Figure 4.6C is at a saturation level. Potentially, dextrins hydroxyl groups on d-AuNP are repulsed by the exposed oxygen atoms of the smart vial surface. This force results in local displacement of dextrin from the AuNP, exposing the positively charged AuNP to the electron-rich oxygen atoms. This leads to binding of AuNP to the surface oxygen atoms.

4.3.4 Correlation between frequency shift and E. coli concentration

The resonance frequency shift for both the SRR and the interdigitated sensor element are directly correlated with the number of d-AuNP that capacitively load the strong electric field regions of the both the sensors. As the concentration of E. coli increases, a lower number of d-AuNP bind to the surface of the smart vial, leading to a lower shift in resonance frequency. Hence, an inverse relationship exists between E. coli concentration and resonance frequency shift due to capacitive loading with conductive nanoparticles. The resonance frequency of the sensor is independent of the pH of the milk matrix.

4.4 Materials and Method

4.4.1 Concentrated d-AuNp

Concentrated d-AuNP pellet was prepared by sonicating 75 μL of the d-AuNP (obtained from Nano-Biosensors Lab, MSU) for 10 min, followed by centrifugation at 15,000 rpm at

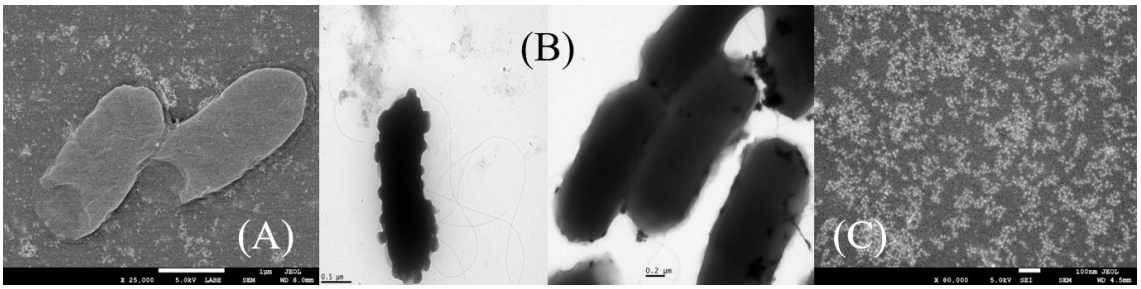

Figure 4.6: Scanning electron microscopy (SEM) images of (A) E. coli attachment to the smart vial surface, (B) Transmission electron microscopy (TEM) image of d-AuNP attachment to E. coli C3000, and C) SEM image of d-AuNP attachment to smart vial surface.

4 0C for 20 min. The supernatant was removed and the remaining volume was sonicated for 15 min to re-suspend the d-AuNP evenly. These were stored at 4 ^{o}C, and used within 24 hours of preparation. Concentrated d-AuNP are identified based on their initial volume throughout the paper, e.g. a 75 μL initial volume would be identified as AuNP75.

4.4.2 Contaminated Milk

E. coli C3000 strain was obtained from the Nano-Biosensors Lab collection at MSU. The colonies from frozen (-70 ^{o}C) culture were grown on tryptic soy agar (TSA) and a single colony was isolated and inoculated into tryptic soy broth (TSB, Sigma-Aldrich, St. Louis, MO) and grown overnight at 37 ^{o}C, then a second tenfold dilution within TSB was made and grown for 4 hr. Tenfold dilutions of this culture were made within Vitamin D milk (purchased from a local grocery store) before each experiment. A standard plate count was performed to estimate the concentration of bacteria suspended in milk.

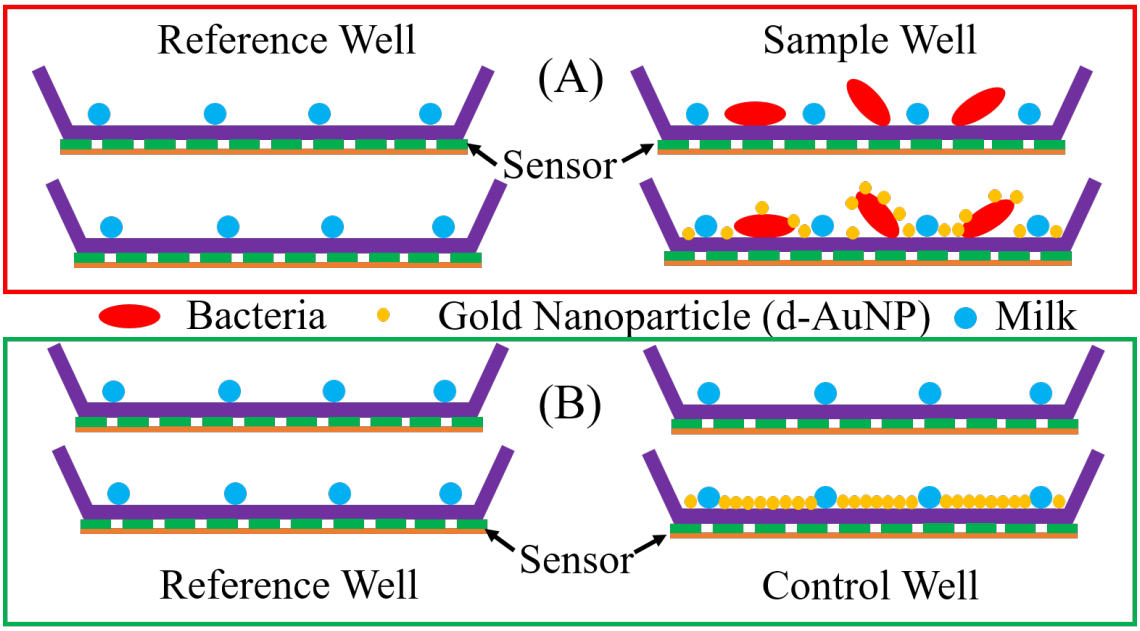

Figure 4.7: Schematic of the two-step preparation process of (A) Samples (B) Negatives.

4.4.3 Sample preparation

This proof-of-concept bio-sensing of target analyte consists of a two-step process. The first step involves filling the sample well with 20 μL of milk spiked with E. coli C3000. The cells were allowed to attach for 30 min, followed by 500 μL PBS rinse. The second step was to apply the concentrated d-AuNP to the same sample well and allow to attach for 30 min, followed by a 500 μL PBS rinse. The reference well was filled with 20 L of non-contaminated milk and allowed to attach for 30 min, followed by a 500 μL PBS rinse. This process is illustrated in Figure 4.7A. The negative control forms were prepared by similar two-step process without the presence of cells in the control well as shown in Figure 4.7B.

4.4.4 Measurement Setup

The experimental setup to analyze the performance of the SRR sensing element consists of a Vector Network Analyzer (VNA, E5070B). Two port measurements are performed and the transmission coefficients recorded for different experiments with an averaging factor of 50. For the LC tank, the experimental setup consists of a VNA and an external pick-up wire coil (11 mm diameter, 6 turns) with a cut off frequency higher than the resonance frequency of the sensor. The sensor tag was placed in the near-field region of the pick-up coil ($\sim$1 cm) and the scattering parameter (s-parameters) were averaged 50 times before being recorded.

4.5 Results

Two sets of experiments were performed to validate the sensitivity of the developed RFID compatible sensing elements.

4.5.1 RF Measurement and Spectrometry Verification

The first set was performed to demonstrate the ability of the sensor element to detect different concentrated d-AuNP standards. Triplicates of concentrated standard volumes (AuNP25, AuNP50, AuNP75, and AuNP100) were dried within the sample wells of the smart vial. The standards were placed on the sensor element and were tested for resonance frequency shift with respect to the reference wells in which no d-AuNP is present. Reference testing eliminated the error due to printing tolerance between two different forms. Three measurements were recorded for each of the standards, resulting in 9 data points per standard. The results for each standard were then averaged and plotted in Figure 4.8B and Figure 4.9A. Spectrometry was used to verify the frequency shift trend showing a similar strong relation-

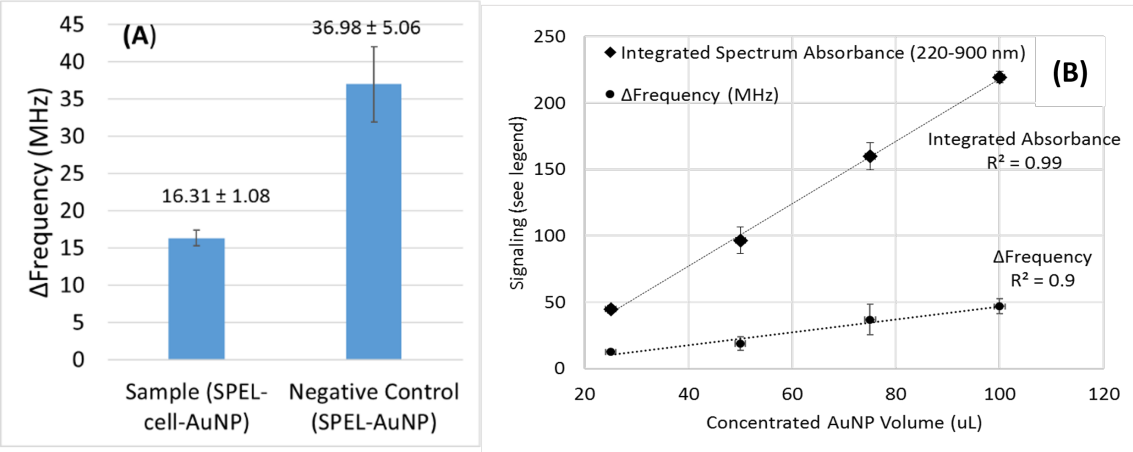

Figure 4.8: (A) Frequency shift of SRR for samples with and without cells. (B) Change in the spectral area and SRR frequency shift with respect to d-AuNP concentration.

ship between concentrated d-AuNP volume and integrated absorbance spectrum (220-900 nm). Figure 4.8B and Figure 4.9A. plots the change in integrated absorbance spectrum and frequency shift along with standard deviation for the respective sensing element, verifying the sensitivity of the developed sensing element.

4.5.2 RF Measurement and Bacterial Count

The second set was performed to demonstrate the ability of the developed RFID compatible sensor elements to detect approximately 5 log CFU/ml E. coli C3000 cells in milk. In this experiment, the samples (N=6) and negative controls (N=6) have AuNP75 applied to the lower wells as per the two-step preparation process outlined in Figure 4.7. Each form is measured three times and the results are averaged. Figure 4.8A and Figure 4.9B shows the resonance frequency shift of the attached AuNP75 for the respective elements, along with the standard deviations, between the samples with cells and milk, and negative controls with only milk. There is a clear distinction between the presence and absence of E. coli C3000 cells, demonstrating the effectiveness of the developed sensor.

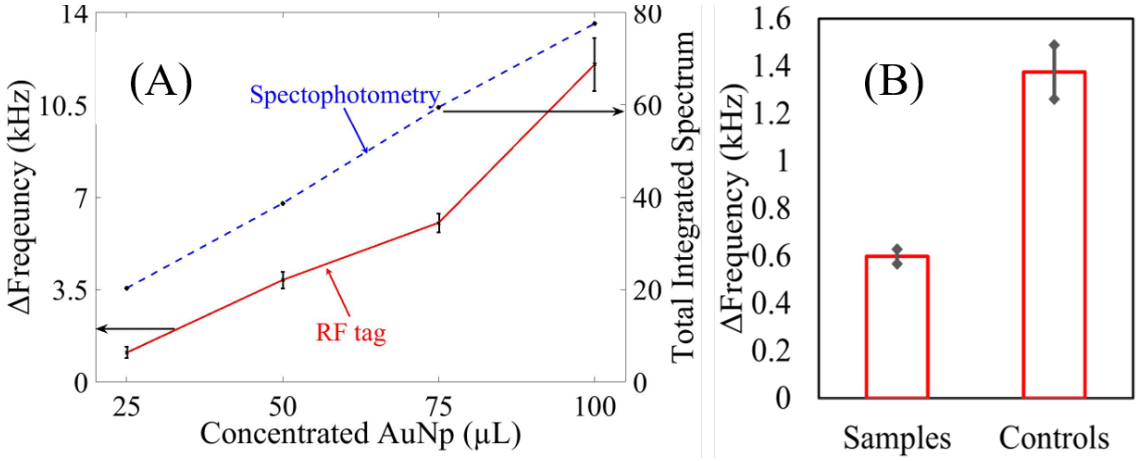

Figure 4.9: (A) Change in the spectral area and frequency shift with respect to d-AuNP concentration. (B) Frequency shift for samples with and without cells.

4.6 Discussion and Summary

The key aspects of this proof-of-concept wireless bio-sensing of pathogenic bacteria were verified using SEM, TEM, and spectrophotometry. The inverse relationship in the results clearly differentiates between the presence and absence of cells. The frequency of operation of the sensing elements can be tailored to the Federal Communications Commission (FCC) approved RFID frequency bands to make the process compatible with existing RFID infrastructure. The near-field approach is very attractive, but it has its own limitations such as read range, Q-factor, coupling factor of the pick-up coil, etc. Moreover, conventional lithography wet etching used here has its own limitations with respect to cost and limited volume production. The best possible choice for large-scale commercialization of these bio-sensors is to print them on a roll-to-roll process which reduces the complexity of manufacturing and is compatible with large volume production. The chip-less far-field approach for sensing as presented in [35] provides an opportunity to overcome the limitations of read range while allowing interrogation from long distance (>1m).

A new wireless biosensor design capable of detecting a threshold of 5 log CFU/ml bacteria with minimum handling steps is presented in this chapter. The antibody-free detection technique exploits the ability of bacteria to form biofilms. Attached cells coupled with conductive nanoparticles allow RF interrogation. The sensor shows good sensitivity and reproducibility. The non-contact and wireless nature of the sensor, if adapted to existing RFID infrastructure, provides an opportunity to monitor real-time the quality of milk through the supply chain using a simple RFID hand-held reader. The sensor design is non-selective across a broad spectrum of pathogens within liquid food or water, and thus low-cost selfcontained sensor kits are envisioned for quality control and safety.

Chapter 5

Capillary Condensation Based Sensor For Spoilage Detection

5.1 Introduction

The fourth topic investigated is to develop a RFID compatible low cost wireless passive sensor for profiling packaged food volatiles to prevent food wastage. An important food quality control technique is to monitor the volatiles emitted by packaged food over time since profiling of food volatiles allows determination of spoilage rate and freshness of the packaged food and prevents wastage [92,93]. Moreover, the real-time, end-to-end monitoring of volatiles along the food supply chain is necessary to enforce highest quality standards to ensure delivering safe and quality food for consumption, eliminating the risk of reputation and economic loss due to product recalls and helps in increasing the brand reputation.

In literature, current techniques for monitoring food volatiles are gas chromatography, mass spectrometry, rapid pre-concentration and enrichment techniques such as solid phase microextraction,headspacesorptive extraction dynamic headspace purge and trap, and electronic noses [94].The current techniques have been well studied and reported for profiling different food volatiles over the years, but they are typically battery operated, bulky or non-field operable. To overcome these limitations, a low cost, real-time, multi-use, field-operable, and a non-contact sensing method is required to advance the volatile profiling technology.

Recently, electromagnetic radiation in the microwave spectral continues to grow considerably in analysis and monitoring of the environment. Inductor-Capacitor (LC) tank based wireless sensors have been demonstrated for detection of volatile organic compounds and in particular, interdigitated capacitor or comb-drive resonator based resonant tanks media plays a prominent role in these efforts. The sensor works on the principle of change in capacitance of the LC tank due to different volatile loading conditions which in turn shifts the resonance frequency. The sensing techniques used for changing the effective capacitance of the sensor falls under any of the three different phenomenons, adsorption, absorption, and capillary condensation. For capillary condensation to occur, a substrate with pores is required into which the gas or volatile molecules condenses into liquids thereby changing the effective dielectric constant of the substrate [95]. One such example is presented in [96] where a wireless LC tank on a porous substrate is used for environmental monitoring and bio sensing.

In this chapter, the interdigitated capacitor is fabricated on a flexible porous substrate for enabling capillary condensation phenomenon for sensing. The substrate is flexible in nature making it easily adaptable to existing packaging technology. Since, the sensor is wireless and the target (e.g., packaged food) is hidden inside optically opaque materials, it is an ideal choice for detecting the presence of VOCs inside the packaging along the food supply chain for quality control and spoilage detection. An array of interdigitated LC tanks can be used to sense combination of different gases. The specificity of the gas is identified by the adsorption and desorption rates of different volatile gases. Furthermore, different thin film coatings can be used that allows certain volatiles to permeate through and aids in adsorption of volatile molecules on the substrate for enhanced specificity. The tags can be easily tuned to existing RFID infrastructure and can be made compatible for interrogated

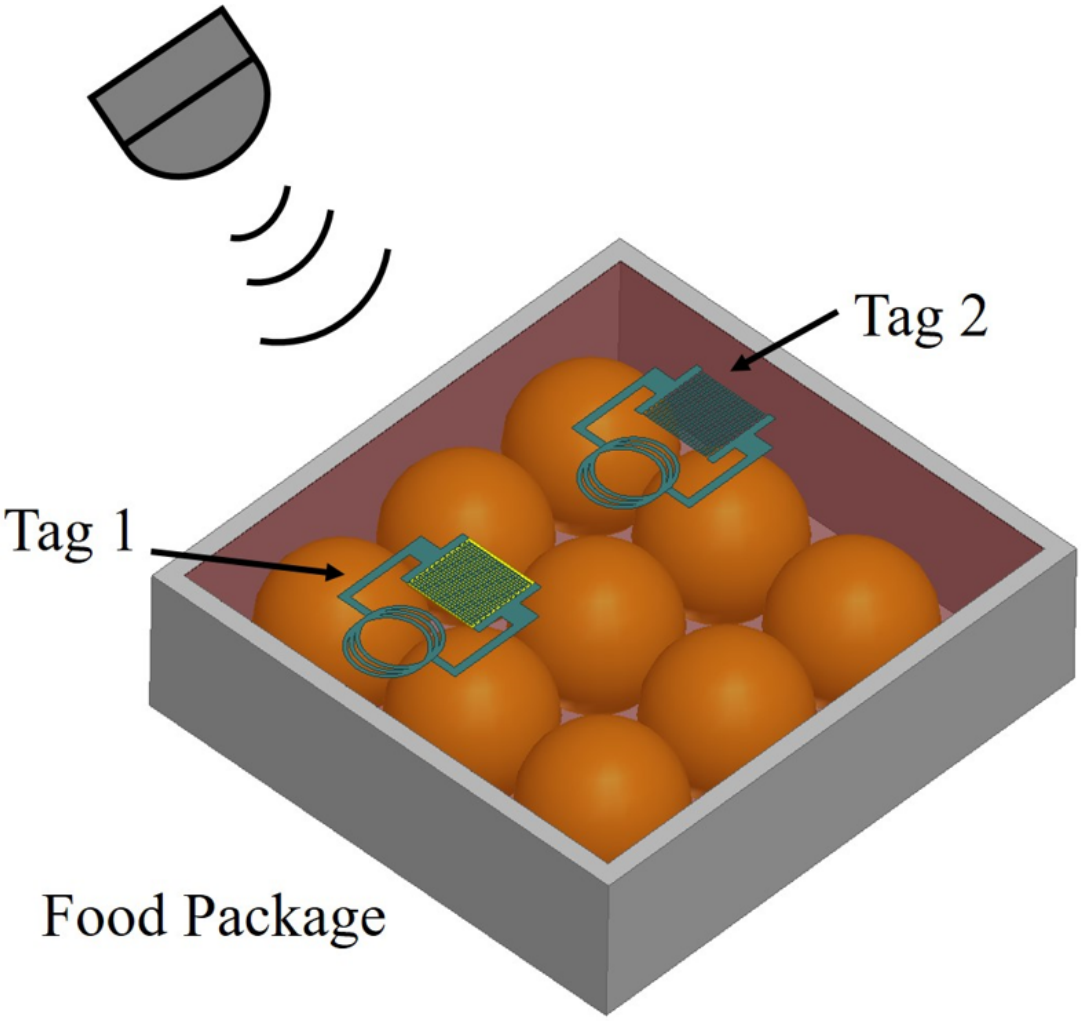

Figure 5.1: Proposed real-time volatile profiling along the fresh food supply chain with sensing tag (Tag 1) and reference tag (Tag 2).

using a hand-held reader system. The developed tags are also screen printing compatible and can be mass produced by a commercial roll-to-roll printing process. Figure 5.1 shows the proposed real-time volatile profiling of packaged food using RFID compatible sensor tags along the food supply chain.

5.2 Theory

5.2.1 Capillary Condensation

Capillary condensation occurs when the vapor or gas molecules enter into a confined porous medium due to higher inter-molecular interaction and increased van der Waals forces leading to condensation of vapor molecules below saturation vapor pressure. A meniscus is formed on the surface of the liquid-gas interface and it depends on the surface tension of the liquid and the shape of the pore [97]. The properties of liquid trapped inside micro pores as curved droplets are described by the Kelvin's equation as shown in 5.1. It provides the relationship between vapor pressure, surface tension and radius of the droplet formed due to condensation [98].

$$\ln \frac{p}{p_o} = \frac{2\gamma V_m}{rRT} \tag{5.1}$$

where, γ is the surface tension, V_m is the molar volume of the liquid, R is the universal gas constant, T is the absolute temperature, r is the radius of the droplet (radius of curvature of liquid-vapor interface), p/p_o is the relative pressure. The experimental verification of Kelvin's equation to curved interfaces ranging from 1-100 nm and observing the formation of capillary condensed liquid by multiple beam interferometry was reported by [99]. Kelvin's equation and modifications have been a topic of research for studying capillary condensation of liquids in pores over several decades. Most recently, [100] studied capillary condensation in narrow and wide grooves using modified Kelvin equation. The study presents the location and onset of capillary condensation in deep grooves when the walls are partially wet and relates the pressure required for the onset of condensation to a modified Kelvin equation

that takes into account the edge contact angle of the meniscus.

5.2.2 Concept of Volatile Sensing using nanoporosity

The fundamental concept behind sensing using substrate properties such as porosity involves following steps.

- Monolayer adsorption of gas/vapor molecules on a solid porous substrate (adsorption interface).
- Multilayer adsorption occurs after the substrate is covered with monolayer adsorbate.
- The multi-layer adsorbed vapor condenses into liquid and the condensed liquid fills the pores.
- Effective substrate dielectric constant changes based on condensed liquid volume and surface expansion due to multilayer adsorption.
- The resonance frequency of the sensor shifts.
- Correlation between resonance frequency shift and adsorption along with condensation allows identification.

The concept is illustrated in Figure 5.2.

5.2.3 Relationship between effective substrate dielectric constant and condensed volume

The effective dielectric constant of the porous substrate depends on the substrate dielectric constant (adsorbent), dielectric constant of adsorbing layer (adsorbate), the dielectric

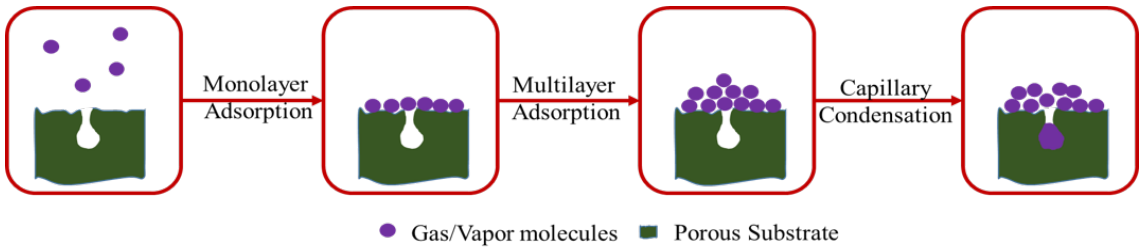

Figure 5.2: Concept of capillary condensation of gas/vapor molecules on a porous substrate.

constant of the condensed liquid inside the pores, specific surface area, or the volume of condensed liquid [101] [102]. In literature, a number of techniques exist for modeling effective dielectric constant of a solid-liquid mixtures such as soil and water [103] [104]. [105] presented that the dielectric constant increases with increase in presence of water in porous materials. A more precise model for estimating dielectric constant of the porous material in different stages of moisture saturation is presented in [101]. Here, a simple model for estimating the effective dielectric constant of the substrate based on [106] is used. The effective dielectric constant of a porous material at different stages of saturation can be modeled using weighted average of the permittivity of its constituents [106]. A general formula for this model also known as Lichteneker-Rother equation is given in 5.2.

$$\epsilon_{eff}^{\alpha} = \sum_{i=1}^{n} \phi_i \epsilon_i^{\alpha} \tag{5.2}$$

where, n is the number of porous medium components, α is the fitting parameter [-1,1], ϵ_{eff} is the effective permittivity of the medium, ϕ_i is the volume fraction, and ϵ_i is the permittivity of the ith phase [106]. 5.2 can be rewritten for a three phase system using direct weighted average model (α=1) as shown in 5.3 [107]

$$\epsilon_{eff} = (1-\phi)\epsilon_s + \theta\epsilon_w + (\phi-\theta)\epsilon_n \tag{5.3}$$

where, ϵ_{eff} is the effective permittivity, ϕ is the porosity ($0 \leq \phi \leq 1$) (total pore volume over total volume of the solid), θ is the volumetric fluid content ($0 \leq \theta \leq 1$) (volume of condensed fluid over total pore volume), and ϵ_s ϵ_w ϵ_n are the permittivities of solid (substrate), fluid (condensed liquid), and air [107]. The term $(1-\phi)\epsilon_s$ is constant since ϕ and ϵ_s are constants for a particular substrate. The term $(\phi-\theta)\epsilon_n$ depends on θ (volume of condensed fluid) and so the effective dielectric constant ϵ_{eff} of the porous substrate depends directly on θ (volumetric fluid content). It can be concluded that the substrate effective dielectric constant ϵ_{eff} is directly proportional to volumetric liquid content θ. If the pores are completely saturated, then 5.3 reduces to the 5.4

$$\epsilon_{eff} = (1-\phi)\epsilon_s + \theta\epsilon_w \tag{5.4}$$

It can be inferred that the effective dielectric constant of the substrate increases with increase in the volume of condensed liquid inside the pores. The phenomenon of capillary condensation for detecting gas molecules using a interdigitated capacitor is illustrated in Figure 5.3.

5.3 Design and Fabrication

The LC tank comprises of two key components, an interdigitated capacitor and an inductor. The inductor coil both acts as an integral part of the LC resonant tag and also it is used as an antenna to interface with the external pickup coil. The goal of the design of the capacitor structure is to confine strong electric field regions between the interdigital fingers to make it sensitive to any dielectric loading. The choice of the substrate depends directly on the ability of target gases to adsorb onto the surface and to condense into the pores. The substrate used

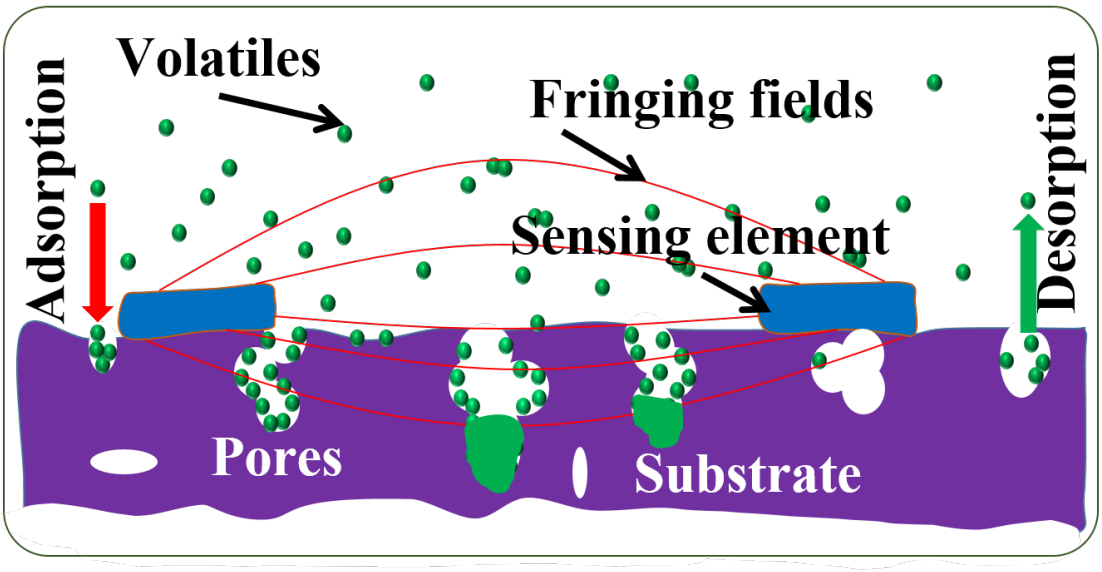

Figure 5.3: Concept of capillary condensation based sensing using interdigitated capacitor fabricated on a porous substrate.

for this design is a porous Rogers 3010 high frequency flexible laminates of thickness 0.13 mm, dielectric constant (ϵ_r) 10.2 and loss tangent (tan δ) 0.0035. The sensor is fabricated using conventional photolithography and etching process. The schematic and image of the interdigitated capacitor structure along with the dimensions is shown in Figure 5.4. The interdigitated capacitor consists of 12 fingers with a spacing of 250 μm from all the edges and in between the fingers creating a strong electric field (capacitance).

Instead of fabricating an inductor coil directly on the board, a 100 μH surface mount inductor is connected to the pads of the interdigitated structure to form an LC tank as shown in Figure 5.4B. The advantage of this approach is that different inductor coil designs are readily available and also it takes less foot print on the substrate which is necessary when an array of these sensors needs to be integrated on a small area. Typically, large value inductors with high cut-off frequency are needed to achieve resonance, when coupled with interdigitated capacitor, in the low MHz frequency range. Measured amplitude and phase

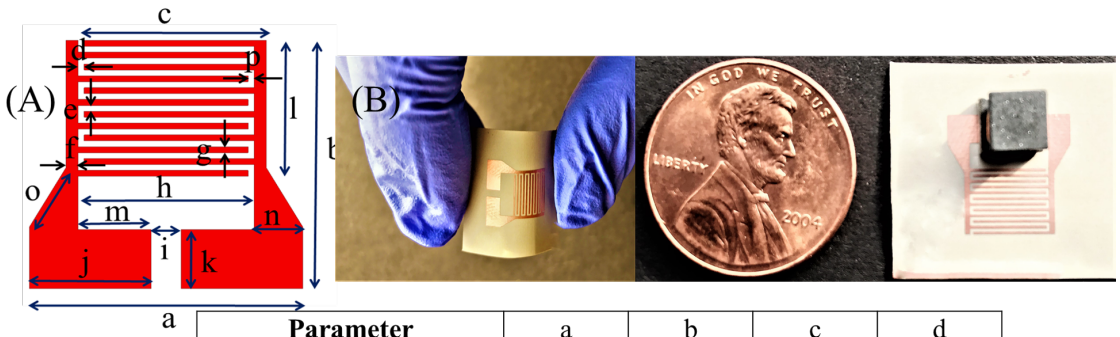

(C)

Parameter	a	b	c	d
Dimension (mm)	11.25	10.5	7.5	0.25
Parameter	e	f	g	h
Dimension (mm)	0.25	0.5	0.25	7.25
Parameter	i	j	k	l
Dimension (mm)	1.25	5	2.5	5.4
Parameter	m	n	o	p
Dimension (mm)	3	2	2.91	0.25

Figure 5.4: Proposed interdigitated capacitor: (A) Schematic, (B) Image with a commercially available inductor coil, and (C) Dimensions.

(reflection coefficient S11) of the LC tank, measured using a pickup coil, and the simulated E-field pattern at the resonance freqeuncy is shown in Figure 5.5. The LC tank shows a resonance frequency of 4.33 MHz. The pattern shows the existence of strong E-fields across the interdigitated fingers making it ideal for sensing volatile molecules.

5.4 Measurement Set-up

The experimental set up consists of a 5.5L bell jar is sealed with rubber clay from all sides and closed by a rubber cork on the top. This is to simulate a closed environment to measure gas sensing. A capillary tube of inner diameter 1.28 mm and outer diameter 1.58 mm is introduced into the jar from the sides and any air gap is sealed using rubber clay. The capillary tube is connected to a 5 ml syringe which supplies controlled volume of organic solvents. The sensor is enclosed and sealed inside the bell jar, close to the wall of the jar. The

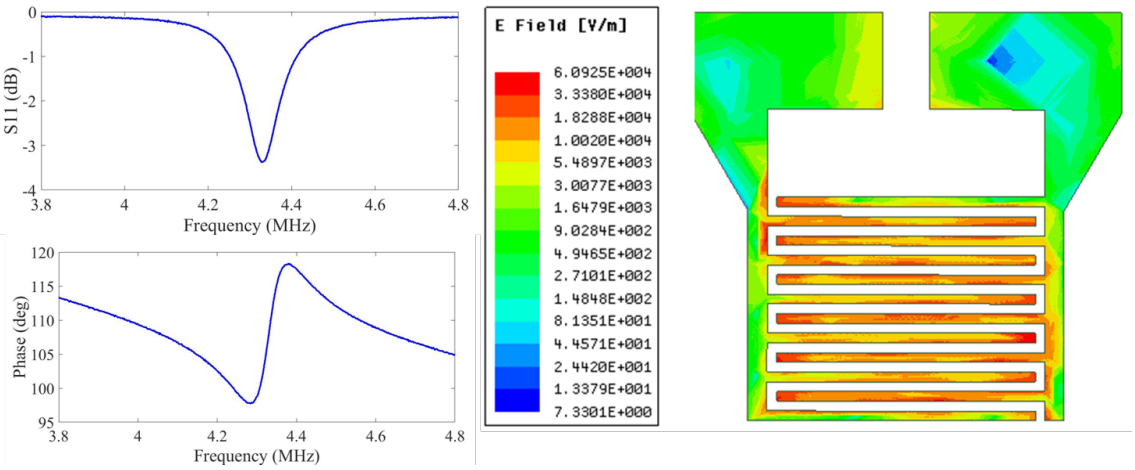

Figure 5.5: Measured return loss (S11) and phase of the LC tank (left), Simulated E-Field pattern across the cross section of the interdigitated capacitor at the resonance frequency. (right)

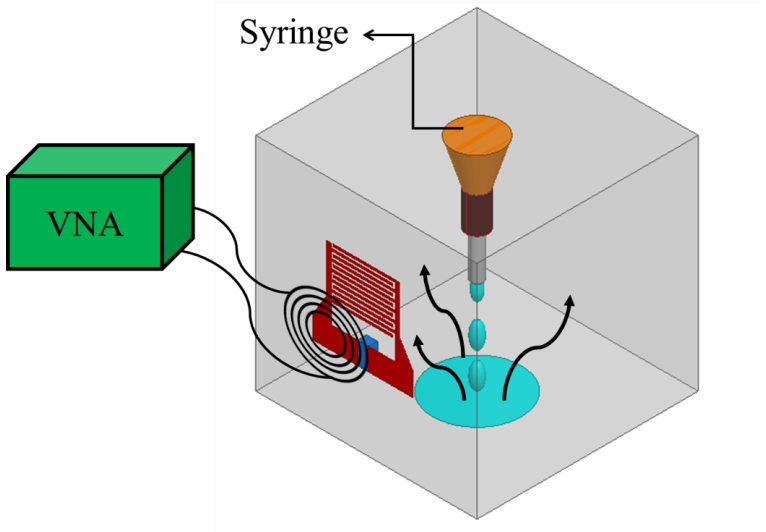

Figure 5.6: Schematic of the measurement setup.

external pickup coil is placed in the proximity of the bell jar in the near field region of the sensor. It is connected to the vector network analyzer (E5070B) to measure the S-parameters and phase. A schematic of the setup is shown in Figure 5.6.

Droplets of VOCs are introduced into the bell jar using a capillary connected to a syringe. A 10-minute waiting period was followed to allow liquid to evaporate into the surrounding

and giving sufficient time for condensation of vapor into substrate pores. All the experiments are done at room temperature. Prior to measurement of next VOC sample, the bell jar is opened and allowed to completely dry using hot air until the resonance frequency of the sensor matches with the resonance frequency in the air background. For the size of the tubing used, the volume of a drop is estimated first, a 1 ml syringe is filled with liquid and emptied drop by drop. The number of drops to empty the syringe is recorded and this gives an approximate estimate of the number of drops/ml. The experiment is repeated thrice and the average of number of drops/ml is found to be 34. The volume of a drop is estimated to be $\sim$ 0.03 cc. VOCs such as acetone, methanol, isopropyl alcohol and n-octane are used for testing the sensitivity of the sensor. The volume of volatiles used for the experiment start from 0.15 cc to 2.25 cc in smaller increments. Each volatile liquid has different vapor pressure and thereby generate different quantities of volatile molecules inside the bell jar. This leads to change in resonance of the LC sensor due to surface dielectric loading and also due to absorption by the substrate through capillary condensation. All the volatiles used in this paper are purchased from Sigma-Aldrich.

5.5 Results

5.5.1 Acetone

The first set of experiment is done to evaluate the sensitivity of the sensor in detecting acetone. Different volumes of acetone are introduced into the glass jar and allowed to evaporate. Figure 5.7 and Figure 5.8 shows the change in resonance frequency as well as phase of the sensor for different concentration of acetone. Acetone has a boiling point of 56^0C, vapor pressure of 231 $mm - Hg$, ϵ_r of 21 and $tan\delta$ of 0.054 [108].

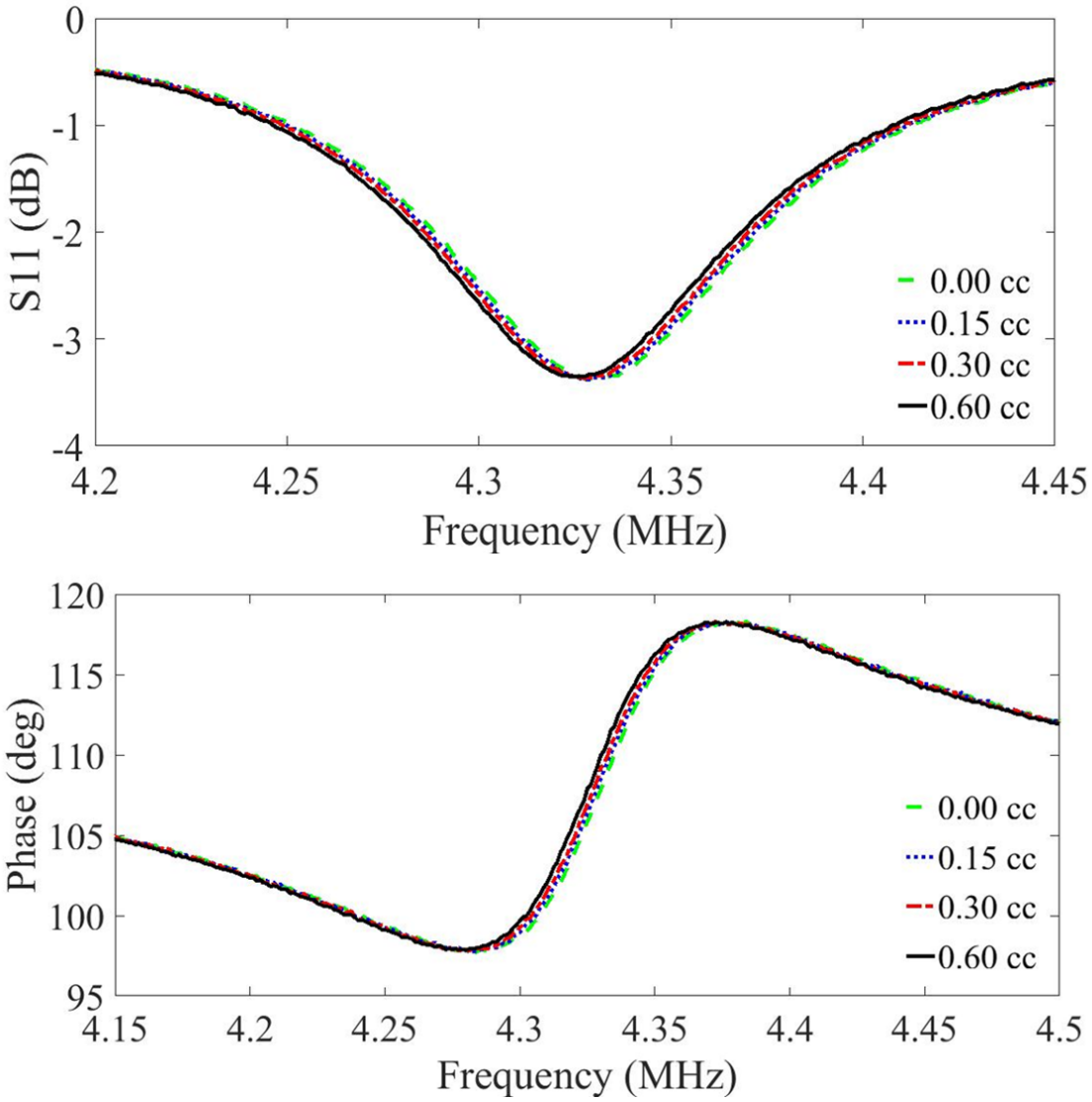

Figure 5.7: Change in S_{11} and Phase for lower concentration of acetone.

It can be inferred from the results that the resonance frequency of the sensor shifts towards lower frequency as the concentration of acetone vapor increases. This is as expected since the effective dielectric constant of the substrate increases with increase in concentration due to capillary condensation. Change in resonance can be verified by tracing the change in phase of the resonator circuit.

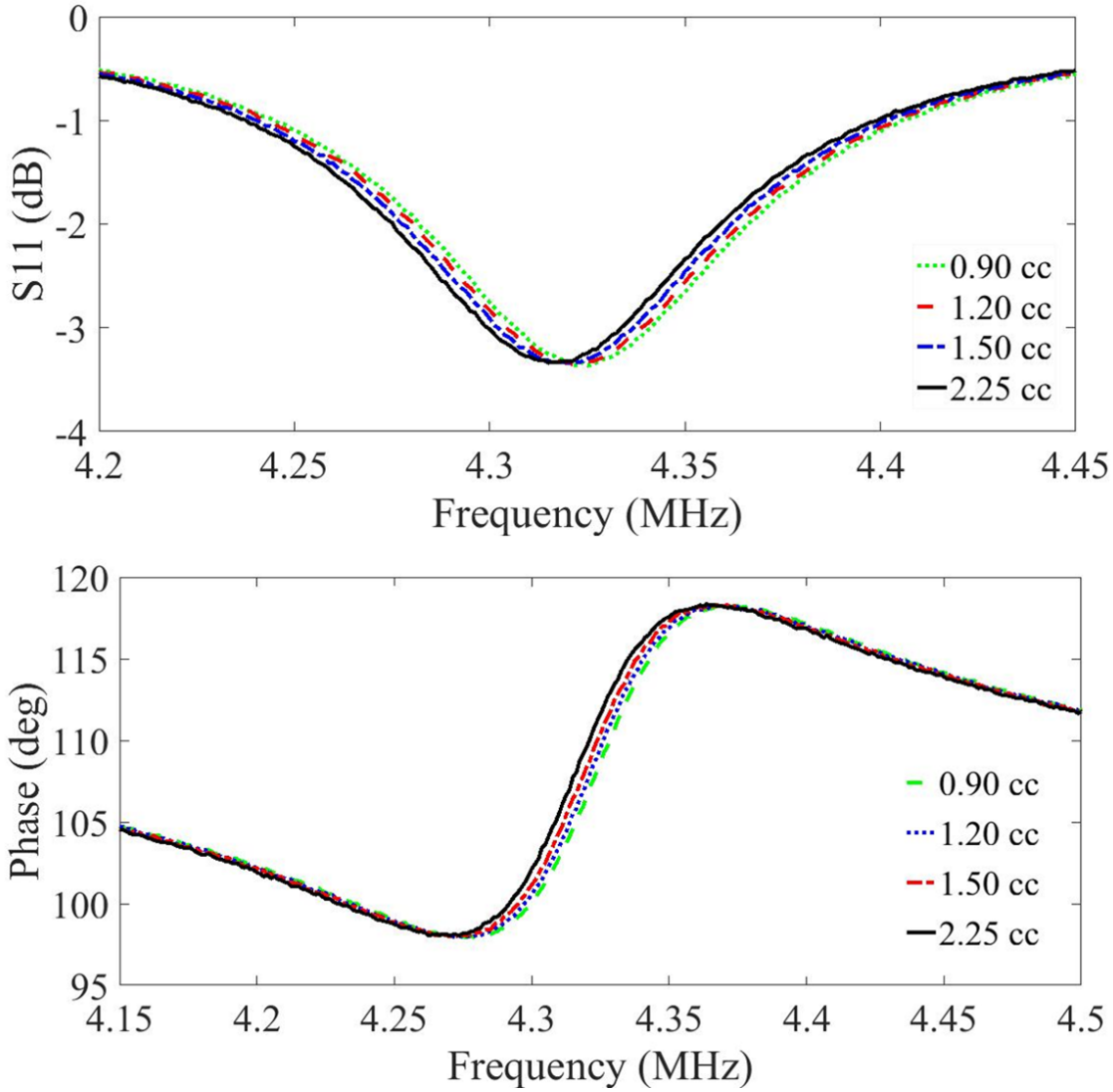

Figure 5.8: Change in S_{11} and Phase for higher concentration of acetone.

5.5.2 Methanol

A second set of experiment is carried out using methanol vapor. Same concentration range as of acetone is used in this experiment. Figure 5.9 and Figure 5.10 shows the change in resonance and phase for different methanol concentration. Methanol has a boiling point of 65^0C, vapor pressure of 127 $mm - Hg$, ϵ_r of 33 and $tan\delta$ of 0.66 [108].

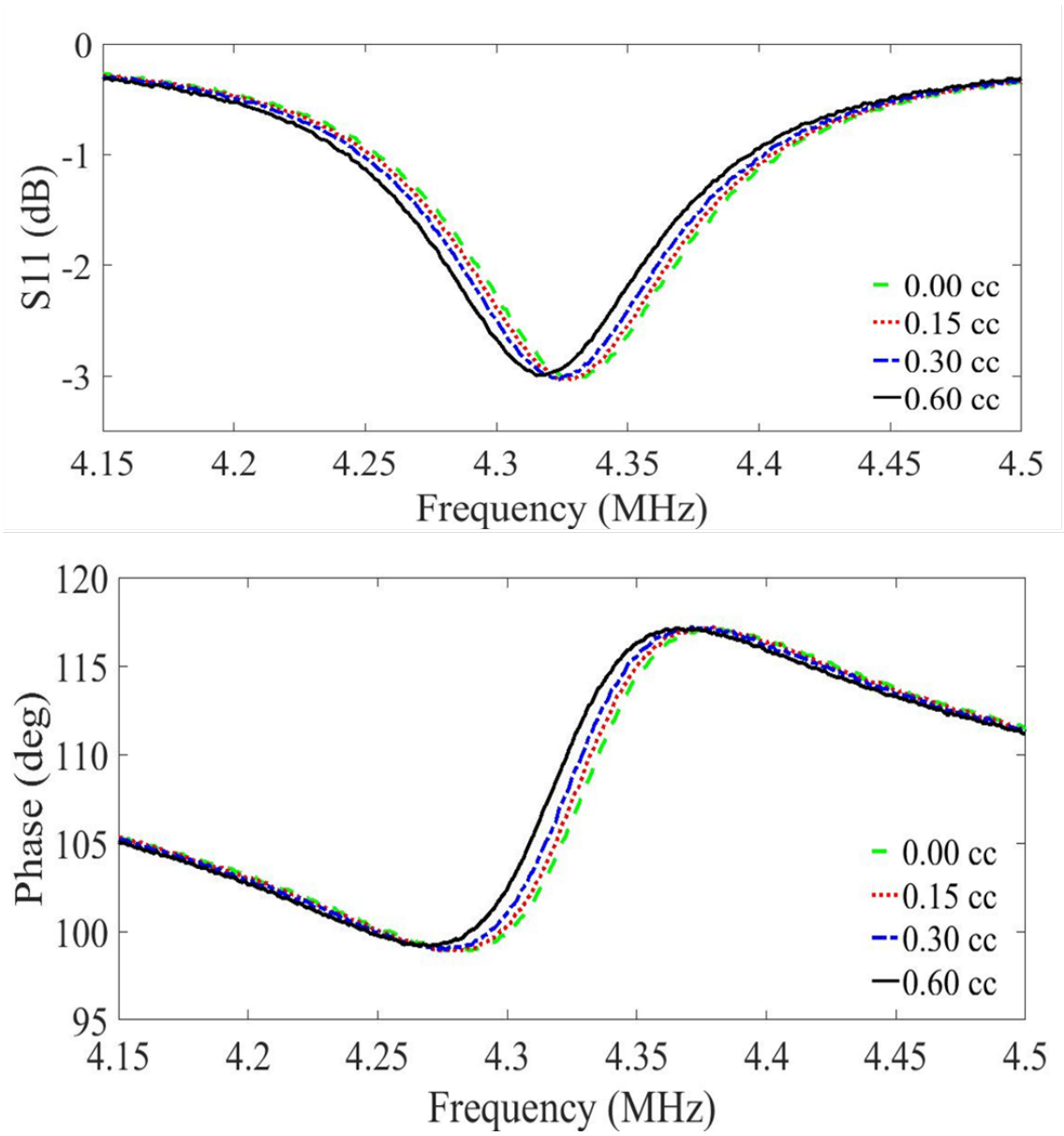

Figure 5.9: Change in S_{11} and Phase for lower concentration of methanol.

The results follow the trend similar to acetone as the dielectric constant increases the resonant frequency decreases. The Q-factor of the sensor also decreases since methanol has a higher dielectric loss (loss tangent, $tan\delta$) than acetone. Similarly, this is also observed in the phase plots.

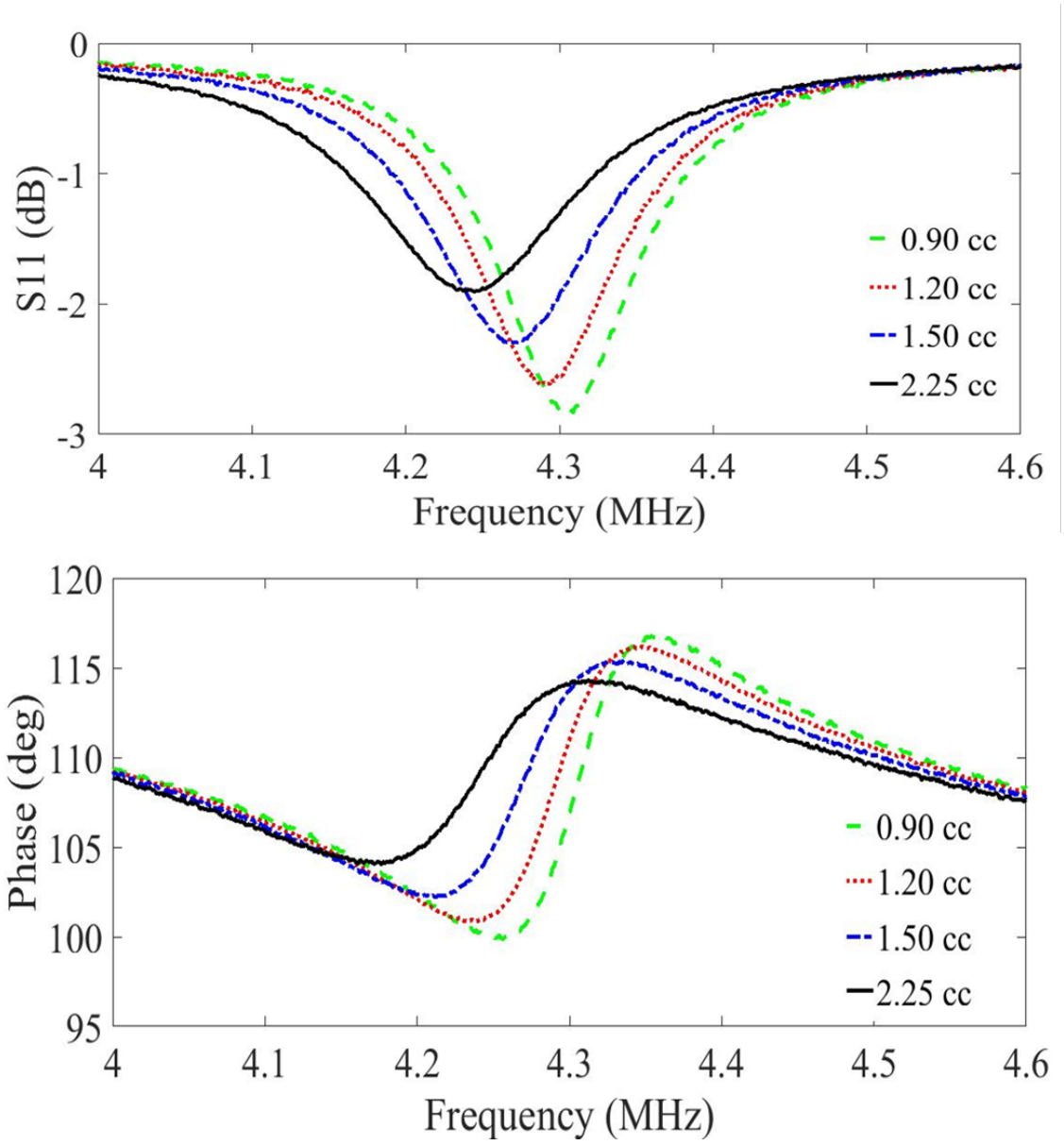

Figure 5.10: Change in S_{11} and Phase for higher concentration of methanol.

5.5.3 Isopropyl alcohol

A third set of experiment is performed using isopropyl alcohol (IPA) vapor. Figure 16 shows the change in resonance and Figure 5.11 shows the change in phase for 0.30 and 2.25 cc concentration of volatile IPA. It has a boiling point of 83^0C, vapor pressure of 45 $mm - Hg$, ϵ_r of 20 and $tan\delta$ of 0.001 [108].

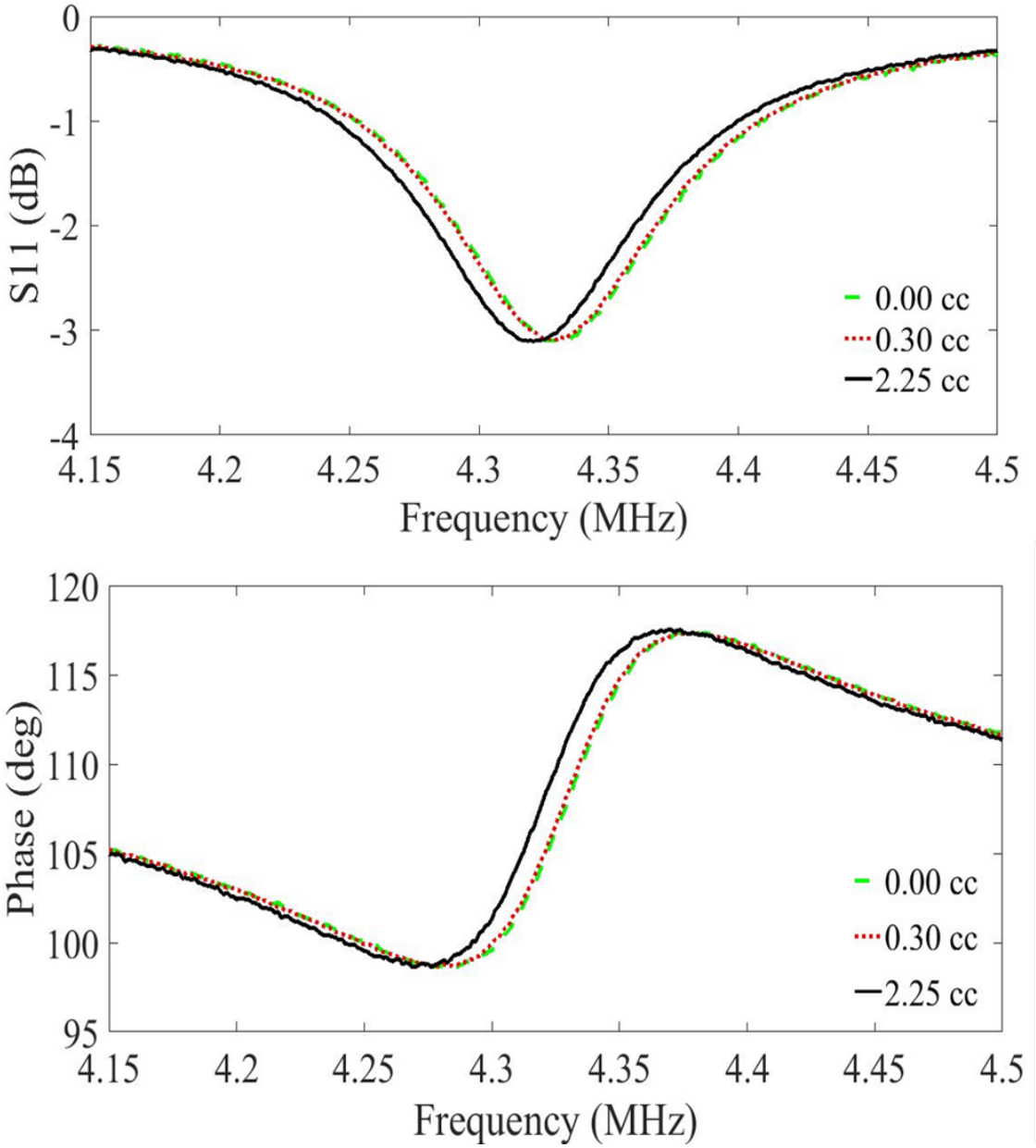

Figure 5.11: Change in S_{11} and Phase for different concentration of isopropyl alcohol.

It can be inferred from the plots that IPA has lower loss tangent and hence it does not affect the Q-factor of the sensor. Only a shift in the resonance frequency is noted as concentration of IPA increases the effective dielectric constant of the substrate material. The phase plot also shows a clear shift in resonance due to dielectric loading of the sensor.

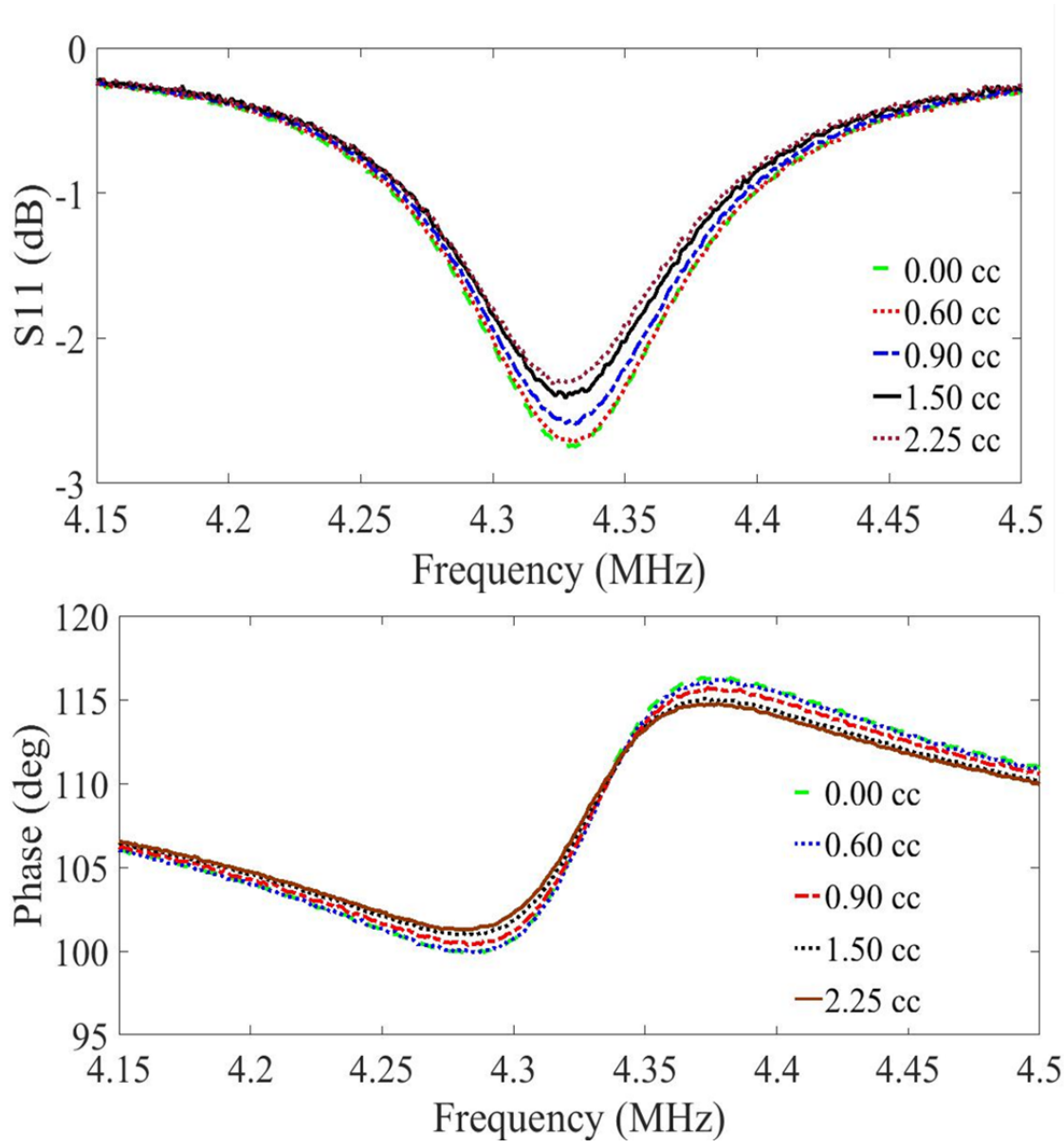

Figure 5.12: Change in S_{11} and Phase for different concentration of n-octane.

5.5.4 n-Octane

The fourth set of experiment is carried out using n-octane vapor. Figure 18 shows the change in resonance and Figure 5.12 shows the change in phase for 0.60 cc, 0.90cc, 1.50 cc and 2.25 cc concentration of n-octane. It has a boiling point of 125.7^0C, vapor pressure of 11 $mm - Hg$, and ϵ_r of 1.98 [108].

The results show that the sensor is capable of sensing very small change in volume since n-octane has a very low dielectric constant and vapor pressure. Lower vapor pressure leads to lesser number of volatile molecules in the air. Since dielectric constant is also very low, a substantial volume of octane (0.60 cc) is required for changing the resonance frequency. However, it does show that n-octane has higher dielectric loss and thus a decrease in Q-factor is noted with increase in concentration.

From the above experiments it is clear that different samples provide their own unique characteristics in the resonance frequency due their electrical properties, and thus can be used to identify different VOCs. Also, the sensor can be integrated with a heating element to further measure absorption and desorption rate to achieve further unique characteristics based on solvents boiling point. Figure 5.13 shows the change in resonance frequency with air as reference for different VOCs measured here. As the effective dielectric constant increases due to surface adsorption and loading, the relative change in frequency increases which is a clear indication of the specificity of the sensor. The substrate used here has poor porosity, and thus substrate with designed porosity (especially with open porosity) will allow further improvement in sensitivity.

5.6 Summary

In this chapter, a wireless interdigitated LC resonant tank fabricated on a flexible and porous substrate is demonstrated for sensing VOCs using dielectric loading through capillary condensation. Capillary condensation is utilized to enhance sensitivity. It is also shown that simple packaging concepts can readily be adopted to design sensors. The sensor is demonstrated to have high sensitivity and can sense very small volume (0.15 cc) of volatiles

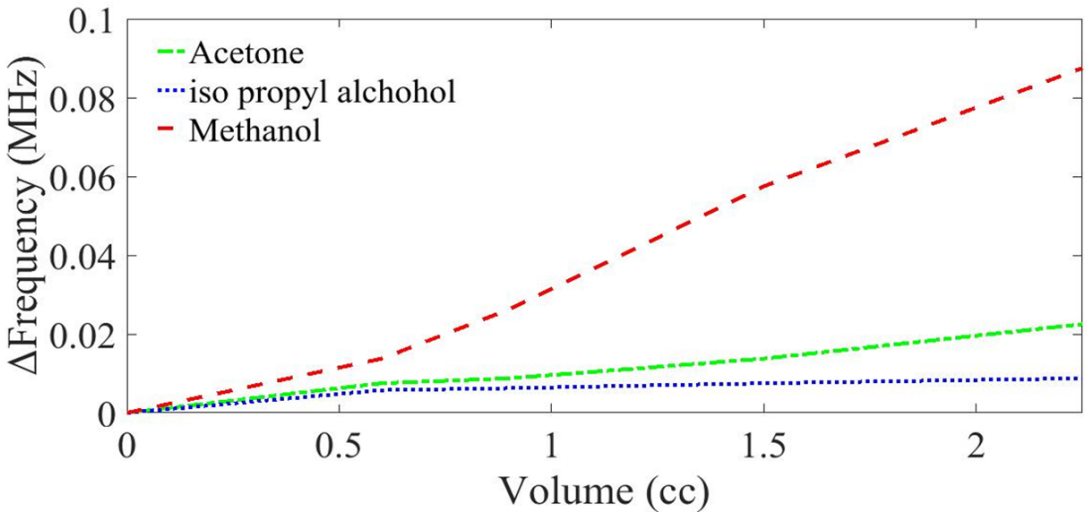

Figure 5.13: Relative change in frequency for different concentration of VOCs.

in air. Since the tags are flexible, these can be mounted onto food packaging for detecting volatiles to determine the freshness and quality in food supply chain. It can also be tailored to FCC approved RFID frequency range and can be easily integrated with existing RFID infrastructure. Moreover, the tag does not depend on any microchip for its operation which makes it easier to be printed and enables a cost effective commercial production. These LC tanks can be integrated as an array format to sense multiple gases, similar to an electronic nose.

Chapter 6

Thin Film Absorption Based Sensors for Food Spoilage Detection

6.1 Introduction

The fifth topic investigated is to improve the specificity of volatile sensors developed in the previous chapter by introducing different thin-film coatings that absorb certain gas molecules which are markers for spoilage detection. In the previous chapter, Inductor-Capacitor (LC) based resonant tanks have been proposed for aroma profiling of food along the supply chain using capillary condensation. The basic operating principle of these sensors is to detect change in impedance of the sensor tag due to adsoprtion, absorption (permeation) or condensation of gas molecules onto the sensor substrate. A combination of the three techniques can also be used for enhancing specificity as well as sensitivity. For absorption, two different techniques are commonly used, substrate absorption where the sensor substrate absorbs the gas molecules or thin-film absorption where the sensor surface is coated with a thin absorbing film that traps the gas molecules. Among the thin film technique, there are two methods of detection, one method is to use the thin-film to block certain molecules and the other is to allow certain molecules depending on the affinity of the film to the gas molecules. In this chapter, two different photo resists (SU8 and S1813) are chosen for coating the surface of the sensor and evaluated for sensitivity and specificity for detecting different volatile organic

compounds. This is followed by investigating a conductive thin-film polymer for Ammonia gas detection. A good candidate which has high affinity towards Ammonia gas molecules is Polyaniline (PANi). Ammonia detection technique using conducitve polymer PANi has been used as spoilage indicator in a number of packaged food such as fish, meat, and protein rich food items [13, 109]. A comprehensive review of Ammonia sensors is presented in [110].Table 6.1 lists different PANi based ammonia sensors presented in literature over the last five years.

Table 6.1: PANi based resistive Ammonia sensors.

Interrogation Type	**Sensitivity (ppm)**	**Sensor**	**Reference**
Direct Probed	100	Pellet	[111]
Wireless/Passive	100	LC tank	[112]
Direct/Probed	30	Interdigital	[113]
Wireless/Active	6	Interdigital	[114]
Wireless/Passive	3	Interdigital	**This Work**
Wireless/Active	1	Interdigital	[115]

6.2 Design and Fabrication

Two different interdigitated capacitor designs are presented for thin-film evaluation. The first design (volatile tag) is coated with sensitive photoresists and consists of an inductor-capacitor resonant tank for volatile profiling. The second design (ammonia tag) is coated with conductive polymer and is presented in two different configurations, direct wired and wireless short range for ammonia profiling.

6.2.1 Volatile tag

6.2.1.1 LC Tank

The sensor tag consists of an interdigitated capacitor and an inductor forming an inductor-capacitor (LC) resonant tank. An external pick interrogates the LC tank up coil and the inductor also serves as an interface between the tag and the reader (external coil). The inductor used in this work is a commercially available chip inductor (100 μH) similar to our previous work presented in [108]. The reason for choosing a commercial inductor instead of fabricating an inductor coil is to minimize the real-estate occupied by the sensor tag. The interdigitated capacitor has 24 fingers of 200 μm width and 200 μm spacing on all sides. The spacing between the lines was chosen such that strong electric fields are confined in between the fingers and strong fringing fields exist in close proximity above the substrate. The substrate chosen for fabricating the LC tank is a flexible and porous Rogers 3010 high frequency laminate with a dielectric constant (ϵ_r) of 10.2, loss tangent ($tan\delta$) of 0.0035 and a thickness of 130 μm. Figure 6.1 shows the schematic and image of the interdigitated capacitor along with its dimensions.

6.2.1.2 Thin-film photoresist coating

The fabricated interdigitated capacitor is coated with a volatile sensitive photoresist such as SU8 or S1813 using a spin coating and photo patterning technique. S1813 is coated on the surface of the sensor by spin coating at 3000 rpm for 30 sec, followed by ultraviolet exposure for 25 sec, and developing using MF319 developer solution for 35 sec. S1813 is a negative photoresist and hence the UV exposed region does not retain the photoresist during the developing process. The photoresist is coated on both the front and the back of

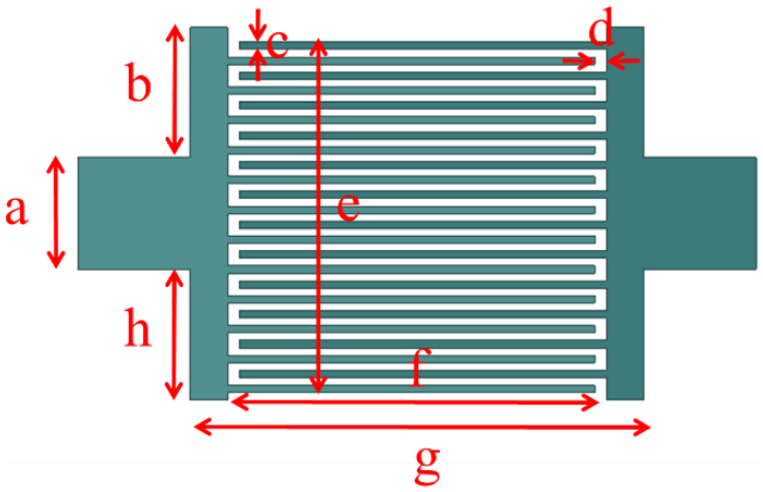

Parameter	a	b	c	d
Dimensions (mm)	3	3.5	0.2	0.2
Parameter	e	f	g	h
Dimensions (mm)	9.4	9.8	12.1	3.5

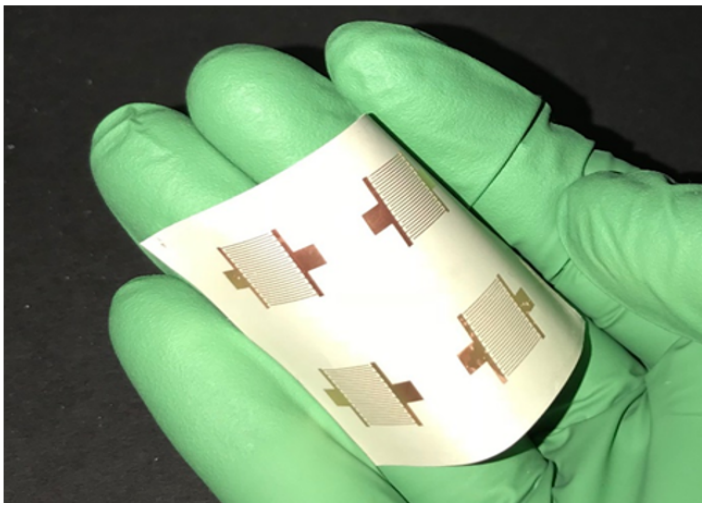

Figure 6.1: Schematic of the interdigitated capacitor (top), dimension in mm (middle), and the fabricated image (bottom).

the substrate to maintain uniformity.

The following procedure is followed to realize approximately 200 nm thick SU8 coating on the interdigitated capacitor. SU8 is diluted using SU8 thinner (1:3 ratio by weight) and spin coated at a speed of 500 rpm for 30 seconds. A pre-exposure bake of 10 min follows this

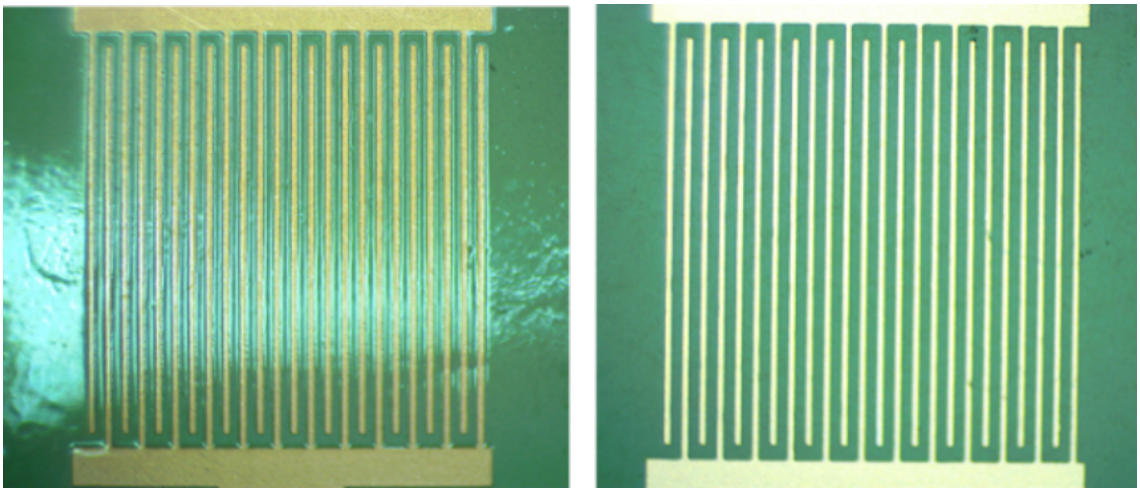

Figure 6.2: Image of the sensor tag coated with SU8 (left) and without any coating (right).

step at 65 ^{o}C and 30 min at 90 ^{o}C. The prebaked substrate is exposed to ultraviolet (UV) light using a mask aligner for patterning the positive photoresist onto the substrate. The UV exposed regions on the substrate retain the photoresist during the developing process. The exposure time was 10 min followed by post exposure bake for 1 min at 65 ^{o}C and 10 min at 90 ^{o}C. The final step is to develop the SU8 using Microchem SU8 developer. A thin uniform coating of approximately 150-200 nm is realized on the surface of the sensor. Next, a thin film is realized on the backside of the sensor following a similar process to maintain uniformity [116]. Figure 6.2 shows the image of the sensor tag with and without coating.

6.2.2 Gas tag

In this section, the design and fabrication of the sensing element is presented. The element chosen is an interdigitated capacitor fabricated on a flexible Rogers XT/Duroid 8000 high frequency laminates with a dielectric constant of 3.2 (ϵ_r) and a loss tangent of 0.0035 ($tan\delta$) with ten pair of fingers. The width of the fingers and the spacing between them is fixed to be 250 μm. The fabrication process is shown in Figure 6.3.

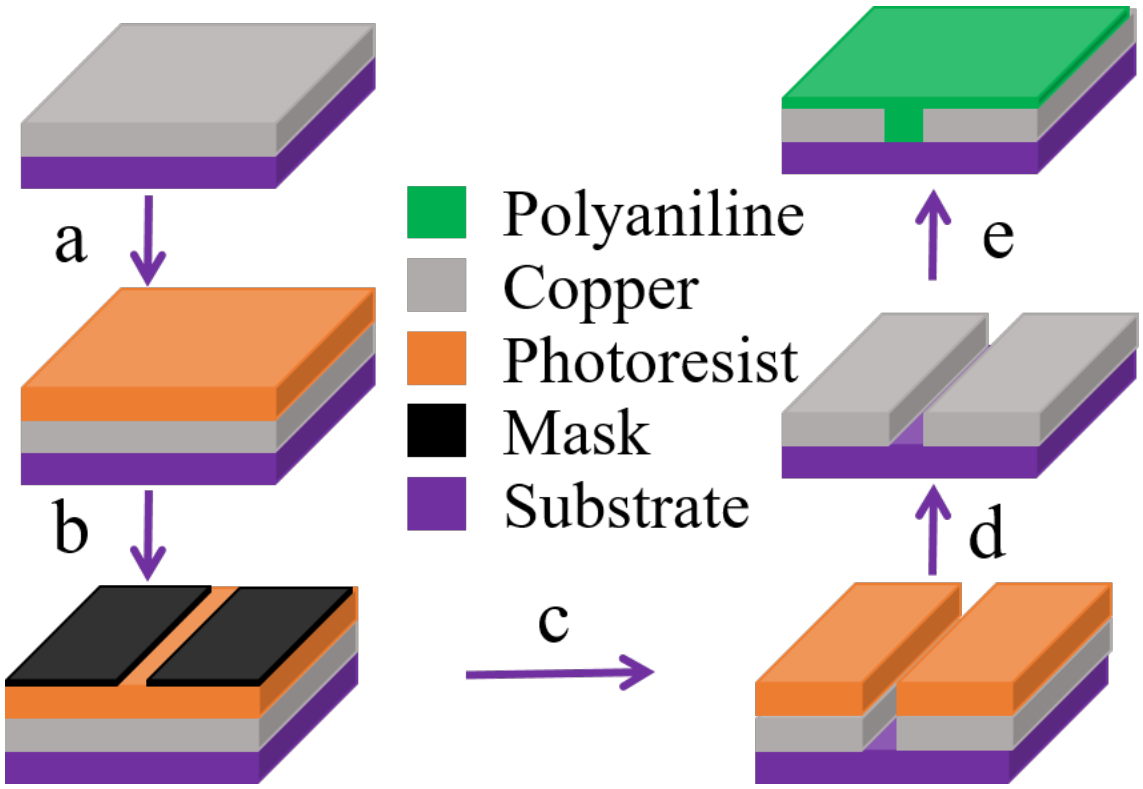

Figure 6.3: Schematic of the fabrication process for the interdigitated sensor a) Spin coat photoresist, b) expose, c) develop, d) etch, e) spin coat and bake PANi.

All the chemicals used are obtained from Sigma Aldrich. The interdigitated pattern is etched onto the Roger's substrate using a standard photolithography and Copper etching process (steps a-d in Figure 6.3). This step is followed by coating a thin-film of PANi over the interdigitated sensor. For this purpose, PANi in emeraldine salt form is mixed with a solvent 1-Methyl-2-Pyrrolidone in 1:100 ratio by weight. A 30 min of sonification allows proper mixing of the salt in the solvent. The mixture is spin coated on the interdigitated sensor using a Laurell Technologies Spinner (WS400B-6NPP LITE) at 100 rpm for a minute and this is followed by a baking step of 120^o C for 30 min. Spin coating followed by baking is repeated four times to obtain a near uniform coating of PANi over the sensor surface. Figure 6.4 shows the schematic of the sensing element and the image of it before and after

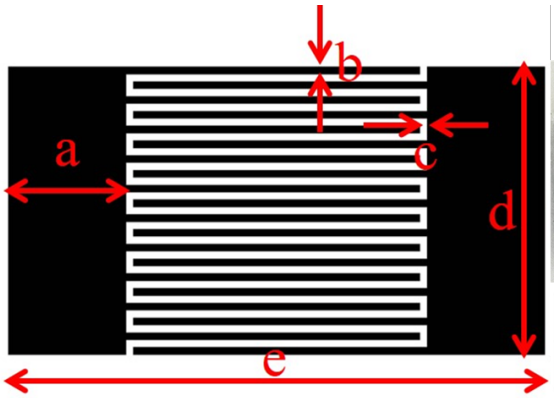

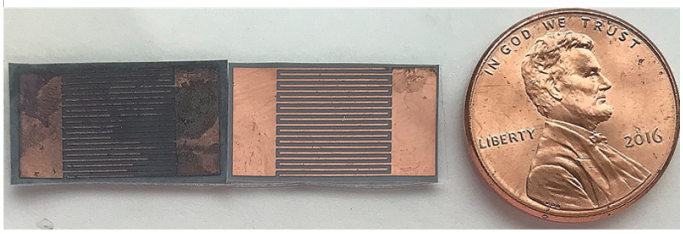

Parameter	a	b	c	d	e
Dimensions (mm)	4	0.25	0.25	9.75	18.25

Figure 6.4: Schematic of the interdigitated capacitor (top left), image of the interdigitated capacitor with and without PANi coating (top right) and its dimensions (bottom left).

PANi coating along with dimensions.

6.3 Measurement Set-up

6.3.1 Volatile tag

For measurement, two tags, coated (tag 1) and uncoated (tag 2) are measured simultaneously using tag 1 as reference. The measurement set up consists of a sealed chamber (a glass jar), the two tags (coated and uncoated), and two external pick up coils. The external coils are placed in the proximity of the glass jar, in the near-field region of the tags and connected to a vector network analyzer (E5070B) for recording the phase and frequency data. The sensor tags (1 and 2) were placed enclosed inside the sealed glass jar (500 mL) with inlets for microfluidic tubing to introduce volatiles into the jar. The glass jar was sealed using clay to prevent volatiles from escaping into the atmosphere. After each measurement, the jar is opened up, blow dried using hot air and resealed to prevent cross-contamination between different volatiles. Figure 6.5 and Figure 6.6 shows the schematic of the measurement setup

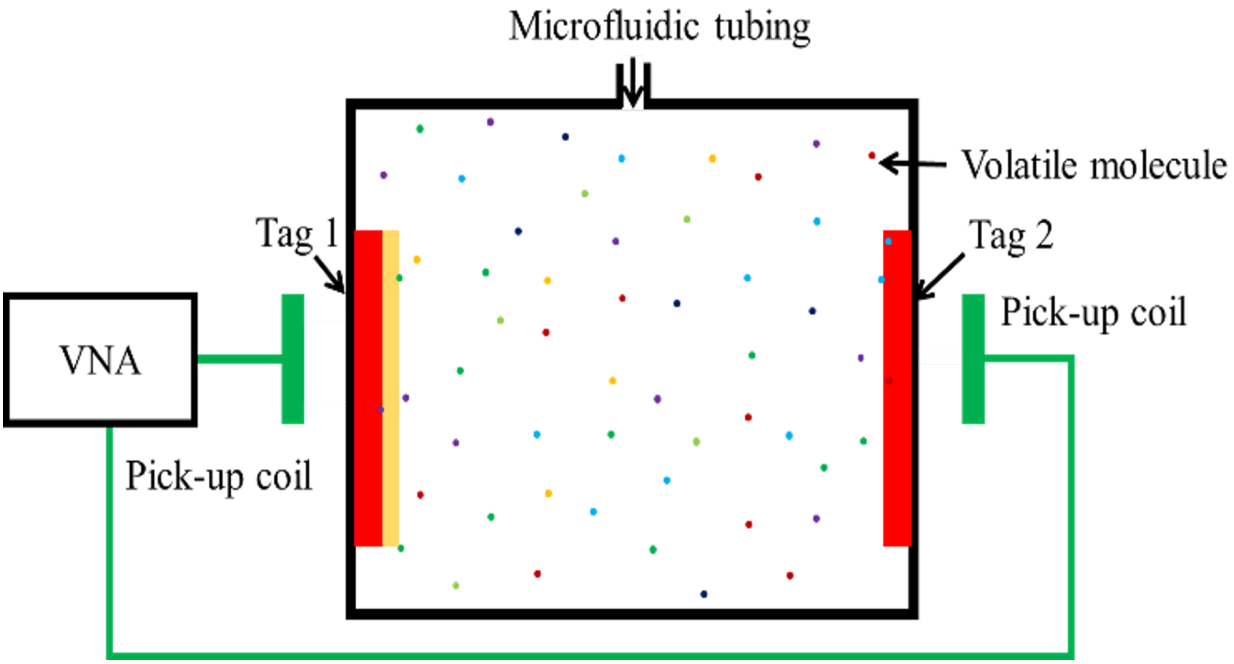

Figure 6.5: Schematic of the measurement set-up.

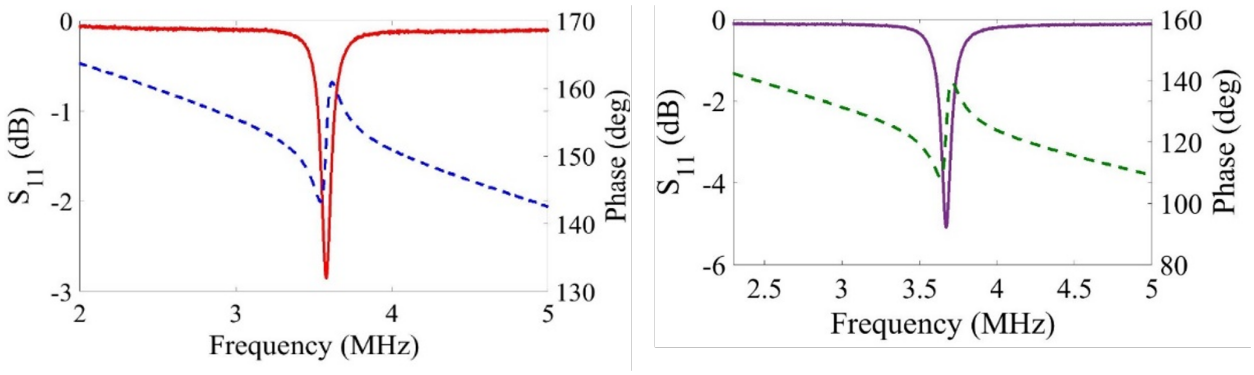

Figure 6.6: Measured reflection coefficient and phase for unloaded tag 1 (left) and tag 2 (right).

and the measured reflection coefficient and phase for unloaded volatile tags. The measured resonance frequency of tag 1 is at 3.58 MHz, and that of tag 2 is at 3.67 MHz. The difference in resonance frequency is due to loading of the thin-film coating and also due to fabrication tolerances on the dimensions of the interdigitated lines due to wet etching (over or under etching).

6.3.2 Gas tag

The PANi coated interdigitated capacitor is coupled to a commercially available 100 μH inductor to form an Inductor-Capacitor (LC) resonant tank for wireless interrogation. The inductor is soldered directly on the pads of the interdigitated capacitor. An external pickup coil is placed on the outer walls of the glass jar to read the resonance frequency (reflection coefficient) of the LC tank using a Vector Network Analyzer (E5070B) in order to monitor the change in resonance as the capacitor is loaded with Ammonia gas. Figure 6.7 shows the schematic of the measurement set-up and the measured reflection coefficient.The resonance frequency of the unloaded LC tank is at 2.87 MHz.

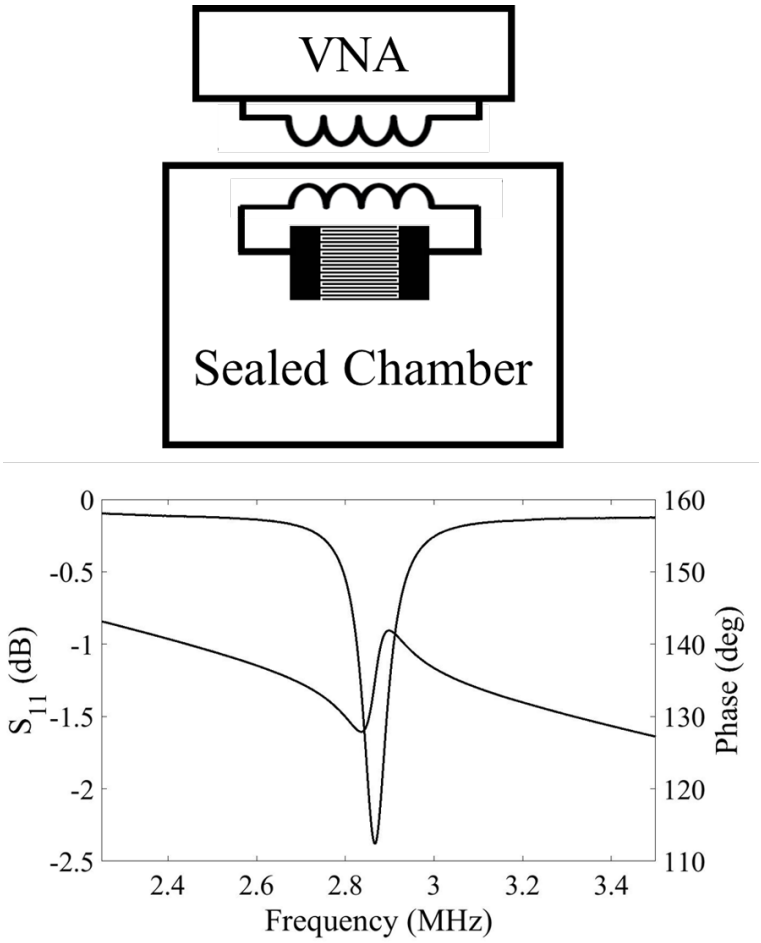

Figure 6.7: Schematic of the measurement set-up (top) with measured reflection coefficient (bottom).

6.4 Results

6.4.1 Volatile tag

The first set of experiments are performed to validate the sensitivity of the sensor tag coated with SU8 photoresist. Iso-propyl alcohol, methanol, and acetone with a dielectric constant (ϵ_r) of 20, 33, and 21 respectively are introduced in different volumes [108]. The reflection coefficient (S_{11}) and phase are recorded for each volume using the VNA. The averaging factor was set to 25 for all the experiments, and each experiment is repeated twice and averaged

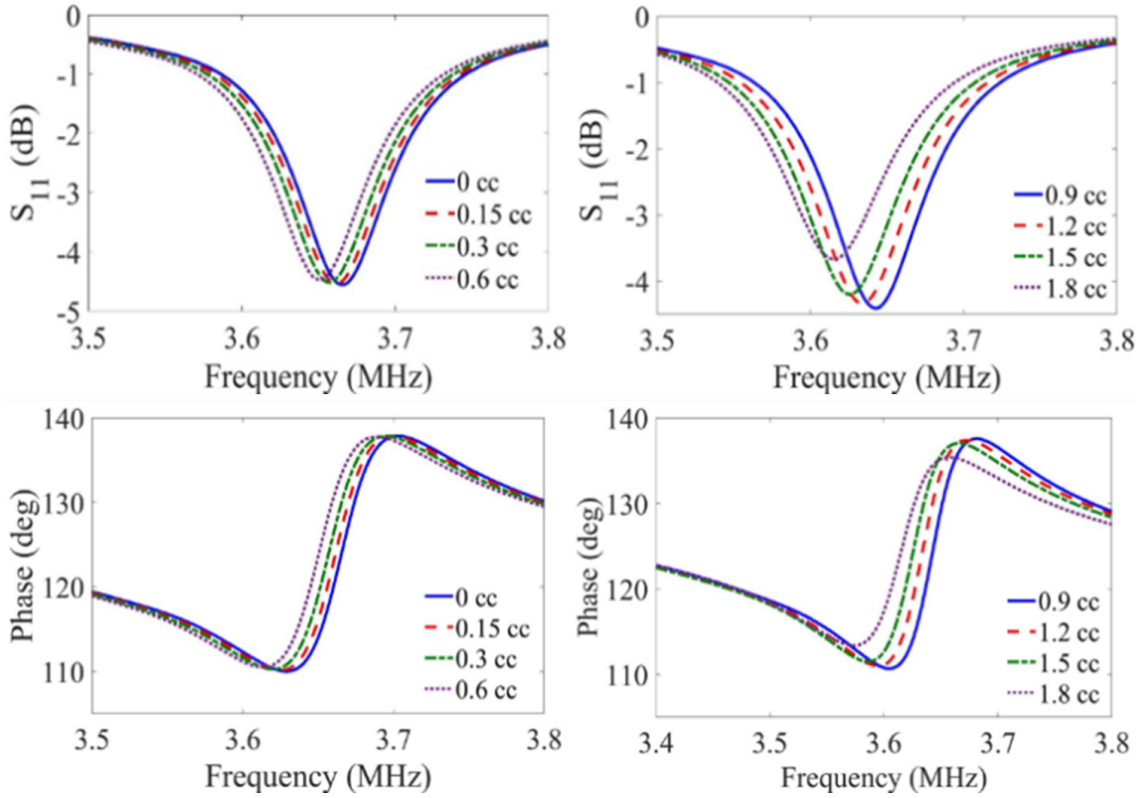

Figure 6.8: Change in S_{11} and phase for different concentrations of methanol vapors for tag 1.

out.

6.4.2 SU8 coated tags

6.4.2.1 Methanol

The first set of measurements are performed using methanol vapors. Different concentrations of methanol ranging from 0.15 cc to 1.8 cc were introduced into the chamber, and the frequency shift is monitored. Figure 6.8 and Figure 6.9 shows the resonance frequency and phase shift for tag 1 with SU8 coating and tag 2 without the SU8 coating, respectively.

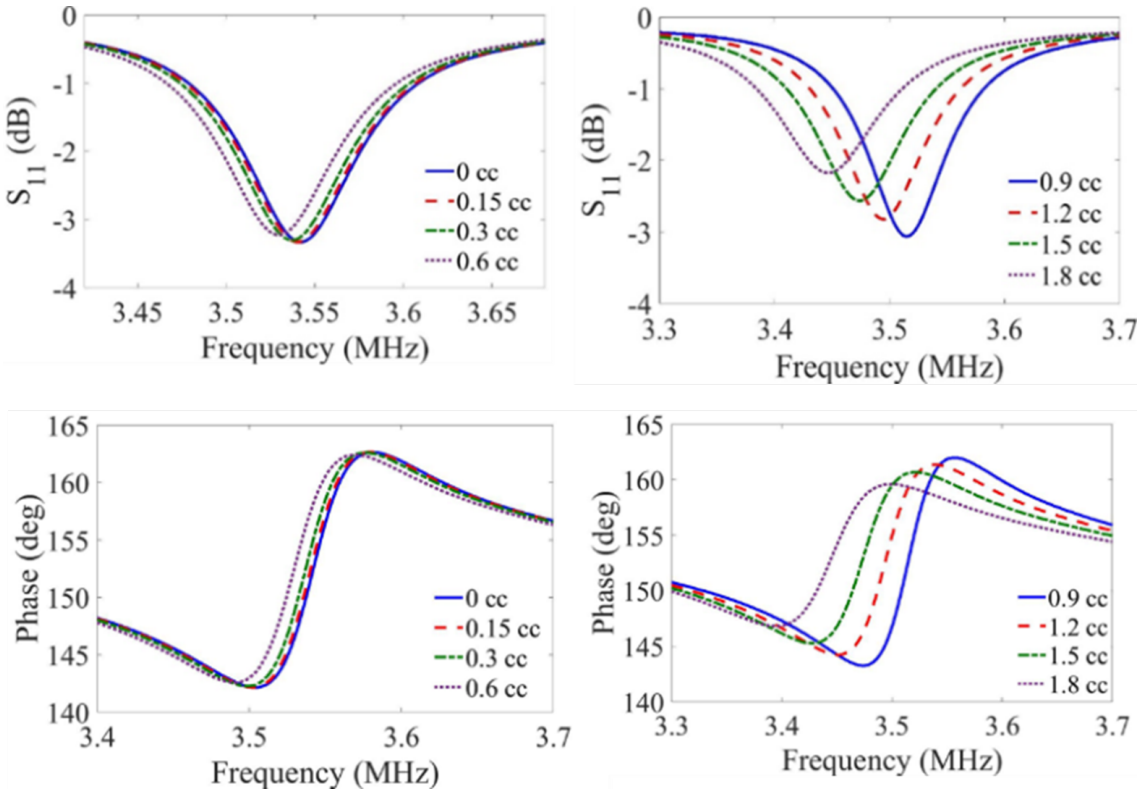

Figure 6.9: Change in S_{11} and phase for different concentrations of methanol vapors for tag 2.

It can be inferred from the graphs that the resonance frequency shifts to a lower value as the volume of methanol vapors increases thereby increasing the effective dielectric constant. Tag 1 has a lower shift in resonance when compared to tag 2 due to lower surface adsorption and absence of capillary condensation since the volatile molecules should permeate through the SU8 coating first. The phase plots show a similar shift to the resonance plots.

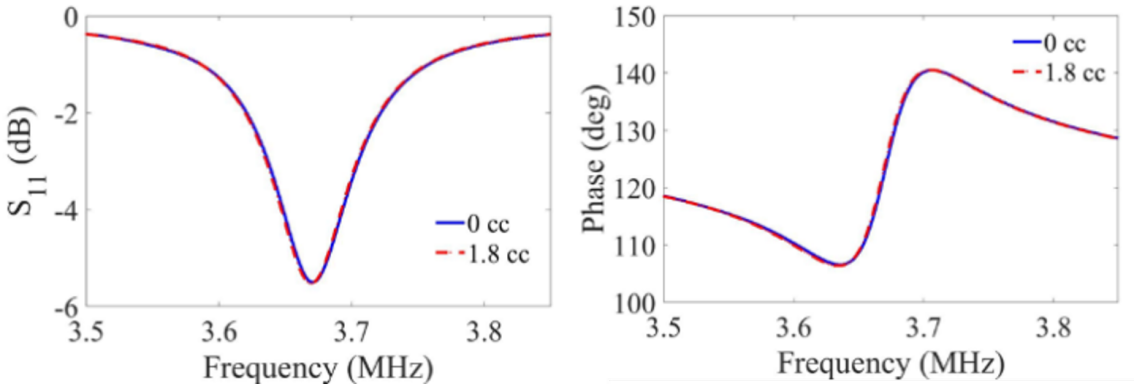

Figure 6.10: Change in S_{11} and phase for different concentrations of isopropyl vapors for tag 1.

6.4.2.2 Iso-propyl Alcohol

The second set of measurements are performed with iso-propyl alcohol vapors. Before starting the measurement cycle, the glass jar was unsealed, blow dried using hot air and resealed to prevent cross contamination. Figure 6.10 and Figure 6.11 shows the change in resonance and phase for different volumes of iso-propylalcohol vapors for tag 1 and tag 2 respectively.

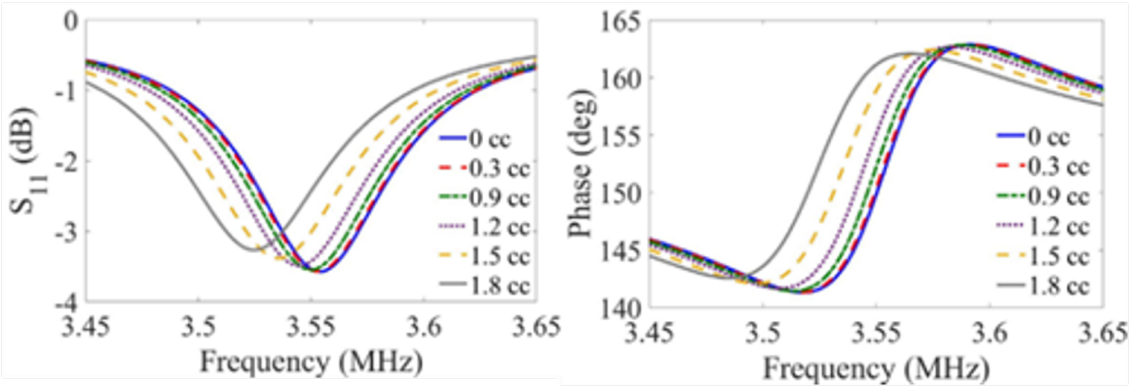

Figure 6.11: Change in S_{11} and phase for different concentrations of isopropyl vapors for tag 2.

It can be inferred from the graph that the SU8 coating on tag 1 did not allow the isopropyl alcohol to permeate through it thereby showing no frequency shift between 0 and 1.8 cc of volatile volume. SU8 is selective in allowing volatiles to permeate through it and this property can be used for enhancing specificity. The resonance frequency shifts to a lower frequency as the effective dielectric constant increases as expected for tag 2. The shift in frequency, when compared to methanol is lower due to lower dielectric constant than methanol.

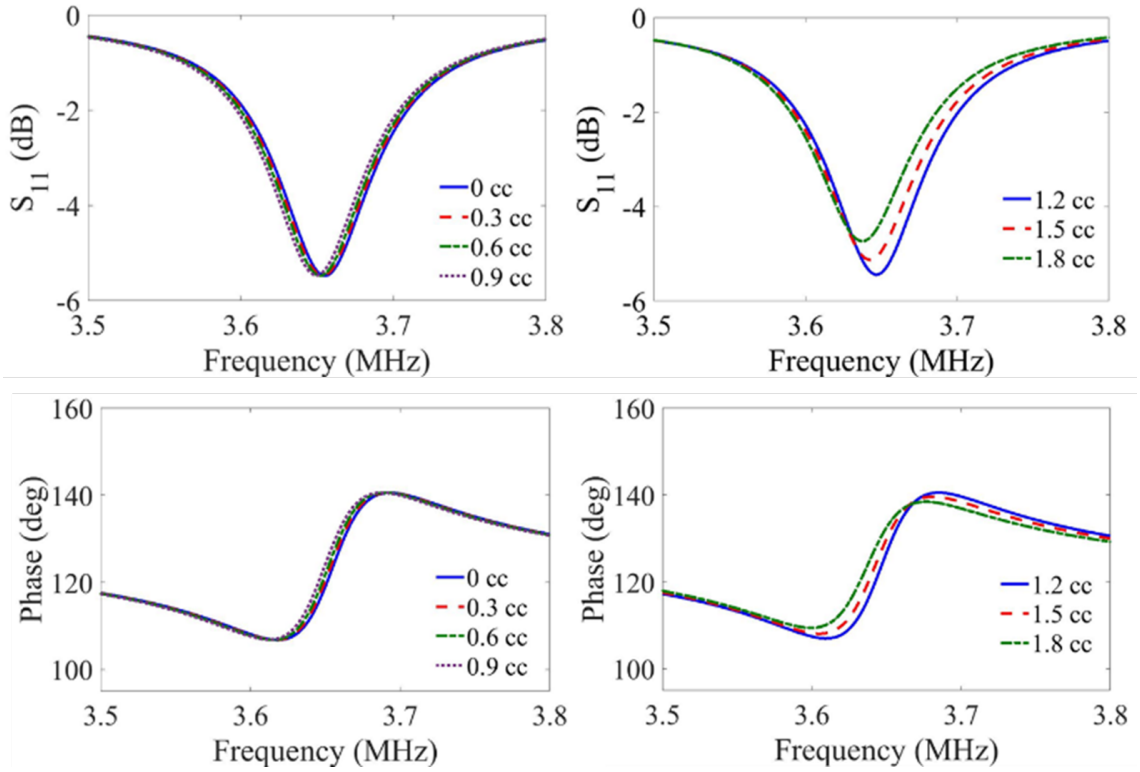

Figure 6.12: Change in S_{11} and phase for different concentrations of acetone vapors for tag 1.

6.4.2.3 Acetone

The third set of measurements are performed with acetone vapors to understand the frequency shift dynamics of both the tags. Figure 6.12 and Figure 6.13 shows the change in resonance frequency and phase for different concentration of acetone vapors for tag 1 and tag 2 respectively.

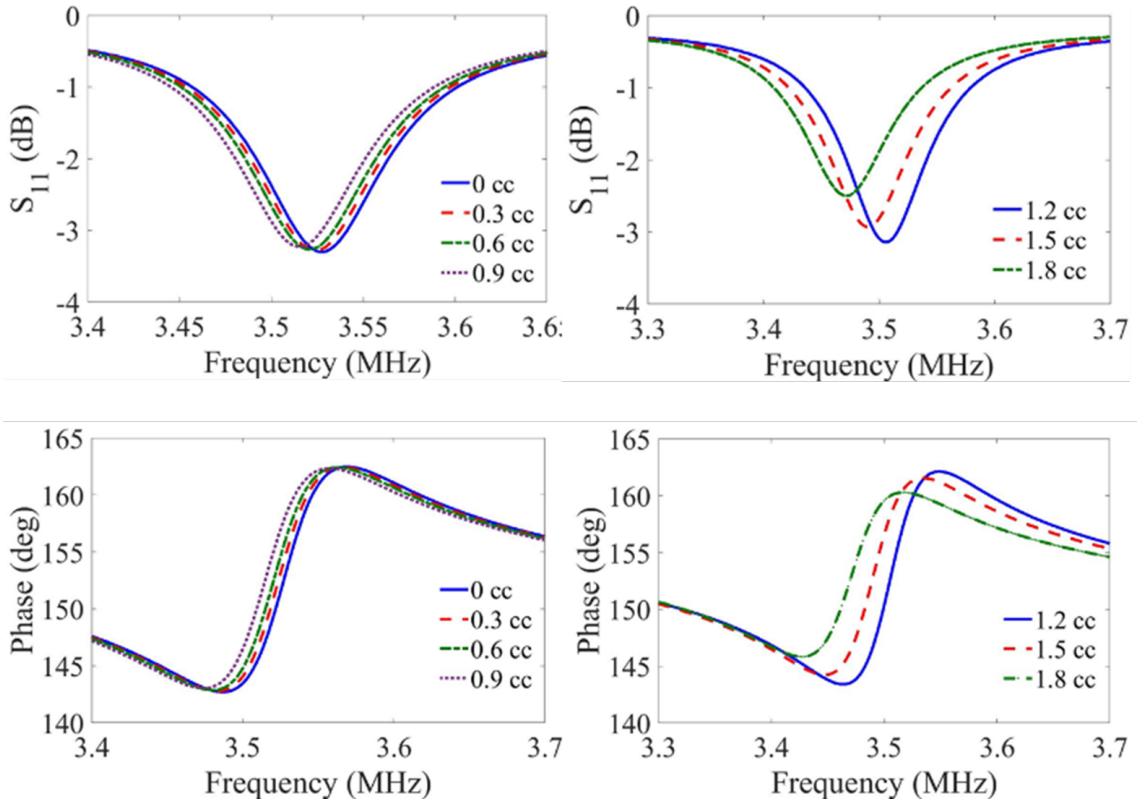

Figure 6.13: Change in S_{11} and phase for different concentrations of acetone vapors for tag 2.

It can be inferred from the graph that acetone vapors permeate through the SU8 layer better than iso-propyl alcohol but not as good as methanol. As expected, the frequency shifted to a lower value as the effective dielectric constant increased.

6.4.3 S1813 coated tags

The second set of experiments are performed to analyze the sensitivity of the tag coated with negative photoresist S1813.

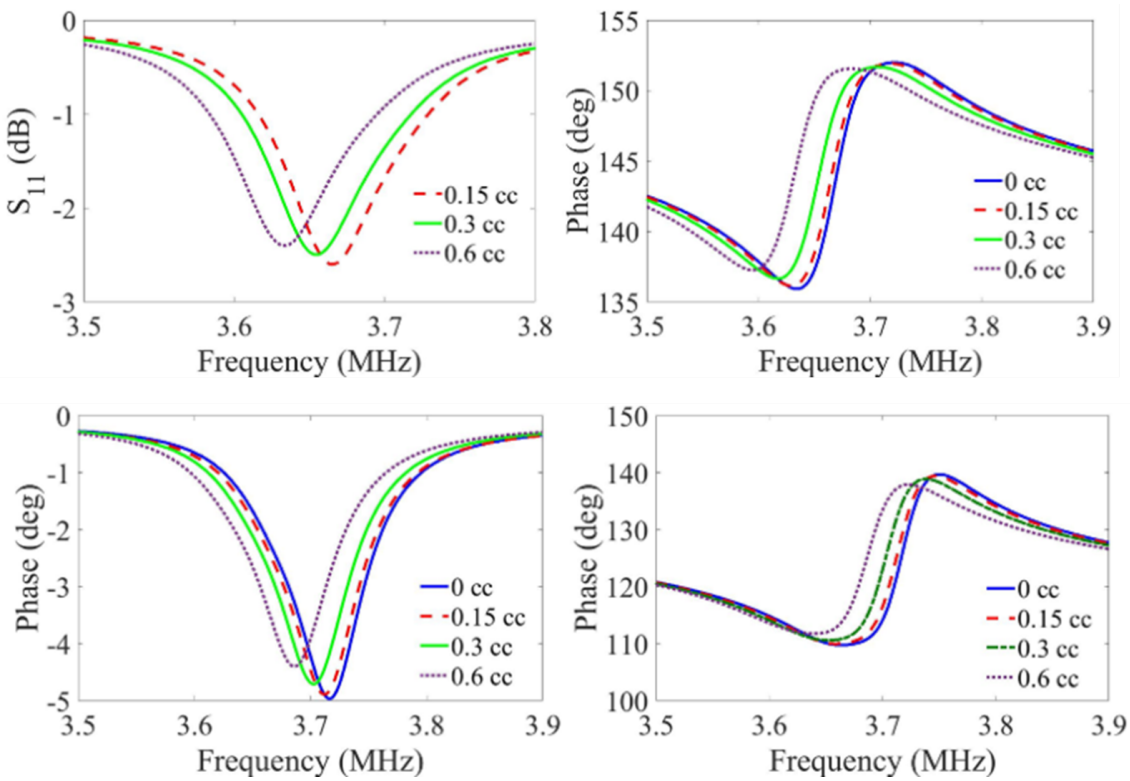

Figure 6.14: Change in S_{11} and phase for different concentrations of methanol vapors for tag 1 (top) and tag 2 (bottom).

6.4.3.1 Methanol

A set of measurements are performed with methanol vapors to evaluate the sensitivity of the tag coated with S1813 photoresist. Figure 6.14 shows the change in resonance frequency and phase for different volumes of methanol vapors for tag 1 and tag 2 respectively.

It can be inferred from the plots that the resonance frequency shift for tag 1 is greater than tag 2. This shows that the photoresist S1813 has a higher affinity towards methanol and enables higher permeation rate and increased adsorption onto the substrate. The combination of high permeability rate, surface adsorption and capillary condensation enables higher sensitivity in comparison to sensor coated with SU8.

6.4.4 Gas tag

The PANi coated interdigitated sensor is placed inside a glass jar (5L) and sealed air tight using clay for measurement. To estimate the amount of Ammonia present in a single drop of aqueous solution, a colorimeteric test is performed using a commercially available API Ammonia test kit. Based on the test results, the aqueous Ammonia solution contained 0.5 mg/L or 0.5 ppm of Ammonia. Based on this, the quantity of Ammonia in a single drop is estimated to be $\sim$3 mg/L or 3 ppm. This sets the lower bound for the detection limit of Ammonia using the current set-up.

For evaluating the sensitivity, three sets of experiments are performed and the values are averaged out. Different concentration of aqueous Ammonia is introduced into the chamber at regular time interval and data is recorded. The evaporated Ammonia vapors are absorbed by PANi as well as adsorbed onto the surface of the sensor which changes the effective capacitance and inturn the resonance frequency. Figure 6.15 and Figure 6.16 shows the change in resonance frequency and phase for different Ammonia concentration respectively.

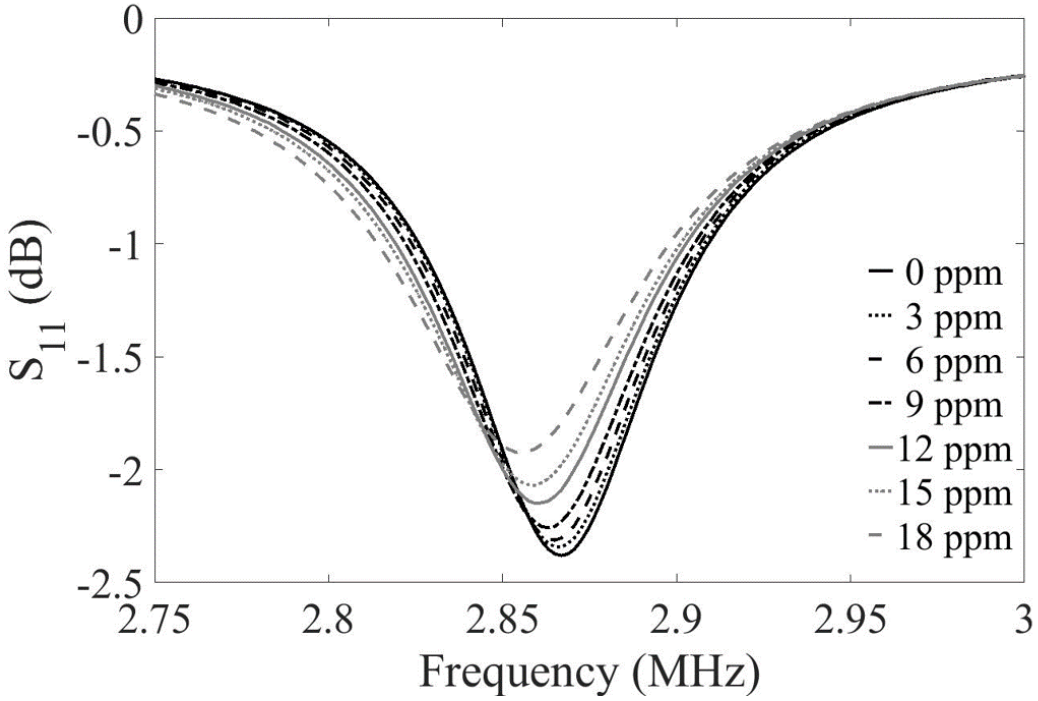

Figure 6.15: Change in resonance frequency (unloaded as reference) of the LC tank for different Ammonia concentration.

It can be inferred from the graph that increase in Ammonia concentration increases the conductivity of the PANi film leading to a decrease in the Q-factor and the effective dielectric constant increases leading to a downward shift in the resonance frequency as expected. Figure 6.17 shows the change in the capacitance as a function of ammonia concentration with unloaded resonance as a reference for three different trials.

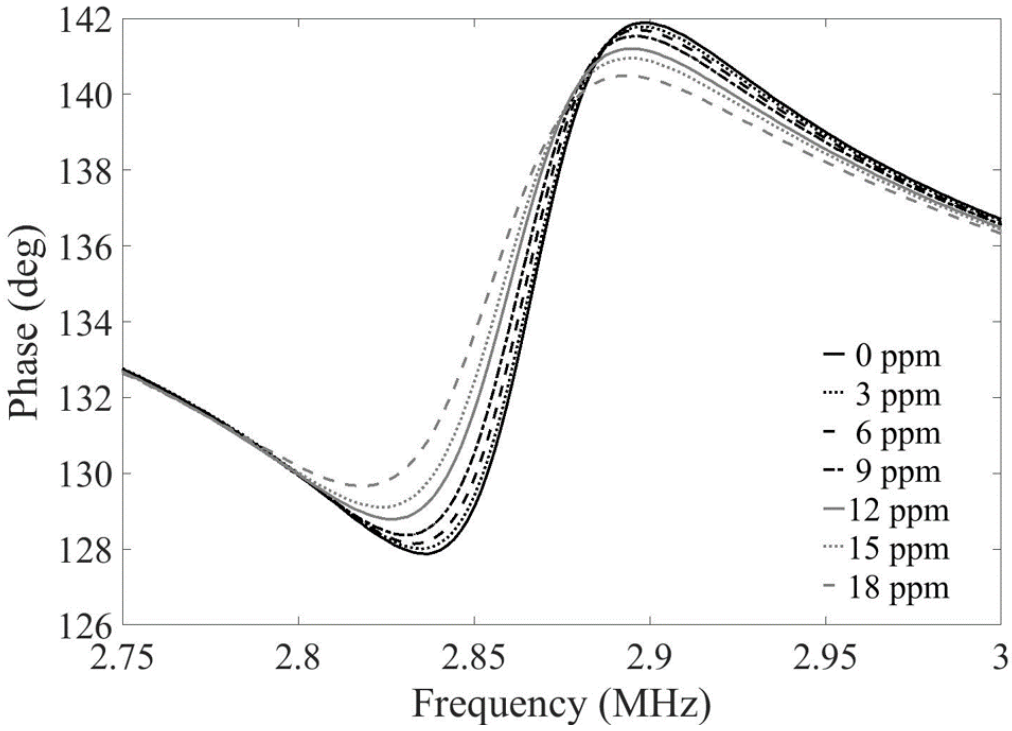

Figure 6.16: Change in phase (unloaded as reference) of the LC tank for different Ammonia concentration.

6.5 Summary

In this chapter, three different thin-film coatings are investigated for improving sensitivity and selectivity of the LC tank for volatile and gas profiling. Three different methods absorption (permeation), adsorption, and capillary condensation are investigated. The change in frequency for different volatile concentration depends on the size of the molecule, affinity towards the thin-film layer and the dielectric constant. The thin-film can be tailored to absorb certain volatiles enabling specificity along with sensitivity. The flexible nature of the tags enables easier integration with current food packaging technology for monitoring food quality along the supply chain. Several tags can be arranged in an array format with volatile specific coatings for identifying multiple vapors at room temperature. In the next chapter,

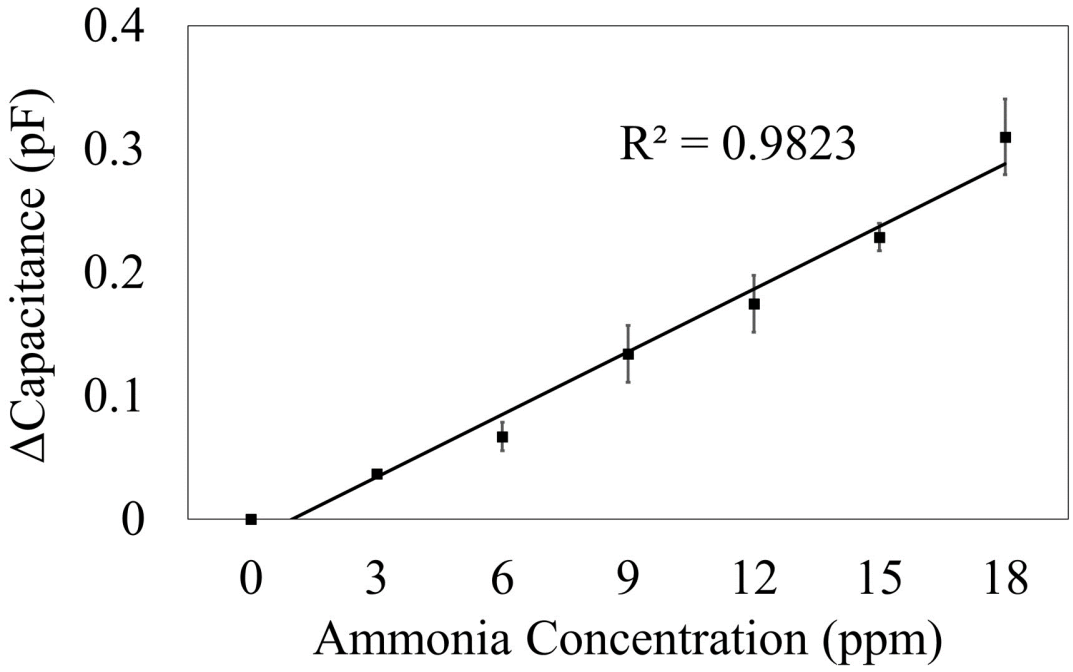

Figure 6.17: Change in capacitance for different concentration of Ammonia taking unloaded resonance as a reference (linear fit).

the sensor will be made compatible with existing UHF RFID and modified such that the analog information can be digitized and transmitted along with the identification information. Nevertheless, the low-cost, real-time, non-contact nature of the tag allows monitoring quality of packaged food items across the supply chain and such tags serves as a first line of defense against food contamination or spoilage.

Chapter 7

Sensor Integrated Modified RFID tag

7.1 Introduction

The previous chapters introduces different type of short range sensors that are compatible with existing RFID infrastructure but are not integrated as part of it. These sensors are a good candidate for wireless near field sensing but they are limited by read range and functionality. The best approach for increasing read range of the sensor is to employ long-range RFID tags for ease of monitoring packaged food across the supply chain. Typically, RFID tags are passive in nature and provide just the traceability information and does not provide any additional quality information. An RFID tag which can perform sensing and traceability simultaneously is required to enhance visibility across the supply chain. Sensor integrated RFIDs are typically battery powered [115] making the tag active and bulky. The requirement of battery increases the overall cost of the tag and cannot be compatible with roll-to-roll printing technique. Furthermore, active tags are not best suited for individual package monitoring due to their short life time and high maintenance cost. Typically, battery powered RFID tags are not desired for low cost large scale enhancement of visibility across the supply chain.

In order to overcome these challenges, passive tags with sensing capability are always preferred which has a theoretical "infinite" life time and can be manufactured using a low cost process. Additionally, low power modulation circuitry with energy harvesting capability

which harvests power from the reader signal for powering up the tag can be incorporated as part of the RFID integrated chip that allows multiple sensor integration on a single RFID tag. Sensor data can be converted into digital bits and transmitted along with the identification information, it can be transmitted to the cloud in real-time through a hand-held reader. In this chapter, a low power passive digital modulation circuitry with energy harvesting capability coupled to an Ammonia sensor is demonstrated as an RFID integrated tag.

7.2 Design and Fabrication

7.2.1 Sensing Element

The element chosen is an interdigitated capacitor fabricated on a flexible Rogers XT/Duroid 8000 high frequency laminates with a dielectric constant of 3.2 (ϵ_r) and a loss tangent of 0.0035 ($tan\delta$) with ten pair of fingers. The width of the fingers and the spacing between them is fixed to be 250 μm. A thin-film of PANi is coated over the interdigitated sensor. For this purpose, PANi in emeraldine salt form is mixed with a solvent 1-Methyl-2-Pyrrolidone in 1:100 ratio by weight. A 30 min of sonification allows proper mixing of the salt in the solvent. The mixture is spin coated on the interdigitated sensor at 100 rpm for a minute and this is followed by a baking step of 120^o C for 30 min. Spin coating followed by baking is repeated four times to obtain a near uniform coating of PANi over the sensor surface. Figure 7.1 shows the schematic of the sensing element and the image of it before and after PANi coating along with dimensions.

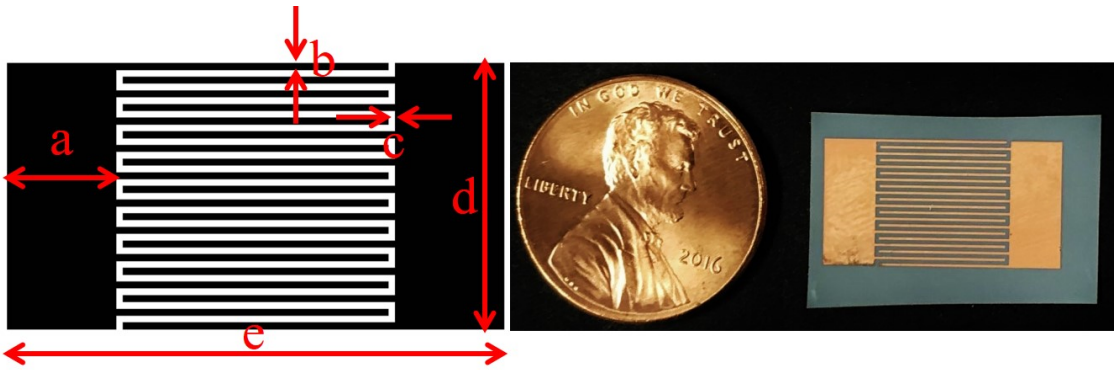

Parameter	a	b	c	d	e
Dimensions (mm)	4	0.25	0.25	9.75	18.25

Figure 7.1: Schematic of the interdigitated capacitor (top left), image of the interdigitated capacitor (top right) and its dimensions (bottom).

7.2.2 Wireless Long Range Approach

The long range sensor tag consists of an antenna, a low power digital modulation unit with energy harvesting capability, and the sensing element coated with PANi.

7.2.2.1 Antenna

A meandered dipole antenna design operating at a wide band across 890-940 MHz (UHF RFID band) is chosen for this purpose. Roger's 4350B high frequency laminates with dielectric constant (ϵ_r) of 3.66 and loss tangent ($tan\delta$) of 0.0037 is chosen for fabricating the antenna. The image of the antenna along with the dimensions and the measured and simulated reflection coefficients are shown in Figure 7.2.

7.2.2.2 Digital Modulation circuit

The digital modulation circuit consists of two parts, an RF front end with the antenna for energy harvesting and a digital backend with a microcontroller and an analog to digital

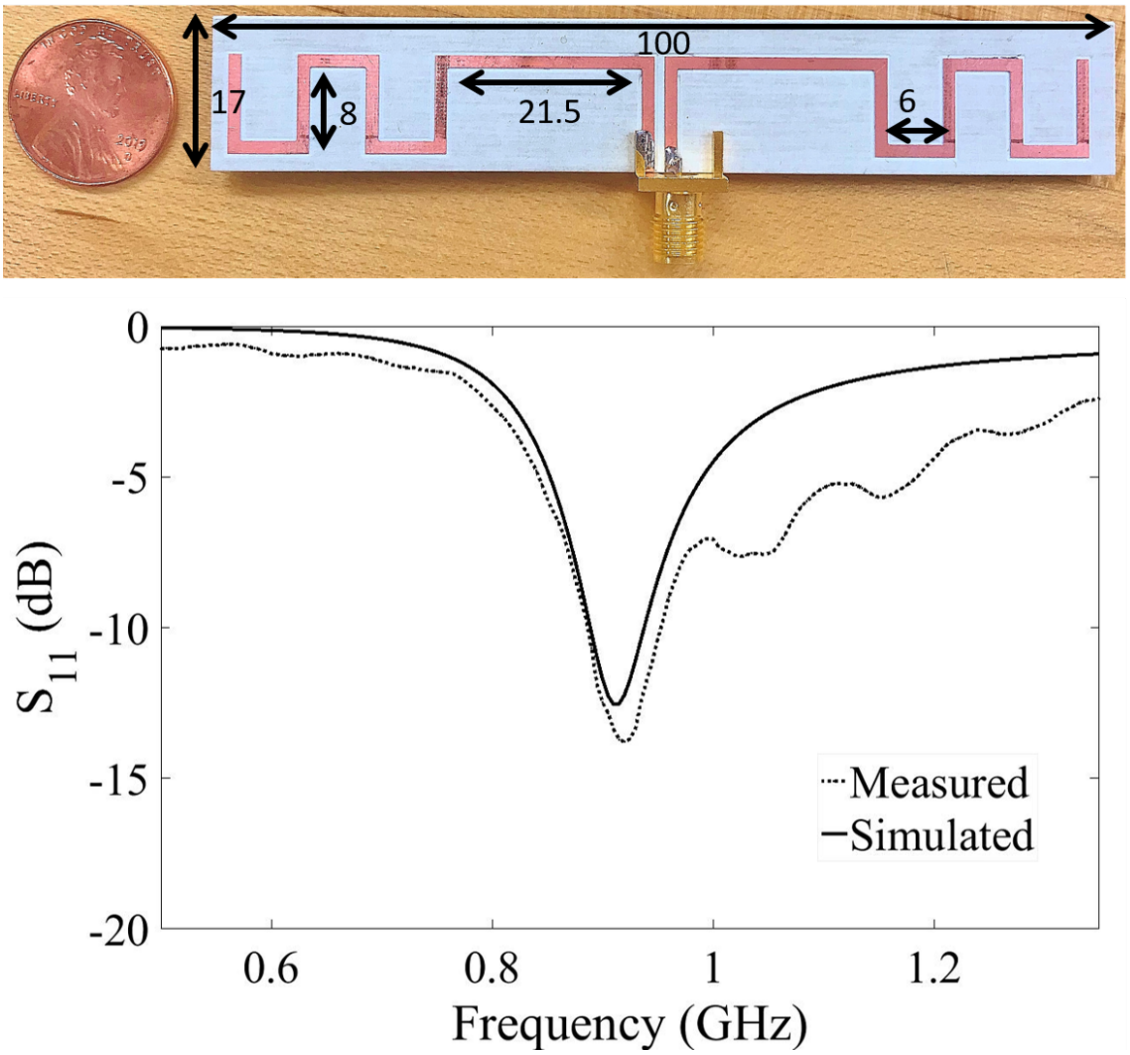

Figure 7.2: Image of the antenna with dimensions (in mm) (top), Simulated and measured reflection co-efficients (bottom).

convertor (ADC) for transmitting the digital bit sequence. The circuit diagram for the long range tag is shown in Figure 7.3 and the image of the circuit is shown in Figure 7.4. The modulation circuit with the energy harvester is adapted from [28].

The long range set-up works at 900 MHz frequency. The RF power from the interrogator is received by the antenna and is fed into the 6-stage Dickson charge pump rectifier circuit for energy harvesting. A matching circuit is designed with L_M = 6.8 nH and C_M= 8 pF in

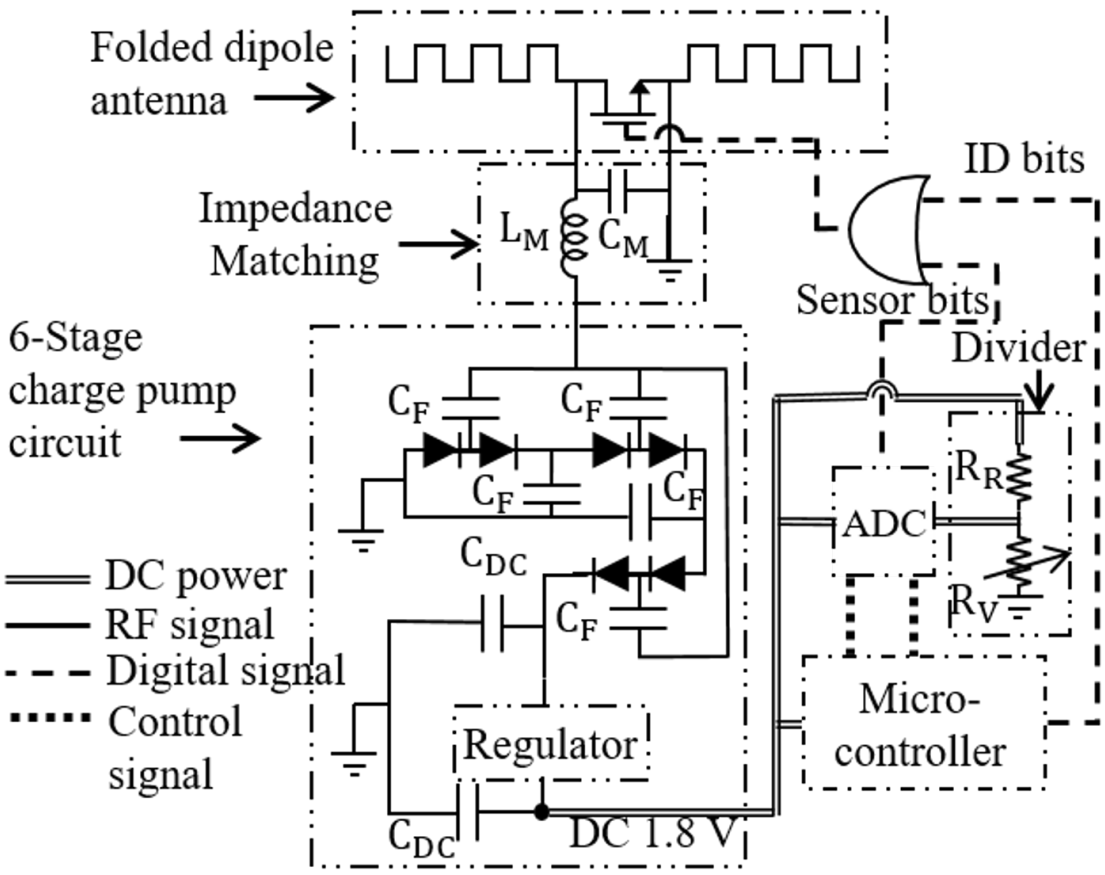

Figure 7.3: Circuit diagram for the low power digital modulation circuit with energy harvesting coupled to the PANi coated sensor.

between the antenna and rectifier to maximize power conversion. The charge pump circuit consists of six low barrier Schottky diodes HSMS 2852 for converting the RF energy into DC voltage for driving the digital circuit and the sensor. Further details of the charge pump can be found in our previous work [28]. The DC voltage generated from the rectifier is fed into a low power Voltage regulator (TPS79730) from Texas Instruments to cap the voltage at 1.8 V for driving the digital circuitry. Two 1 μF capacitors (C_{DC}) at the input and output of the regulator aids in stabilizing the DC voltage. PIC12LF1822 micro controller is programmed to generate the ID bits as well as the control signal to activate the 8-bit ADC ADS7040. The voltage range of the ADC is from 0 to 1.8 V. The ADC converts the voltage data generated

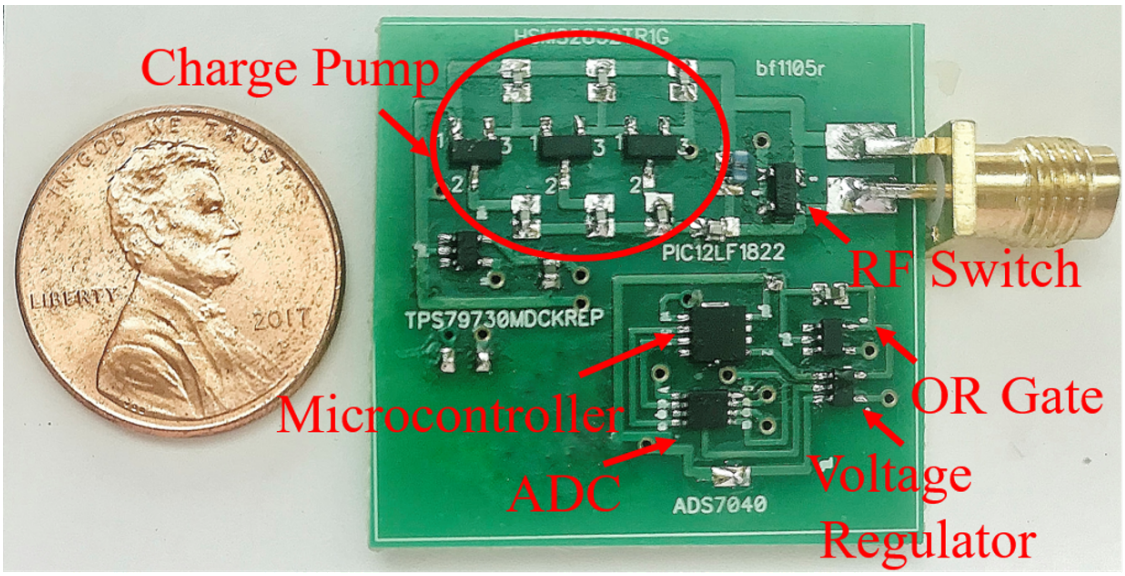

Figure 7.4: Image of the low power digital modulation circuit with energy harvesting.

from the Ammonia sensor to digital bits. The ID and sensor bits are combined using an OR gate (SN74AUP1G32) and is fed to a high frequency switch (BF1105R) to modulate the antenna impedance based on the bit stream generated for transmission. The sensor circuitry consists of a resistor divider with a fixed reference resistance R_R of 100 MΩ and a variable resistance R_V representing the resistivity of the interdigitated sensor. A 100 MΩ resistor is connected in parallel to the PANi coated interdigitated sensor and the equivalent resistance R_V changes with change in Ammonia concentration. The received modulated signal is demodulated at the interrogator to obtain the sensor information.

7.2.2.3 Interrogator Set-up

For the long range configuration, the digital data is demodulated using a read-out circuitry at the RF interrogator similar to the one in [28]. The interrogator activates the sensor tag wirelessly and receives the identification as well as sensor information bits. The measurement

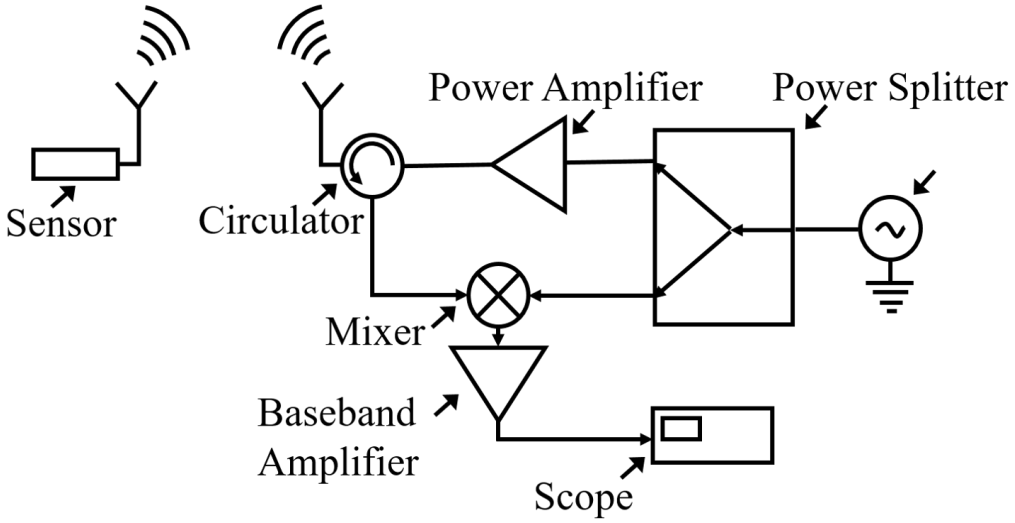

Figure 7.5: Schematic of the interrogator set-up for wireless long range configuration.

set-up consists of an RF source to generate a continuous RF signal at 900 MHz which is fed into a power splitter which splits the power into two equal branches. One branch is fed to a power amplifier, amplified and transmitted through a transmitting antenna via a circulator. The other branch is fed into a mixer for demodulation. The return signal from the tag is received by the antenna and is fed into the mixer through the circulator. The return signal mixes with the transmitting signal for demodulation of digital data. The low power demodulated signal is amplified using a base band amplifier with a 26 dB gain and a cut-off frequency of 150 kHz. The amplified signal is fed into the oscilloscope to obtain the sensor data. The schematic of the interrogator circuitry is shown in Figure 7.5.

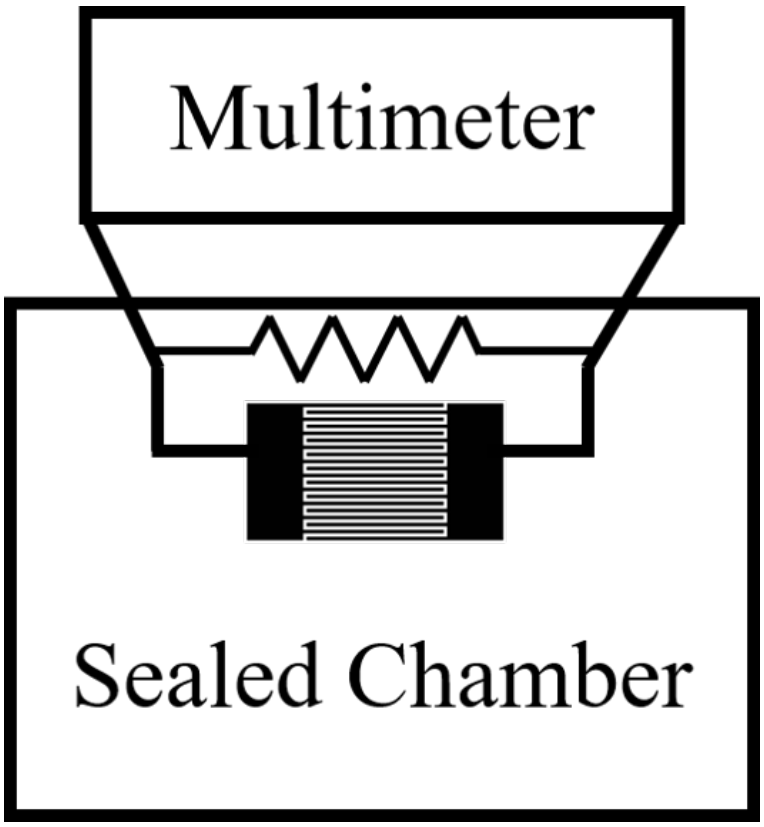

Figure 7.6: Schematic of the direct probing measurement set-up.

7.3 Sensor Element Evaluation

7.3.1 Direct Probing

For evaluating the sensing element using the direct probing technique, two wires are soldered onto the pads of the sensing element with a 100 MΩ resistor in parallel and is connected to the Keysight digital multi meter (34401A) for measurement. The resistance across the sensing element is measured as a function of number of drops as shown in Figure 7.6.

Three sets of experiment are performed to determine the relationship between concentration of Ammonia and resistance change across the interdigitated sensor. Similar to first technique, Ammonia is introduced in drops with a fixed time interval of 30 min. The resis-

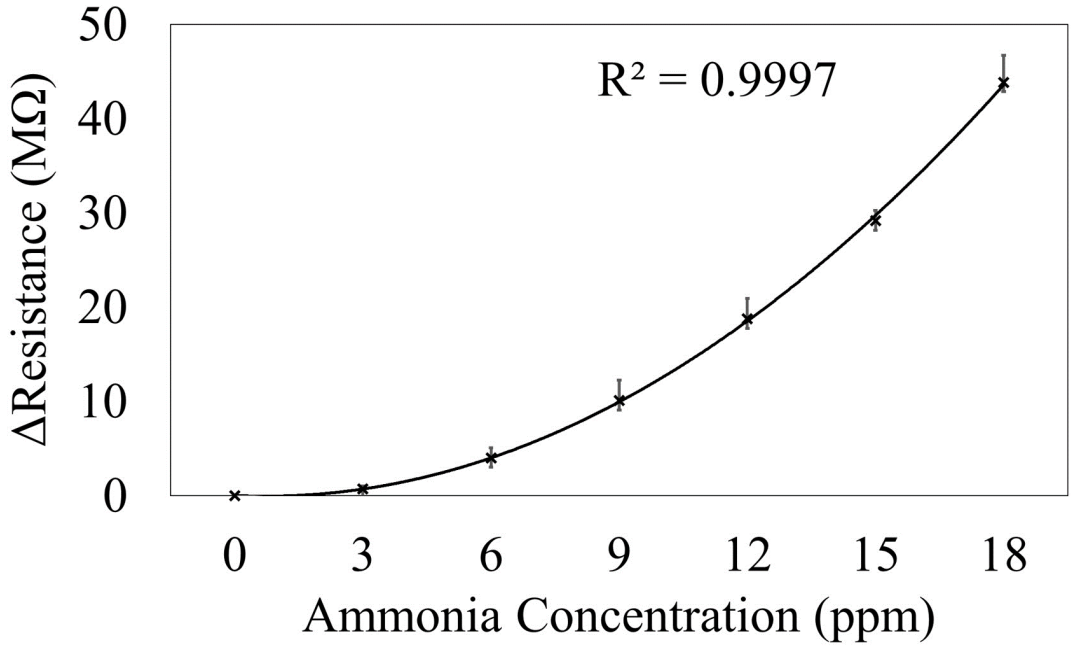

Figure 7.7: Change in resistance (unloaded as reference) across the sensing element for different Ammonia concentration (polynomial fit: n =2).

tivity is measured and the values are averaged out as shown in Figure 7.7.

From Figure 7.7, it can be inferred that the resistance decreases with increase in concentration of Ammonia as expected. The two different interrogation techniques provided further insight regarding the sensitivity of the sensor element. For both the techniques, the sensing element is able to detect a very small amount of Ammonia in the chamber setting the sensitvity to be 3 ppm. From Figure 7.7 and Figure 7.6, it is clearly inferred that the repeatability factor for change in resistance is higher than that of change in capacitance. Hence, the change in resistance technique is chosen for digitization and evaluation in the wireless long range setup.

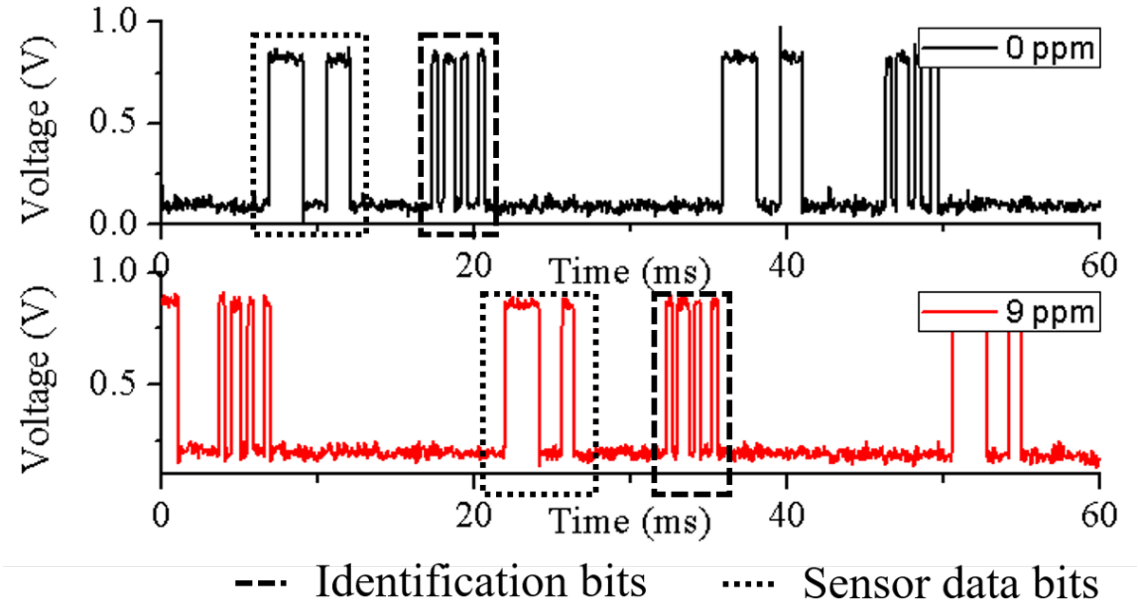

Figure 7.8: Digital response (ID and sensor data) of the sensor tag for two different Ammonia concentrations.

7.3.2 Wireless Long range

The wireless long range set-up is evaluated and the digital data bits are recorded in the scope. The interrogator is placed 45 cm from the sensor tag and operates at 900 MHz with a power of 15 dBm. As the Ammonia concentration increases inside the chamber, the resistance decreases which in turn changes the voltage across the resistor divider circuit. Based on the divider voltage, the ADC converts the analog data to digital bits for transmission. The ID of the sensor is chosen as '101101001' and along with the digitized voltage information, the data is transmitted back to the interrogator. For showing the proof-of-concept, the complete tag is tested for two different Ammonia concentration (0 & 9 ppm) and the digital bit sequence recorded by the reader is shown in Figure 7.8.

It can be inferred from the Figure 7.8 that the digital sequence '01110011' corresponds to 0 ppm of Ammonia. The voltage generated from the resistor divider is 0.9 V. The digital

sequence '01110010' corresponds to 9 ppm of Ammonia and the voltage generated from the resistor divider is 0.8 V. The senstivity of the long range configuration is limited by two factors, first is the amount of ammonia in 1 drop, and second is the digitization error of the ADC (∼7 mV for 0-1.8 V range). In this case, sensitivity is limited by the concentration of Ammonia in 1 drop (3 ppm). In reality, the data can be acquired in real-time for any concentration change by adapting a proper voltage range for ADC to convert into digital bits.

7.4 Discussion

In this chapter, a battery free digital RFID coupled Ammonia sensor is presented for traceability and quality control of food products across the supply chain. The sensor is real-time in nature and operates at the RFID frequency band allowing the use of existing RFID infrastructure set-up. Although the technique is robust, low cost, and simple to implement, it comes with a number of challenges and these are discussed in the next section.

7.4.1 Miniaturization

A few key challenges should be overcome in near future to adapt this tag as a part of the existing packaging infrastructure. In the current set-up, the low power digital modulation and energy harvesting circuitry is not optimally miniaturized and occupies more space. This can be avoided by packaging the circuit into a single integrated chip similar to the RFID IC in order to make it practical and adaptable to food packages. There is a lack in commercial availability of passive RFID IC's which has both identification and sensing capability. The first step to advance this technology is to develop an integrated chip that can perform both

the functions simultaneously similar to the digital circuitry presented in this paper. Furthermore, a single IC with the above-mentioned functionality will make it easier to adapt the sensor tag as part of mass commercialization techniques such as roll-to-roll manufacturing. Another potential challenge is to fabricate the complete set-up on a flexible packaging compatible substrate. Once a single IC for sensing and identification becomes a reality, this challenge can be easily overcome.

7.4.2 Sensitivity

In terms of improving the sensitivity of the sensor tag, the field strength of the fringing fields across the interdigitated tag should be improved. This can be performed by increasing the number of fingers and decreasing the finger width of the interdigitated capacitor. Small feature size are possible in traditional photolithography, but typically, RFID tags are screen printed and the minimum feature size is limited by the print resolution. Another challenge is to obtain a uniform layer deposition of PANi over the sensor substrate. This can be achieved by further optimizing the mixing ratio of the salt and the solvent as well as the spin speed, curing time, and temperature. A dip coating technology will makes it further advantageous for mass commercialization than the current spin coating technology. Furthermore, a combination of different sensing techniques such as capillary condensation, adsoprtion and absorption can be investigated and incorporated to further enhance the sensitivity of the sensor tag.

7.4.3 Read range

Typical challenge in current RFID systems is to improve the read range and the clutter rejection. In terms of read range, there exists a trade-off in antenna design between improved read range and miniaturization. In this work, the read range is limited to 45 cm and can be improved by further reducing the power consumed for the digital modulation. Adapting a single chip to perform both the operations (ID + Sensor) will reduce power consumption and improve the read range. For most applications, a miniaturized antenna is always desired but this comes with a trade-off that limits the gain of the antenna and in turn the read range. One possible alternative solution to overcome both these challenges is to use multiple frequencies for operation. The concept of harmonic RFID with one frequency band for down link and another frequency band for up link will improve clutter rejection [117] as well as read range as demonstrated in [118, 119].

7.4.4 Data Analysis & Security

For a real-time system, a potential challenge is to handle the enormous amount of data collected over time to characterize the quality of product. One solution is to increase the on-board memory of the RFID IC, but this can be potentially altered or physically damaged making the quality control system less secure. The ability of the system to communicate with the cloud and transfer the data to a remote server makes it practical and easier to securely verify the product quality. One such technique is to use blockchain inspired RFID for product authentication and data logging as presented in [120]. In order to manage large data, instead of monitoring continuously, a technique to trigger the sensor when the quality deteriorates below a certain threshold can be considered. Smart scheduling algorithms for

reading multiple sensor tags can also be considered to improve efficiency as well as to use lower resources.

7.5 Summary

In this chapter, a battery free digital Ammonia sensor is presented using a complete passive long range sensor tag. An interdigitated capacitor coated with PANi is chosen as the sensing element and is capable of detecting a small volume (3 ppm) of Ammonia at room temperature and atmospheric pressure. The change in resistivity across the sensing element is monitored for different Ammonia concentration. A passive sensor tag with a low power energy harvesting and digital modulation circuit is designed to obtain a read range of 45 cm. The tag harvests energy from the source, digitizes the sensing data and re-transmit the signal with both the sensing as well as identification information as digital bits. The proposed sensor can be easily adapted to existing RFID infrastructure and can be used for monitoring quality of food items such as fish. In the future, the low power modulation circuitry can be made into a single integrated chip similar to the RFID IC which allows mass commercialization using conventional roll-to-roll manufacturing techniques. This tag aids in identifying and quickly removing bottlenecks across the supply chain and provides a low cost solution for food quality monitoring.

Chapter 8

Conclusion

In this dissertation, a number of sensing elements and interrogation techniques are developed that can be adapted to existing supply chain tracking infrastructure. The different sensing modalities developed in this dissertation allows monitoring a variety of target parameters that ensures highest quality food reaching the fork. These techniques help in achieving the goal of the envisoned modified supply chain shown in Figure 1.3 using a modifed RF sensor tag as shown in Figure 1.4.

8.1 Summary

In Chapter 2, a simple, inexpensive, and reusable hybrid sensor is proposed for real time liquid sample measurements. The hybrid nature of the sensor allows simultaneous measurement of two properties, dielectric constant and viscosity, by tracking the electrical and mechanical resonant frequencies. The natural resonance of the sensor is affected by the viscosity of the liquid food and the resonance due to the formation of the LC tank is affected by the dielectric constant of the liquid food. Both the resonances are read out using a single reader coil forming a wirless short range system. The proposed sensors are evaluated for determining the adulteration levels in extra virgin olive oil. The detection of 10% adulteration by the smart vial is low enough for most practical applications and this sensor can be readily used for quantification of commercial extra virgin olive oil along the supply chain.

In Chapter 3, a sensing approach that utilizes 3D printed RF sensors coupled to a microfludic channel for liquid profiling is developed for food quality control. Two different resonators are presented, a 3D printed cavity and a 3D printed split ring resonator. Both the resonators use a microfludic channel through which the target liquid is introduced for identification (350 μl for cavity and 10 μl for split ring resonator). The sensors are capable of detecting the change in dielectric constant of the liquid as it moves along the supply chain. A path is shown in which such 3D printed sensors can be coupled to an antenna for wireless transmission of sensing data by demonstrating a 3D printed UHF RFID tag. These sensors are low cost and utilizing the advantages of 3D printing, different perturbation geometries or shapes of microfluidic channels can be easily designed targeting specific ranges of dielectric constant for liquid under test.

In Chapter 4, an interdisciplinary approach for detecting bacterial count in liquid food matrices using RF sensors is developed for contamination detection. The proposed wireless biosensor design is capable of detecting a threshold of 5 log CFU/ml bacteria with minimum handling steps. The antibody-free detection technique exploits the ability of bacteria to form biofilms. Attached cells coupled with conductive nanoparticles allow RF interrogation. The sensor shows good sensitivity and reproducibility. The non-contact and wireless nature of the sensor, if adapted to existing RFID infrastructure, provides an opportunity to monitor real-time the quality of milk through the supply chain using a simple RFID hand-held reader. The sensor design is non-selective across a broad spectrum of pathogens within liquid food or water, and thus low-cost selfcontained sensor kits are envisioned for quality control and safety.

In Chapter 5, a new sensing approach that uses capillary condensation phenomenon on a porous substrate for detection of food volatiles is developed for spoilage detection.

A wireless interdigitated LC resonant tank fabricated on a flexible and porous substrate is demonstrated for sensing VOCs using dielectric loading through capillary condensation. The resonance frequency of the LC tank is read out using an external pick up coil and it changes with change in the volume and type of condensate in the pores. The sensor is demonstrated to have high sensitivity and can detect a very small volume (0.15 cc) of volatiles in air. Since the tags are flexible, these can be mounted onto food packaging for detecting volatiles to determine the freshness and quality in food supply chain.

In Chapter 6, a sensing approach that uses absorption of food volatile molecules and gases onto different thin film coating with improved specificity is develeoped for spoilage detection. Three different thin-film coatings are investigated for improving sensitivity and selectivity of the LC tank. Three different methods absorption (permeation), adsorption, and capillary condensation are investigated. The change in frequency for different volatile concentration depends on the size of the molecule, affinity towards the thin-film layer and the dielectric constant. Two sensing approaches are presented; volatile sensor, and gas sensor. For the first approach, thin film of two different photoresists are coated onto the sensing element; SU8 and S1813 and evaluated for enhancing or selectively blocking certain food volatiles. For the second approach, a thin film of conductive polymer which has a very high affinity towards Ammonia is coated onto the sensing element and evaluated for sensitivity and specificity. The sensor is capable of detecting 3 ppm of Ammonia under room temperature and atmospheric pressure.

In Chapter 7, a sensor integrated RFID tag is developed that is compatible with existing RFID infrastructure for detecting Ammonia gas concentration in packaged food. An interdigitated capacitor coated with PANi is chosen as the sensing element and is capable of detecting a small volume (3 ppm) of Ammonia at room temperature and atmospheric

pressure. A passive sensor tag with a low power energy harvesting and digital modulation circuit as shown in [28] is designed to obtain a read range of 45 cm. The tag harvests energy from the source, digitizes the sensing data and re-transmit the signal with both the sensing as well as identification information as digital bits. The sensor tag along with the digital circuitry is evaluated for detection of Ammonia gas which is a spoilage marker for fish.

In summary, the sensor tag developed in Chapter 7 is capable of converting the analog data of the different sensing elements developed in the previous chapters to digital bits showing a path forward to integrate multiple sensors using a single passive tag to enhance visibility of the supply chain. The sensing methodologies and sensing elements developed in this dissertation aids in advancing the quality control strategies with enhanced sensitivity and specificity to provide a comprehensive passive RF tag that can monitor multiple parameters and transmit digital sensor data as well as identification to the cloud with an improved read range.

8.2 Future Work

The next section discusses the future direction in realizing the envisioned goal of sensor integrated modified RFIDs for real-time quality monitoring across the supply chain using the existing RFID infrastructure.

8.2.1 The Road Map: Future of RFID Sensors

RFID sensors play a pivotal role in enhancing visibility across the supply chain. To realize this, a phenomenal leap is required in terms of technology before the industry could actually adopt it. The sensors presented in this dissertation is a first step towards advancing such

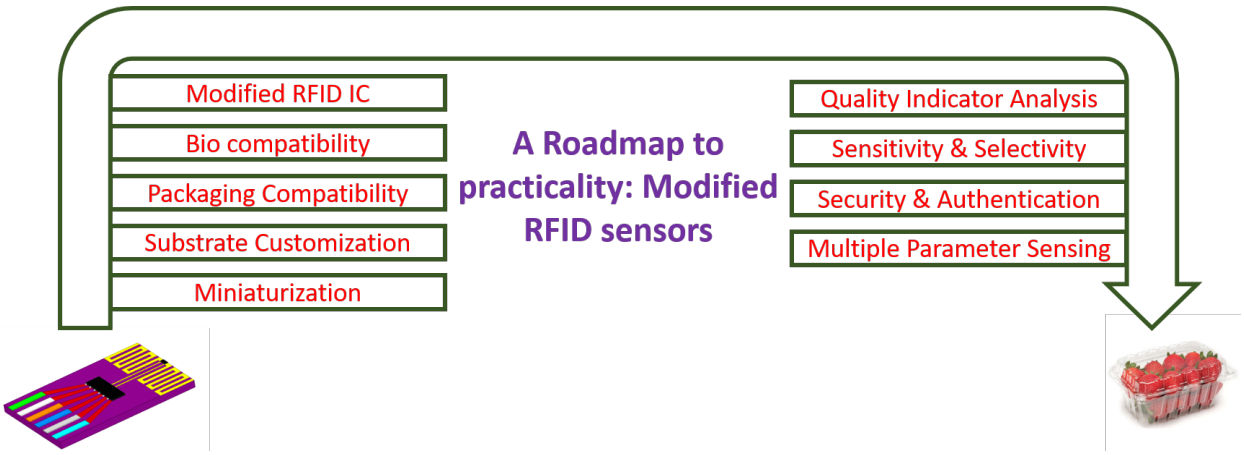

Figure 8.1: A Road Map to Practicality: Modified RFID sensors.

an RFID sensing technology. There are many dimensions that needs to be improved and additional facets added to the integrated sensor developed in Chapter 7 to be made an integral part of the food supply chain as shown in Figure 8.1.

8.2.2 Miniaturization

A key factor that will play a vital role in adapting the sensor tag as part of the food packaging is the size. In the current set-up as shown in Chapter 7, the digital circuitry with the energy harvesting is bulky and occupies more space. This can be avoided by packaging the circuit into a single integrated chip similar to the RFID IC in order to make it practical and adaptable to food packages. There is a lack in commercial availability of passive RFID IC's which has both identification and sensing capability. The first step to advance this technology is to develop an integrated chip that can perform both the functions simultaneously and passively similar to the digital circuitry presented in Chapter 7. Furthermore, a single IC with the above-mentioned functionality will make it easier to adapt the sensor tag as part of mass commercialization techniques such as roll-to-roll manufacturing. A future direction

will be to re-design an RFID IC with ultra low power requirement that encompasses the passive digital circuitry along with the energy harvesting capability.

Next, the radiating element should be optimized to improve the read range of the sensor tags which is a key factor for good performance improvement. Typically for long range tags, an antenna is designed at the front end for communication to and from the RFID reader. There is always a trade-off in antenna design between improved read range and miniaturization as the gain of the antenna depends on the size. Furthermore, the read range is also limited by the amount of power consumed by the modified RFID IC. A ultra low power consumption is a key requirement when re-designing the RFID IC. One possible future direction that can overcome both these challenges is to use multiple frequencies for operation [121]. The concept of harmonic RFID with one frequency band for down link and another frequency band for up link with improved clutter rejection will lead to an increased read-range.

8.2.3 Substrate Compatibility

For adapting multiple sensing capabilities to the single tag, an important constraint that should be addressed is the substrate compatibility. Different sensing techniques require customized substrates as majority of the techniques depends on the substrate properties for sensing. Fabricating reliable multi-material substrate is a huge challenge that involves process compatibility, material bonding, and stringent mechanical strength requirements. One future direction will be to design customized substrates through 3D printing. The additive manufacturing technique through 3D printing has improved over the last decades with introduction of printers that are capable of printing multiple materials such as dielectrics, conductors and nanoparticles. A combination of these techniques can be utilized to fab-

ricate customized substrates that are required for perfoming multiple sensing techniques simultaneously.

In specific to volatile sensing, a customized pore size and geometry is required to enhance specificity. To achieve this, investigations should be carried out for determining pore size versus molecular properties. Once the pore size is determined, the substrate should be custom fabricated. One approach is to add conductive nanoparticles in a liquid polymer and suspend them uniformly. Once suspended, the substrate film can be deposited. Utilizing chemical etching, the nanoparticles can be etched leaving behind nano porosity. Another approach is to utilize nanoporous microparticles instead of nanoparticles and suspend them uniformly in a liquid polymer matrix. Once deposited, the nano pores on the surface of the microparticles can be used for sensing.

8.2.4 Packaging Compatibility

The sensors are deployed in food packages which requires them to be fabricated on a packaging compatible flexible substrate. Typically, the food packages are commercialized using roll-to-roll printing techniques. Adapting the knowledge of 3D printing with current roll-to-roll printing will help in improving substrate compatibility for sensors that are made an integral part of the package. One future direction will be to investigate techniques that utilizes the metal coating of the food packages to integrate the RF sensor. Flexible substrate for the sensor is required to enable easier adaptation to different shapes and sizes of the food packages. Typically, a packaging compartment or casing that separates the sensor tag from direct contact will food is required for non-invasive sensing. Another direction will be to investigate different techniques for compartmentalizing the existing food package to integrate the modified RFID sensor.

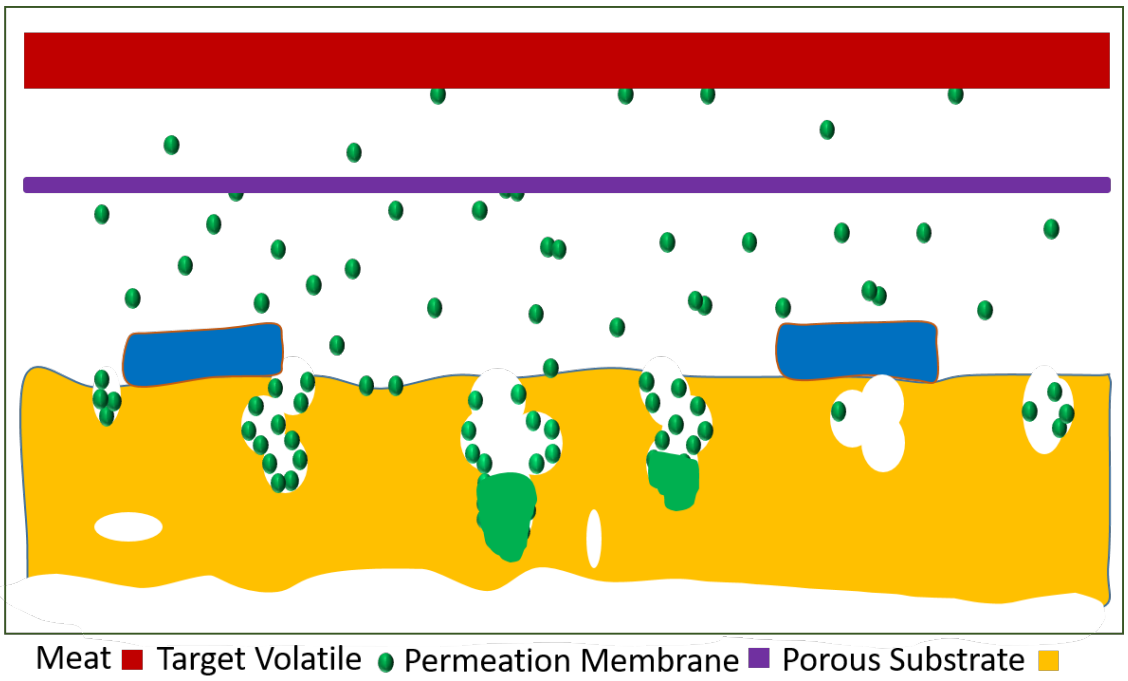

Figure 8.2: Concept of spoilage detection using a bio compatible permeation film.

8.2.4.1 Modified packaging

A change in the existing packaging by introducing additional compartment with a sensor is required for non-invasive sensing. For example, consider detection of spoilage marker such as volatiles in fresh produce such as mushrooms or greens placed in a sealed package. There are two approaches that can be followed, one approach is to use a sensor that has a bio compatible coating on it as explained in next section or to modify the cover of the package to include a compartment sealed with a permeation film that allows volatile permeation in one direction only. As the volatiles enter the permeation film, it gets trapped inside the compartment as shown in Figure reffig:permeate and the sensor continues with the profiling leading to determination of spoilage rate. In [122], a number of food packaging compatible polymers (high density polyethylene, low density polyethylene) are tested for permeation of spoilage markers to enable volatile profiling.

8.2.4.2 Bio Compatible coating

An important aspect of developing food sensors is to fabricate sensor tags on bio compatible materials or to coat it with one to make it part of the existing packaging infrastructure. As mentioned earlier, new packaging techniques should be investigated such as compartmentalized packing to enable integration of modified RFID sensors. An alternative to use the existing packaging infrastructure is to attach the sensor tag on the inner walls of the food package to capture the quality indicators such as volatiles. In order to do so, if compartmentalization is not available, then the sensor should be coated with a bio compatible film or casing. This can allow unintentional contact with food. A number of bio compatible coatings approved by FDA are available in literature [123], a noise analysis should be performed to understand the effect of such coatings on the sensitvity of the modified RFID sensor. Some of the common food packaging materials are

8.2.5 Quality Indicator Analysis: Sensitivity and Selectivity

Food is a complex matrix with multiple indicators that can be tracked for quality control concerns such as adulteration, spoilage or contamination. The sensors are of different types targeting different properties of food and correlate the degradation rate to a quality marker. Repeatability is an important aspect of developing any sensor to eliminate false positives and false negatives. False results render the sensor useless and defeats the sole purpose of incorporating a sensor with the food package. In this aspect, realizing a sensor with improved sensitivity and selectivity is vital towards the success of this envisioned goal of modified RFID sensors. There are number of ways to improve this aspect which will be discussed in the next section and it depends on the parameter being monitored as well as

the nature and type of food.

8.2.5.1 Built-In Reference

To obtain repeatable results, a stable reference is required. The reference can be in built or can be an additional sensing element that does not vary with the change in the monitoring property. This aids in elucidating the change in the quality marker independent of other external factors such as temperature, humidity and environmental variations. The challenge is to utilize the same sensing principle to achieve both the actual sensor and the reference in a smaller form factor. One technique to overcome this is to use the same sensor as a built-in reference by monitoring another parameter simultaneously that does not vary as the food spoils.

8.2.5.2 Interrogation Parameter

For wireless non-contact electrical sensing, there are three fundamental parameters of interest, resistance, capacitance and inductance. Resistance interrogation is simple and is shown in Chapter 7. Capacitance interrogation is based on measuring target loading with the fringing fields [124] or the impedance of the sensor element. Most of the sensors developed in this dissertation are based on capacitance change and are measured through an expensive Vector Network Analyzer. To make these sensors to be adapted in a practical case of food quality monitoring, detection of capacitance change is vital. The first step to perform that is to design a circuit that can convert capacitance to voltage or capacitance to frequency. The converted voltage or frequency is digitized and transmitted similar to the Ammonia sensor presented in Chapter 7. An example of converting capacitance to frequency is to use the sensor as part of the oscillator and generate frequency based on change in capacitance.

8.2.5.3 Sensitivity Improvement

In this dissertation, most of the sensors demonstrated consists of interdigitated sensors as sensing element. The fundamental concept of capacitive sensing using interdigitated sensing element is to utilize the strong fringing fields to improve coupling with targets. There are two different ways to improve the sensitivity of the sensing element: (i) design changes; improving the spacing and the width of the interdigitated capacitance; (ii) coverage changes; increasing the area of the sensing element at the same time maintaining smaller form factor. For a specific case such as volatile sensing; a common challenge is to improve the change in capacitance of the sensor as the food properties changes. Typically, the capacitance change is in ff making it very difficult to interrogate using a low cost reader and requires an expensive VNA. A potential solution to detect such as small change in the capacitance is to use Field Effect Transistor (FET) based device in which the gate of the device is modified as the sensing element. When the capacitance changes, electrostatic potentials across the gate changes that can further be used as a marker for sensing.

8.2.5.4 Selectivity Improvement

An important aspect to realize a reliable sensor that can be made part of a food supply chain quality control is the selectivity for the targeted parameter. The ability of the sensor to distinguish a particular parameter from other parameters of interest or from environmental interference is necessary to reduce the false positives or false negatives. This can be achieved by specifically tailoring the sensor to match the requirement such as substrate modification or thin film coating. For example, in case of volatile profiling, different affinity coatings with higher selectivity can be used to differentiate one volatile from the other. Table 8.1 lists different food volatiles as quality indicators as the food spoils over time due to contamination

or aging.

Table 8.1: Food Volatiles and Spoilage

Volatile	Spoilt Food	Quantity	Time	
Ethanol	Meat			
		75 (Auxiliary Unit(AU))	0 days	[125]
	Pork (AP)	26.9	8 days	
		16.9	13 days	
	Fish	0.15 mg/100g (ethanol/100 g of fish)	1 day	[126]
		2.1 mg/100g	14 day	
	Strawberry	0.5 $cm^{-}1$ (Peak Area (PA))	0 days	[127]
		4.5 $cm^{-}1$	14 days	
	Lettuce	0.31 (AU)	0 days	[128]
		22.5	9 days	
	Lettuce (MA)	0.51 (AU)	0 days	[128]
		10.47	5 days	
	Carrot	1.5 (ppm)	6 weeks	[129]
		35	16 weeks	
		42	20 weeks	
		1200	28 weeks	
	Ham	2.013 (AU)	0 days (7^o)	[130]
		228.344 (AU)	35 days (7^oC)	
	Kiwi	26.1 (μg/100 g.f.w)	0 days (8^o)	[131]
		10.3	9 weeks (8^oC)	
	Mango	195 (RPA)	61 days	[132]
		68	75 days	

8.2.6 Security and Authentication

For a real-time system, a potential challenge is to handle the enormous amount of data collected over time to characterize the quality of product. One solution is to increase the

on-board memory of the RFID IC, but this can be potentially altered or physically damaged making the quality control system less secure. The ability of the system to communicate with the cloud and transfer the data to a remote server makes it practical and easier to securely verify the product quality. One such technique is to use blockchain inspired RFID for product authentication and data logging as presented in [120]. In order to manage large data, instead of monitoring continuously, a technique to trigger the sensor when the quality deteriorates below a certain threshold can be considered.

Another aspect that needs to be considered is the reduction of false positives or false negatives for sensing results. A technique to solve this is to monitor multiple parameters simultaneously similar to hybrid sensor presented in Chapter 2. When multiple parameters are monitored, it provides a unique signature which is extremely hard to defeat and can provides a better authentication of results. Typically, single factor sensing can be easily defeated such as manipulating the properties of food to obtain similar results. For example, in case of adulteration, consider monitoring just the dielectric constant for measuring the adulteration gradient, it is easy to create a similar adulterated item with same dielectric constant as the original food item. This can give rise to false negatives and allows the product to pass through the different layers of supply chain. In this regards, if another property along with dielectric constant is monitored, say viscosity, it provides a unique signature making it hard to be defeated reducing the number of false negatives as well as false positives.

8.2.7 Multiple Sensor Scheduling and Readout

A sensor tag with comprehensive functionality will require sensing multiple target parameters simultaneously. A key bottleneck will be to develop a good scheduling algorithm for reading

these multiple sensors over a period of time. Certain sensors require real-time monitoring but at a specified interval and this determines the amount of data being generated and transmitted from the sensor tag to the cloud. One future direction is to develop a smart scheduling algorithm for reading multiple sensors using a micro controller. One objective of the scheduling algorithm can be to reduce power consumption as low as possible from the energy harvester [133]. This ensures improving the life time of the sensor with lower interrogation power at the reader circuitry.

8.2.8 Summary

Overall, as shown in Figure 8.1, a number of aspects should be investigated and advanced to practically adapt this modified sensing technique without modifying the tracking and tracing infrastructure as well as packaging infrastructure. The sensors developed in this dissertation are a first step towards making this technique a practical and viable solution of real time quality control of food products as it moves along the supply chain. To re-iterate, the ultimate goal of this technology is to ensure that the food reaching the fork meets the highest safety and quality standards.

APPENDICES

APPENDIX A

Photolithography Process

Procedure: 1. **Substrate Preparation and Cleaning.**

(a) Cut the substrate to desired dimensions.

(b) Rinse the susbtrate in acetone for 30 seconds.

(c) Rinse the substrate in methanol for 30 seconds.

(d) Rinse the substrate in DI water for 30 seconds.

(e) Rinse the substrate in isopropanol for 30 seconds.

(f) Blow dry using Nitrogen.

(g) Bake the substrate at 105^0C for 5 minutes.

2. **Spin-Coat Photoresist.**

(a) Set the rpm and time on Laurell Technologies Spinner (WS400B-6NPP LITE). Typically, for 17 μm thick Copper laminates, rpm is 3000 for 30 seconds.

(b) Spin the substrate after dropping positive photoresist S1813 over the substrate.

(c) Bake the substrate at 105^0 for 45 seconds.

3. **Expose and Develop**

(a) Calculate the expose time based on the power of the UV lamp in MJB 3 Mask Aligner and the spin coated thickness of the photoresist.

(b) Typically, expose for 45 seconds (3000 rpm, 30 sec - spin).

(c) Bake the substrate at 105^0 for 45 seconds.

(d) Develop using MF-319 for 30 seconds.

(e) Rinse with DI water and blow dry using Nitrogen.

(f) Bake at 105^0C for 5 minutes.

4. **Copper Etching**

(a) Prepare the etchant. Sodium per suplhate: DI water in 1:4 ratio (250 g in 1000 ml).

(b) Heat the etchant at 80^0C.

(c) Immerse the exposed substrate until the pattern is complete.

(d) Rinse with acetone, methanol for 30 seconds each.

(e) Rinse with DI water and bake at 105^0 for 5 minutes.

5. **Titanium Etching**

(a) Prepare the etchant. HF:NH4OH:DI water in 1:1:50 ratio.

(b) Immerse the substrate untill the pattern is complete.

(c) Immerse in DI water before rinsing.

6. **Zinc Oxide Ethcing**

(a) Prepare the etchant. HCl:DI water in 1:60 ratio.

(b) Immerse the substrate untill the ZnO is etched.

(c) Immerse in DI water before rinsing.

APPENDIX B

Thin Film Coating

SU8 Coating Procedure:

(a) Typically, SU8 and thinner are mixed in 1:1 ratio by volume. Depending on the thickness required, this ratio can be altered.

(b) Dispense the resist on the substrate and spin at 500 rpm for 30 seconds followed by 2000 rpm for 30 seconds.

(c) Bake at 95^0C for 5 minutes.

(d) Exposure time depends on the thickness of the resist coating and the power of the lamp. For the above mentioned spin speed, expose for 30 minutes.

(e) Post Exposure Bake in two steps, 60^0C for 5 minutes followed by 95^0C for 30 minutes.

(f) Immerse in SU8 developer for 10 minutes with constant stirring. Development time depends on the thickness of the resist.

(g) Bake at 95^0C for 10 minutes.

Polyaniline Coating Procedure:

(a) Mix PANi in emeraldine salt form with 1-Methyl-2-Pyrrolidone (1MP) in 1:100 ratio by weight.

(b) Sonicate for 30 minutes for proper mixing.

(c) Spin coat at 100 rpm for 1 minute.

(d) Bake at 120^{o}C for 30 min.

(e) Repeat spin coat followed by bake to obtain a near uniform coating of PANi over the sensor surface. Typically, 4 to 5 cycles are recommended.

APPENDIX C

Sputtering Process

Procedure:

1. **Pump the air out of the chamber.**

(a) Open the Nitrogen gas, turn on ThermoFlex 1400, Vacuum and Rate/Thickness Monitor.

(b) Open up the chamber, push the Shutter 1 button on the screen to open the shutter of the Titanium gun.

(c) After the check is complete, place the sample that needs to be sputtered at the center of the chuck. Close the chamber and put the lock on.

(d) Go the screen view, select Auto pump/vent, push the Auto pump button to pump the air out the chamber.

(e) After about 1 hour or when the displayed pressure on the screen becomes stable.

2. **Sputter the Titanium on the sample (600 A thick).**

(a) Calculate the thickness of the Ti layer. For example, normally 600 A (Anystrom) thick of Ti needs to be sputtered, which is equal to 60 nm thick. However, the thickness displayed on the monitor is half of the actual thickness, which means 300 A thick should be showed on the monitor in this case.

(b) Open the Airgas and the valve. Turn on the power supply that sits in between the vacuum and the monitor. Go to the Rate/Thickness monitor, press Program, choose Film 1 which correspond to Ti sputtering configuration. Then push Next several times to the end of the setup, and press Program again.

(c) In screen view, select DC sputter control—DC1—DC Ignition. Make sure the 125 w power correctly displayed on the power supply. Do not press shutter 1, because we need to burn off the Ti target till it looks light blue. Zero the time on the monitor

(d) When the Ti becomes light blue. Return to the screen, select shutter 1 to open the shutter of the Ti gun. Zero the time again.

3. **Sputter the Copper on the sample (1000 A thick).**

(a) Press shutter 1 to close the Ti gun. And select DC2—DC Ignition to heat up the copper target. Again, do not press shutter 2 now. Program Film 2 as in the previous step.

(b) Allow the copper target to be heated up for 30 seconds, then press shutter 2 to start sputter the copper on the sample. Zero the time.

(c) The actual thickness of the copper is the same as the thickness showed on the monitor. If 10 k A thick of copper needs to be sputtered, when the monitor shows 10k A thick, the sputtering process should be stopped by pressing the shutter 2 to close the copper gun.

4. **Auto vent the chamber.**

(a) Go to the Screen, select Auto pump/vent—Auto vent. When it is done, the lock of the chamber will fall. Then take out the sample by wearing the gloves.

(b) Change the transparent glass cover, turn off all the power supply and shut off the air gas and the Nitrogen.

APPENDIX D

Electroplating Process

Procedure:

(1) Set up the copper plating tank (2 gal)

(2) Add 3 lbs of copper crystals followed by 1.5 liters of copper sulphate and 140 ml Sulfuric Acid.

(3) The rest of the tank is filled with distilled water.

(4) Attach a copper plate and connect it to a power supply with a constant voltage of 5 V. The current varies from 0.25 A - 0.75 A depending on the size of the part to be plated.

(5) Hang the part to be plated inside the bath with the support of copper clips or wires for approximately 15-30 minutes depending on the thickness of the plated copper.

APPENDIX E

Sensitivity Calculations

Procedure: Current sensor sensitivity - 0.15 cc or 0.15 cm^3 of ethanol.

Density of ethanol = 789 kg/m^3 = 789 mg/cm^3.

Volume (5 drops) = 0.15 cm^3.

Mass (ethanol) = density * volume = 118.35 mg.

Volume of the container (jar) = 5 l = 5000 cc.

1 mg/L = 1 ppm.

Sensitivity of ethanol = 23.67 ppm.

An example for detection: Carrot freshness indicator [129] - ethanol

6 weeks - 1.5 ppm

16 weeks - 35 ppm

20 weeks - 42 ppm

28 weeks - 1200 ppm

BIBLIOGRAPHY

BIBLIOGRAPHY

[1] [Online]. Available: https://www.cdc.gov/foodsafety/foodborne-germs.html

[2] [Online]. Available: https://www.fda.gov/Safety/Recalls/default.htm

[3] [Online]. Available: https://www.fda.gov/Safety/Recalls/ucm596050.htm

[4] R. Johnson, "Food fraud and economically motivated adulteration of food and food ingredients," 2014.

[5] [Online]. Available: https://www.fda.gov/Food/GuidanceRegulation/FSMA/ucm378628.htm

[6] J. C. Moore, J. Spink, and M. Lipp, "Development and application of a database of food ingredient fraud and economically motivated adulteration from 1980 to 2010," *Journal of Food Science*, vol. 77, no. 4, 2012.

[7] [Online]. Available: https://www.usda.gov/oce/foodwaste/faqs.htm

[8] K. Finkenzeller, *RFID handbook: fundamentals and applications in contactless smart cards, radio frequency identification and near-field communication*. John Wiley & Sons, 2010.

[9] J. Landt, "The history of RFID," *IEEE potentials*, vol. 24, no. 4, pp. 8–11, 2005.

[10] R. Want, "An introduction to RFID technology," *IEEE pervasive computing*, vol. 5, no. 1, pp. 25–33, 2006.

[11] H. Tao, M. A. Brenckle, M. Yang, J. Zhang, M. Liu, S. M. Siebert, R. D. Averitt, M. S. Mannoor, M. C. McAlpine, J. A. Rogers *et al.*, "Silk-based conformal, adhesive, edible food sensors," *Advanced Materials*, vol. 24, no. 8, pp. 1067–1072, 2012.

[12] S. D. Nguyen, T. T. Pham, E. F. Blanc, N. N. Le, C. M. Dang, and S. Tedjini, "Approach for quality detection of food by RFID-based wireless sensor tag," *Electronics Letters*, vol. 49, no. 25, pp. 1588–1589, 2013.

[13] R. A. Potyrailo, N. Nagraj, Z. Tang, F. J. Mondello, C. Surman, and W. Morris, "Battery-free radio frequency identification (RFID) sensors for food quality and

safety," *Journal of agricultural and food chemistry*, vol. 60, no. 35, pp. 8535–8543, 2012.

[14] R. A. Potyrailo, W. G. Morris, T. Sivavec, H. W. Tomlinson, S. Klensmeden, and K. Lindh, "RFID sensors based on ubiquitous passive 13.56-mhz RFID tags and complex impedance detection," *Wireless Communications and Mobile Computing*, vol. 9, no. 10, pp. 1318–1330, 2009.

[15] E. Smits, J. Schram, M. Nagelkerke, R. Kusters, G. v. Heck, V. Van Acht, M. Van Koetse, J. v. d. Brand, G. Van Den Gelinck, and H. Schoo, "Development of printed RFID sensor tags for smart food packaging," in *Proceedings of the 14th International Meeting on Chemical Sensors, Nuremberg, Germany*, 2012, pp. 20–23.

[16] S. Mondal, D. Kumar, S. Karuppuswami, and P. Chahal, "A harmonic RF phase-shifter based wireless pH sensor," in *2018 IEEE 68th Electronic Components and Technology Conference (ECTC)*. IEEE, 2018, pp. 796–801.

[17] S. Mondal, S. Karuppuswami, R. Steinhorst, and P. Chahal, "A wearable passive pH sensor for health monitoring," in *2019 IEEE 69th Electronic Components and Technology Conference (ECTC)*. IEEE, 2019, pp. 1240–1245.

[18] W.-D. Huang, S. Deb, Y.-S. Seo, S. Rao, M. Chiao, and J. Chiao, "A passive radio-frequency pH-sensing tag for wireless food-quality monitoring," *IEEE Sensors Journal*, vol. 12, no. 3, pp. 487–495, 2011.

[19] S. Bhadra, D. S. Tan, D. J. Thomson, M. S. Freund, and G. E. Bridges, "A wireless passive sensor for temperature compensated remote pH monitoring," *IEEE Sensors Journal*, vol. 13, no. 6, pp. 2428–2436, 2013.

[20] S. Karuppuswami, A. Kaur, H. Arangali, and P. P. Chahal, "A hybrid magnetoelastic wireless sensor for detection of food adulteration," *IEEE Sensors Journal*, vol. 17, no. 6, pp. 1706–1714, 2017.

[21] J. Lorenzo, D. Girbau, A. Lázaro, and R. Villarino, "Temperature sensor based on frequency-coded chipless RFID tags," *Microwave and Optical Technology Letters*, vol. 56, no. 10, pp. 2411–2415, 2014.

[22] C. Amador, J.-P. Emond, and M. C. do Nascimento Nunes, "Application of RFID technologies in the temperature mapping of the pineapple supply chain," *Sensing and Instrumentation for Food Quality and Safety*, vol. 3, no. 1, pp. 26–33, 2009.

[23] T. Unander and H.-E. Nilsson, "Characterization of printed moisture sensors in packaging surveillance applications," *IEEE Sensors Journal*, vol. 9, no. 8, pp. 922–928, 2009.

[24] G. T. Le, T. V. Tran, H.-S. Lee, and W.-Y. Chung, "Long-range batteryless RF sensor for monitoring the freshness of packaged vegetables," *Sensors and Actuators A: Physical*, vol. 237, pp. 20–28, 2016.

[25] M. L. Rodrıguez-Méndez, J. Souto, R. de Saja, J. Martınez, and J. A. de Saja, "Lutetium bisphthalocyanine thin films as sensors for volatile organic components (VOCs) of aromas," *Sensors and Actuators B: Chemical*, vol. 58, no. 1-3, pp. 544–551, 1999.

[26] P. Acuña-Avila, R. Calavia, E. Vigueras-Santiago, and E. Llobet, "Identification of tequila with an array of zno thin films: A simple and cost-effective method," *Sensors*, vol. 17, no. 12, p. 2943, 2017.

[27] H. Hawari, N. Samsudin, A. M. Shakaff, Y. Wahab, U. Hashim, A. Zakaria, S. Ghani, and M. Ahmad, "Highly selective molecular imprinted polymer (MIP) based sensor array using interdigitated electrode (IDE) platform for detection of mango ripeness," *Sensors and Actuators B: Chemical*, vol. 187, pp. 434–444, 2013.

[28] S. Mondal, S. Karuppuswami, and P. Chahal, "ID integrated batteryless wireless digital pH sensor," *IEEE Sensors Journal*, vol. pp, no. p, pp. 1–1, 2019.

[29] J. Spink and D. C. Moyer, "Defining the public health threat of food fraud," *Journal of Food Science*, vol. 76, no. 9, pp. R157–R163, 2011.

[30] P. Shears, "Food fraud–a current issue but an old problem," *British Food Journal*, vol. 112, no. 2, pp. 198–213, 2010.

[31] K. Sharma and M. Paradakar, "The melamine adulteration scandal," *Food security*, vol. 2, no. 1, pp. 97–107, 2010.

[32] L. Doner and P. Cavender, "Chiral liquid chromatography for resolving malic acid enantiomers in adulterated apple juice," *Journal of Food Science*, vol. 53, no. 6, pp. 1898–1899, 1988.

[33] S. P. Natarajan, T. M. Weller, and D. P. Fries, "Sensitivity tunable inductive fluid conductivity sensor based on rf phase detection," *IEEE Sensors Journal*, vol. 7, no. 9, pp. 1300–1301, 2007.

[34] C. A. Grimes, C. S. Mungle, K. Zeng, M. K. Jain, W. R. Dreschel, M. Paulose, and K. G. Ong, "Wireless magnetoelastic resonance sensors: A critical review," *Sensors*, vol. 2, no. 7, pp. 294–313, 2002.

[35] S. Karuppuswami, A. Kaur, M. I. M. Ghazali, and P. Chahal, "RFID compatible sensor tags for remote liquid sample interrogation," in *Electronic Components and Technology Conference (ECTC), 2016 IEEE 66th.* IEEE, 2016, pp. 2401–2407.

[36] M. Pardo, L. Kwong, G. Sberveglieri, K. Brubaker, J. Schneider, W. Penrose, and J. Stetter, "Data analysis for a hybrid sensor array," *Sensors and Actuators B: Chemical*, vol. 106, no. 1, pp. 136–143, 2005.

[37] D. Kumar, S. Karuppuswami, Y. Deng, and P. Chahal, "A wireless shortwave near-field probe for monitoring structural integrity of dielectric composites and polymers," *NDT & E International*, vol. 96, pp. 9–17, 2018.

[38] K. G. Ong, M. K. Jain, C. Mungle, S. Schmidt, and C. A. Grimes, "Magnetism-based sensors," in *Complex Mediums II: Beyond Linear Isotropic Dielectrics*, vol. 4467. International Society for Optics and Photonics, 2001, pp. 158–172.

[39] A. Hernando, M. Vazquez, and J. Barandiaran, "Metallic glasses and sensing applications," *Journal of Physics E: Scientific Instruments*, vol. 21, no. 12, p. 1129, 1988.

[40] L. Meirovitch, *Analytical methods in vibrations.* Pearson, 1967.

[41] T. Grove, M. Masters, and R. Miers, "Determining dielectric constants using a parallel plate capacitor," *American journal of physics*, vol. 73, no. 1, pp. 52–56, 2005.

[42] J. B. Segur and H. E. Oberstar, "Viscosity of glycerol and its aqueous solutions," *Industrial & Engineering Chemistry*, vol. 43, no. 9, pp. 2117–2120, 1951.

[43] G. Akerlof, "Dielectric constants of some organic solvent-water mixtures at various temperatures," *Journal of the American Chemical Society*, vol. 54, no. 11, pp. 4125–4139, 1932.

[44] C. A. Grimes, D. Kouzoudis, and C. Mungle, "Simultaneous measurement of liquid density and viscosity using remote query magnetoelastic sensors," *Review of scientific instruments*, vol. 71, no. 10, pp. 3822–3824, 2000.

[45] S. Karuppuswami, H. Arangali, and P. Chahal, "A hybrid electrical-mechanical wireless magnetoelastic sensor for liquid sample measurements," in *Electronic Components and Technology Conference (ECTC), 2016 IEEE 66th.* IEEE, 2016, pp. 2535–2540.

[46] J. N. Coupland and D. J. McClements, "Physical properties of liquid edible oils," *Journal of the American Oil Chemists' Society*, vol. 74, no. 12, pp. 1559–1564, 1997.

[47] H. Noureddini, B. Teoh, and L. Davis Clements, "Viscosities of vegetable oils and fatty acids," *Journal of the American Oil Chemists' Society*, vol. 69, no. 12, pp. 1189–1191, 1992.

[48] J. A. Byford, M. I. M. Ghazali, S. Karuppuswami, B. L. Wright, and P. Chahal, "Demonstration of RF and microwave passive circuits through 3-D printing and selective metalization," *IEEE Transactions on Components, Packaging and Manufacturing Technology*, vol. 7, no. 3, pp. 463–471, 2017.

[49] M. I. M. Ghazali, S. Karuppuswami, A. Kaur, and P. Chahal, "3D printed high functional density packaging compatible out-of-plane antennas," *Additive Manufacturing*, vol. 30, p. 100863, 2019.

[50] M. I. M. Ghazali, S. Karuppuswami, and P. Chahal, "3-D printed embedded passive harmonic sensor tag as markers for buried assets localization," *IEEE Sensors Letters*, vol. 3, no. 4, pp. 1–4, 2019.

[51] S.-H. Chao, "Measurements of microwave conductivity and dielectric constant by the cavity perturbation method and their errors," *IEEE transactions on microwave theory and techniques*, vol. 33, no. 6, pp. 519–526, 1985.

[52] K. Mathew and U. Raveendranath, "Cavity perturbation techniques for measuring dielectric parameters of water and other allied liquids," *Sensors Update*, vol. 7, no. 1, pp. 185–210, 2000.

[53] L.-F. Chen, C. Ong, C. Neo, V. Varadan, and V. K. Varadan, *Microwave electronics: measurement and materials characterization*. John Wiley & Sons, 2004.

[54] A. K. Jha and M. J. Akhtar, "SIW cavity based RF sensor for dielectric characterization of liquids," in *2014 IEEE Conference on Antenna Measurements & Applications (CAMA)*. IEEE, 2014, pp. 1–4.

[55] P. Sharma, L. Lao, and G. Falcone, "A microwave cavity resonator sensor for water-in-oil measurements," *Sensors and Actuators B: Chemical*, vol. 262, pp. 200–210, 2018.

[56] H. Guo, L. Yao, and F. Huang, "A cylindrical cavity sensor for liquid water content measurement," *Sensors and Actuators A: Physical*, vol. 238, pp. 133–139, 2016.

[57] T. H. Basey-Fisher, N. Guerra, C. Triulzi, A. Gregory, S. M. Hanham, M. M. Stevens, S. A. Maier, and N. Klein, "Microwaving blood as a non-destructive technique for haemoglobin measurements on microlitre samples," *Advanced healthcare materials*, vol. 3, no. 4, pp. 536–542, 2014.

[58] T. Hayat, T. Ejaz, M. Naveed, T. Zaidi, and H.-U. Rahman, "Permittivity sensing and measurement with novel split ball resonator using E-field perturbation technique," *Microwave and Optical Technology Letters*, vol. 60, no. 3, pp. 748–754, 2018.

[59] E. Massoni, G. Siciliano, M. Bozzi, and L. Perregrini, "Enhanced cavity sensor in SIW technology for material characterization," *IEEE Microwave and Wireless Components Letters*, vol. 28, no. 10, pp. 948–950, 2018.

[60] R. C. Caleffo and F. S. Correra, "Liquids electrical characterization sensor using a hybrid SIW resonant cavity," *Microwave and Optical Technology Letters*, vol. 60, no. 2, pp. 445–449, 2018.

[61] A. Yasin, F. U. Rehman, U. Naeem, S. A. Khan, and M. F. Shafique, "Top loaded tm01δ mode cylindrical dielectric resonator for complex permittivity characterization of liquids," *Radioengineering*, vol. 25, no. 4, pp. 714–720, 2016.

[62] M. I. M. Ghazali, S. Karuppuswami, S. Mondal, A. Kaur, and P. Chahal, "Embedded actives using additive manufacturing for high density RF circuits and systems," *IEEE Transactions on Components, Packaging and Manufacturing Technology*, 2019.

[63] M. I. M. Ghazali, S. Mondal, S. Karuppuswami, and P. Chahal, "3D printed substrates for the design of compact RF systems," in *2019 IEEE 69th Electronic Components and Technology Conference (ECTC)*. IEEE, 2019, pp. 113–118.

[64] M. I. M. Ghazali, S. Karuppuswami, A. Kaur, and P. Chahal, "3-D printed air substrates for the design and fabrication of rf components," *IEEE Transactions on Components, Packaging and Manufacturing Technology*, vol. 7, no. 6, pp. 982–989, 2017.

[65] M. I. M. Ghazali, J. A. Byford, S. Karuppuswami, A. Kaur, J. Lennon, and P. Chahal, "3D printed out-of-plane antennas for use on high density boards," in *2017 IEEE 67th Electronic Components and Technology Conference (ECTC)*. IEEE, 2017, pp. 1835–1842.

[66] S. Karuppuswami, S. Mondal, M. I. M. Ghazali, and P. Chahal, "A reusable 3D printed cavity resonator for liquid sample characterization," in *International Symposium on Microelectronics*, vol. 2018, no. 1. International Microelectronics Assembly and Packaging Society, 2018, pp. 000 389–000 392.

[67] D. M. Pozar, *Microwave engineering*. John Wiley & Sons, 2009.

[68] S. Karuppuswami, S. Mondal, M. I. M. Ghazali, and P. Chahal, "A multiuse fully 3-D printed cavity sensor for liquid profiling," *IEEE Sensors Letters*, vol. 3, no. 2, pp. 1–4, 2018.

[69] W. Liu, H. Sun, and L. Xu, "A microwave method for dielectric characterization measurement of small liquids using a metamaterial-based sensor," *Sensors*, vol. 18, no. 5, p. 1438, 2018.

[70] A. Bage and S. Das, "Studies of some non conventional split ring and complementary split ring resonators for waveguide band stop & band pass filter application," in *2013 International Conference on Microwave and Photonics (ICMAP)*. IEEE, 2013, pp. 1–5.

[71] A. Salim and S. Lim, "Review of recent metamaterial microfluidic sensors," *Sensors*, vol. 18, no. 1, p. 232, 2018.

[72] J. Wu, P. Wang, X. Huang, F. Rao, X. Chen, Z. Shen, and H. Yang, "Design and validation of liquid permittivity sensor based on RCRR microstrip metamaterial," *Sensors and Actuators A: Physical*, vol. 280, pp. 222–227, 2018.

[73] E. L. Chuma, Y. Iano, G. Fontgalland, and L. L. B. Roger, "Microwave sensor for liquid dielectric characterization based on metamaterial complementary split ring resonator," *IEEE Sensors Journal*, vol. 18, no. 24, pp. 9978–9983, 2018.

[74] A. Salim and S. Lim, "Complementary split-ring resonator-loaded microfluidic ethanol chemical sensor," *Sensors*, vol. 16, no. 11, p. 1802, 2016.

[75] C.-M. Hsu and C.-L. Yang, "High sensitive detection of flow rate and permittivity through microfluidics based on complementary split-ring resonators," in *2017 IEEE MTT-S International Microwave Symposium (IMS)*. IEEE, 2017, pp. 1015–1017.

[76] S. Karuppuswami, M. I. M. Ghazali, S. Mondal, D. Kumar, A. Kaur, and P. Chahal, "A 3D printed UHF passive RFID tag for plastic components," in *2019 IEEE International Symposium on Antennas and Propagation and USNC-URSI Radio Science Meeting*. IEEE, 2019, pp. 597–598.

[77] M. I. M. Ghazali, S. Karuppuswami, S. Mondal, and P. Chahal, "Embedded active elements in 3D printed structures for the design of RF circuits," in *2018 IEEE 68th Electronic Components and Technology Conference (ECTC)*. IEEE, 2018, pp. 1062–1067.

[78] S. Karuppuswami, L. L. Matta, E. C. Alocilja, and P. Chahal, "A wireless RFID compatible sensor tag using gold nanoparticle markers for pathogen detection in the liquid food supply chain," *IEEE sensors letters*, vol. 2, no. 2, pp. 1–4, 2018.

[79] L. L. Matta, S. Karuppuswami, P. Chahal, and E. C. Alocilja, "AuNP-RF sensor: An innovative application of RF technology for sensing pathogens electrically in liquids (SPEL) within the food supply chain," *Biosensors and Bioelectronics*, vol. 111, pp. 152–158, 2018.

[80] J. Glover, D. Champion, K. Daniels, and A. Dainty, "An institutional theory perspective on sustainable practices across the dairy supply chain," *International Journal of Production Economics*, vol. 152, pp. 102–111, 2014.

[81] N. Wang, N. Zhang, and M. Wang, "Wireless sensors in agriculture and food industryrecent development and future perspective," *Computers and electronics in agriculture*, vol. 50, no. 1, pp. 1–14, 2006.

[82] H. M. Østlie, M. H. Helland, and J. A. Narvhus, "Growth and metabolism of selected strains of probiotic bacteria in milk," *International Journal of Food Microbiology*, vol. 87, no. 1-2, pp. 17–27, 2003.

[83] J. D. Cunningham and L. S. Connie, "Collaborative study of the bactoscan–an automated method for determinations of total bacteria in raw milk," *Canadian Institute of Food Science and Technology Journal*, vol. 21, no. 5, pp. 464–466, 1988.

[84] T. Chen, S. Li, and H. Sun, "Metamaterials application in sensing," *Sensors*, vol. 12, no. 3, pp. 2742–2765, 2012.

[85] H.-J. Lee, J.-H. Lee, H.-S. Moon, I.-S. Jang, J.-S. Choi, J.-G. Yook, and H.-I. Jung, "A planar split-ring resonator-based microwave biosensor for label-free detection of biomolecules," *Sensors and Actuators B: Chemical*, vol. 169, pp. 26–31, 2012.

[86] H.-J. Lee and J.-G. Yook, "Biosensing using split-ring resonators at microwave regime," *Applied Physics Letters*, vol. 92, no. 25, p. 254103, 2008.

[87] A. W. Clark, A. Glidle, D. R. Cumming, and J. M. Cooper, "Plasmonic split-ring resonators as dichroic nanophotonic DNA biosensors," *Journal of the American Chemical Society*, vol. 131, no. 48, pp. 17 615–17 619, 2009.

[88] J. K. Perng, W. D. Hunt, and P. J. Edmonson, "Development of a shear horizontal SAW RFID biosensor," in *SENSORS, 2007 IEEE*. IEEE, 2007, pp. 691–694.

[89] H. Xu, A. E. Murdaugh, W. Chen, K. E. Aidala, M. A. Ferguson, E. M. Spain, and M. E. Nunez, "Characterizing pilus-mediated adhesion of biofilm-forming e. coli to chemically diverse surfaces using atomic force microscopy," *Langmuir*, vol. 29, no. 9, pp. 3000–3011, 2013.

[90] T. M. Joys, "The covalent structure of the phase-1 flagellar filament protein of salmonella typhimurium and its comparison with other flagellins." *Journal of biological chemistry*, vol. 260, no. 29, pp. 15 758–15 761, 1985.

[91] J. Chen, M. L. Rossman, and D. M. Pawar, "Attachment of enterohemorrhagic escherichia coli to the surface of beef and a culture medium," *LWT-Food Science and Technology*, vol. 40, no. 2, pp. 249–254, 2007.

[92] J. Schnürer, J. Olsson, and T. Börjesson, "Fungal volatiles as indicators of food and feeds spoilage," *Fungal Genetics and Biology*, vol. 27, no. 2-3, pp. 209–217, 1999.

[93] A. Pacquit, K. T. Lau, H. McLaughlin, J. Frisby, B. Quilty, and D. Diamond, "Development of a volatile amine sensor for the monitoring of fish spoilage," *Talanta*, vol. 69, no. 2, pp. 515–520, 2006.

[94] A. Loutfi, S. Coradeschi, G. K. Mani, P. Shankar, and J. B. B. Rayappan, "Electronic noses for food quality: A review," *Journal of Food Engineering*, vol. 144, pp. 103–111, 2015.

[95] S. Karuppuswami, J. A. Byford, and P. Chahal, "A volatile molecular sensor using terahertz resonators on porous substrates," in *2018 IEEE 68th Electronic Components and Technology Conference (ECTC)*. IEEE, 2018, pp. 2295–2300.

[96] K. G. Ong, C. Grimes, C. Robbins, and R. Singh, "Design and application of a wireless, passive, resonant-circuit environmental monitoring sensor," *Sensors and Actuators A: Physical*, vol. 93, no. 1, pp. 33–43, 2001.

[97] W. J. Moore, *Basic physical chemistry*. Prentice Hall, 1983.

[98] A. C. Mitropoulos, "The kelvin equation," *Journal of Colloid and Interface Science*, vol. 317, no. 2, pp. 643–648, 2008.

[99] L. Fisher and J. Israelachvili, "Direct experimental verification of the kelvin equation for capillary condensation," *Nature*, vol. 277, no. 5697, p. 548, 1979.

[100] A. Malijevskỳ and A. O. Parry, "Modified kelvin equations for capillary condensation in narrow and wide grooves," *Physical Review Letters*, vol. 120, no. 13, p. 135701, 2018.

[101] F. Vodák, "Dielectric constant of an n-element moist capillary-porous material," *Czechoslovak Journal of Physics B*, vol. 23, no. 10, pp. 1093–1101, 1973.

[102] D. Wallacher, V. Soprunyuk, A. Kityk, and K. Knorr, "Dielectric response of CO and ar condensed into mesoporous glass," *Physical Review B*, vol. 66, no. 1, p. 014203, 2002.

[103] M. T. Hallikainen, F. T. Ulaby, M. C. Dobson, M. A. El-Rayes, and L.-K. Wu, "Microwave dielectric behavior of wet soil-part 1: Empirical models and experimental observations," *IEEE Transactions on Geoscience and Remote Sensing*, no. 1, pp. 25–34, 1985.

[104] M. C. Dobson, F. T. Ulaby, M. T. Hallikainen, and M. A. El-Rayes, "Microwave dielectric behavior of wet soil-part ii: Dielectric mixing models," *IEEE Transactions on Geoscience and Remote Sensing*, no. 1, pp. 35–46, 1985.

[105] C. Y. Chan and R. J. Knight, "Determining water content and saturation from dielectric measurements in layered materials," *Water Resources Research*, vol. 35, no. 1, pp. 85–93, 1999.

[106] A. Goncharenko, V. Lozovski, and E. Venger, "Lichtenecker's equation: applicability and limitations," *Optics Communications*, vol. 174, no. 1-4, pp. 19–32, 2000.

[107] A. Brovelli and G. Cassiani, "Effective permittivity of porous media: A critical analysis of the complex refractive index model," *Geophysical Prospecting*, vol. 56, no. 5, pp. 715–727, 2008.

[108] S. Karuppuswami, N. Wiwatcharagoses, A. Kaur, and P. Chahal, "Capillary condensation based wireless volatile molecular sensor," in *Electronic Components and Technology Conference (ECTC), 2017 IEEE 67th.* IEEE, 2017, pp. 1455–1460.

[109] S. Matindoust, A. Farzi, M. B. Nejad, M. H. S. Abadi, Z. Zou, and L.-R. Zheng, "Ammonia gas sensor based on flexible polyaniline films for rapid detection of spoilage in protein-rich foods," *Journal of Materials Science: Materials in Electronics*, vol. 28, no. 11, pp. 7760–7768, 2017.

[110] D. Kwak, Y. Lei, and R. Maric, "Ammonia gas sensors: A comprehensive review," *Talanta*, 2019.

[111] A. Tripathi, K. P. Misra, and R. Shukla, "Enhancement in ammonia sensitivity with fast response by doping al2o3 in polyaniline," *Journal of Applied Polymer Science*, vol. 130, no. 3, pp. 1941–1948, 2013.

[112] S. Shen, Z. Fan, J. Deng, X. Guo, L. Zhang, G. Liu, Q. Tan, and J. Xiong, "An LC passive wireless gas sensor based on PANI/CNT composite," *Sensors*, vol. 18, no. 9, p. 3022, 2018.

[113] M. Eising, C. E. Cava, R. V. Salvatierra, A. J. G. Zarbin, and L. S. Roman, "Doping effect on self-assembled films of polyaniline and carbon nanotube applied as ammonia gas sensor," *Sensors and Actuators B: Chemical*, vol. 245, pp. 25–33, 2017.

[114] N. Tang, C. Zhou, L. Xu, Y. Jiang, H. Qu, and X. Duan, "A fully integrated wireless flexible ammonia sensor fabricated by soft nano-lithography," *ACS sensors*, vol. 4, no. 3, pp. 726–732, 2019.

[115] A. V. Quintero, F. Molina-Lopez, E. Smits, E. Danesh, J. van den Brand, K. Persaud, A. Oprea, N. Barsan, U. Weimar, N. De Rooij *et al.*, "Smart RFID label with a printed multisensor platform for environmental monitoring," *Flexible and Printed Electronics*, vol. 1, no. 2, p. 025003, 2016.

[116] S. Karuppuswami, M. I. M. Ghazali, S. Mondal, and P. Chahal, "Wireless EAS sensor tags for volatile profiling in food packages," in *2018 IEEE 68th Electronic Components and Technology Conference (ECTC)*. IEEE, 2018, pp. 2174–2179.

[117] S. Mondal, M. I. M. Ghazali, S. Karuppuswami, A. Kaur, and P. Chahal, "A nonlinear transmission line based harmonic RF tag," in *2017 IEEE 67th Electronic Components and Technology Conference (ECTC)*. IEEE, 2017, pp. 2237–2242.

[118] D. Kumar, S. Mondal, S. Karuppuswami, Y. Deng, and P. Chahal, "Harmonic RFID communication using conventional UHF system," *IEEE Journal of Radio Frequency Identification*, 2019.

[119] M. I. M. Ghazali, S. Karuppuswami, and P. Chahal, "Embedded passive RF tags towards intrinsically locatable buried plastic materials," in *2016 IEEE 66th Electronic Components and Technology Conference (ECTC)*. IEEE, 2016, pp. 2575–2580.

[120] S. Mondal, K. Wijewardena, S. Karuppuswami, N. Kriti, D. Kumar, and P. Chahal, "Blockchain inspired RFID based information architecture for food supply chain," *IEEE Internet of Things Journal*, 2019.

[121] S. Karuppuswami, M. I. M. Ghazali, A. Kaur, and P. Chahal, "Multi-band harmonic RF tags for barcode applications in a cluttered environment," in *Electronic Components and Technology Conference (ECTC), 2017 IEEE 67th*. IEEE, 2017, pp. 1861–1867.

[122] F. Johansson and A. Leufven, "Food packaging polymer films as aroma vapor barriers at different relative humidities," *Journal of food science*, vol. 59, no. 6, pp. 1328–1331, 1994.

[123] [Online]. Available: https://www.fda.gov/food/packaging-food-contact-substances-fcs

[124] S. Karuppuswami, E. Rothwell, P. Chahal, and M. Havrilla, "A triaxial applicator for the measurement of the electromagnetic properties of materials," *Sensors*, vol. 18, no. 2, p. 383, 2018.

[125] E. Jääskeläinen, P. Johansson, O. Kostiainen, T. Nieminen, G. Schmidt, P. Somervuo, M. Mohsina, P. Vanninen, P. Auvinen, and J. Björkroth, "Significance of heme-based respiration in meat spoilage caused by leuconostoc gasicomitatum," *Applied and environmental microbiology*, pp. AEM–02 943, 2012.

[126] S. D. KELLEHER and R. R. ZALL, "Ethanol accumulations in muscle tissue as a chemical indicator of fish spoilage," *Journal of Food Biochemistry*, vol. 7, no. 2, pp. 87–92, 1983.

[127] D. Dong, C. Zhao, W. Zheng, W. Wang, X. Zhao, and L. Jiao, "Analyzing strawberry spoilage via its volatile compounds using longpath fourier transform infrared spectroscopy," *Scientific reports*, vol. 3, p. 2585, 2013.

[128] P. Ragaert, F. Devlieghere, E. Devuyst, J. Dewulf, H. Van Langenhove, and J. Debevere, "Volatile metabolite production of spoilage micro-organisms on a mixed-lettuce agar during storage at 7 C in air and low oxygen atmosphere," *International journal of food microbiology*, vol. 112, no. 2, pp. 162–170, 2006.

[129] D. Heatherbell, R. Wrolstad, and L. Libbey, "Carrot volatiles." *Journal of Food Science*, vol. 36, no. 2, pp. 219–224, 1971.

[130] F. Leroy, C. Vasilopoulos, S. Van Hemelryck, G. Falony, and L. De Vuyst, "Volatile analysis of spoiled, artisan-type, modified-atmosphere-packaged cooked ham stored under different temperatures," *Food Microbiology*, vol. 26, no. 1, pp. 94–102, 2009.

[131] H. Young and V. J. Paterson, "The effects of harvest maturity, ripeness and storage on kiwifruit aroma," *Journal of the Science of Food and Agriculture*, vol. 36, no. 5, pp. 352–358, 1985.

[132] M. Lebrun, A. Plotto, K. Goodner, M.-N. Ducamp, and E. Baldwin, "Discrimination of mango fruit maturity by volatiles using the electronic nose and gas chromatography," *Postharvest Biology and Technology*, vol. 48, no. 1, pp. 122–131, 2008.

[133] S. Mondal, S. Karuppuswami, M. I. M. Ghazali, A. Kaur, P. Chahal *et al.*, "A PSK modulation scheme for sensor integrated RFIDs," in *2019 IEEE International Symposium on Antennas and Propagation and USNC-URSI Radio Science Meeting*. IEEE, 2019, pp. 635–636.